


Spring 2015

# Quantifying moisture transport in cementitious materials using neutron radiography

Catherine L. Lucero  
*Purdue University*

Follow this and additional works at: [https://docs.lib.purdue.edu/open\\_access\\_theses](https://docs.lib.purdue.edu/open_access_theses)

 Part of the [Civil Engineering Commons](#), and the [Materials Science and Engineering Commons](#)

---

## Recommended Citation

Lucero, Catherine L., "Quantifying moisture transport in cementitious materials using neutron radiography" (2015). *Open Access Theses*. 572.  
[https://docs.lib.purdue.edu/open\\_access\\_theses/572](https://docs.lib.purdue.edu/open_access_theses/572)

This document has been made available through Purdue e-Pubs, a service of the Purdue University Libraries. Please contact [epubs@purdue.edu](mailto:epubs@purdue.edu) for additional information.

**PURDUE UNIVERSITY  
GRADUATE SCHOOL  
Thesis/Dissertation Acceptance**

This is to certify that the thesis/dissertation prepared

By Catherine L. Lucero

Entitled

Quantifying Fluid Transport in Cementitious Materials Using Neutron Radiography

For the degree of Master of Science in Civil Engineering

Is approved by the final examining committee:

W. Jason Weiss

Chair

Dale P. Bentz

Jan Olek

To the best of my knowledge and as understood by the student in the Thesis/Dissertation Agreement, Publication Delay, and Certification Disclaimer (Graduate School Form 32), this thesis/dissertation adheres to the provisions of Purdue University's "Policy of Integrity in Research" and the use of copyright material.

Approved by Major Professor(s): W. Jason Weiss

Approved by: Dr. Dulcy Abraham

Head of the Departmental Graduate Program

5/14/2015

Date



QUANTIFYING MOISTURE TRANSPORT IN CEMENTITIOUS MATERIALS  
USING NEUTRON RADIOGRAPHY

A Thesis

Submitted to the Faculty

of

Purdue University

by

Catherine L. Lucero

In Partial Fulfillment of the

Requirements for the Degree

of

Master of Science in Civil Engineering

May 2015

Purdue University

West Lafayette, Indiana

## ACKNOWLEDGEMENTS

First, I would like to acknowledge my advisor, Dr. Jason Weiss for his support and guidance. I have had so many incredible opportunities during my time at Purdue and it was an honor to work with you. I would also like to thank my members of my committee, Professor Jan Olek and Mr. Dale Bentz, for their support.

I would like to thank my colleagues, Robert Spragg, Yaghoob Farnam, Timothy Barrett, Heather Todak, Nathan Todd, Andrea LaGreca, Chiara Villani, Andrew Weise, and Chunyu Qiao for their advice, assistance and encouragement in my work.

I would like to acknowledge the support of the National Institute of Standards and Technology, U.S. Department of Commerce, in providing the neutron research facilities used in this work. The guidance from Dr. Daniel Hussey and Dr. David Jacobson is greatly appreciated.

I would like to thank my family for their unconditional love and support in all my academic endeavors.

## TABLE OF CONTENTS

	Page
LIST OF TABLES .....	vi
LIST OF FIGURES .....	vii
ABSTRACT .....	xi
CHAPTER 1. INTRODUCTION, OBJECTIVES, AND ORGANIZATION.....	1
1.1 Introduction .....	1
1.2 Research Objectives .....	2
1.3 Organization and Contents of Thesis .....	3
CHAPTER 2. BACKGROUND ON THE USE OF NEUTRON IMAGING IN POROUS MEDIA RESEARCH.....	6
2.1 Assessing Moisture Content in Cementitious Materials Using X-Ray Imaging.....	6
2.2 Assessing Moisture Content in Various Porous Media Using Neutron Radiography and Tomography .....	10
2.3 Summary .....	15
CHAPTER 3. MONITORING FLUID PENETRATION AND QUANTIFYING MOISTURE CONTENT IN MORTAR USING NEUTRON RADIOGRAPHY .....	17
3.1 Abstract .....	17
3.2 Introduction .....	18
3.3 Experimental Methods .....	20
3.3.1 Sample Preparation .....	20
3.3.2 Neutron Imaging .....	21
3.3.3 Image Processing and Analysis .....	22
3.3.4 Gravimetric Absorption .....	24
3.4 Results and Discussion .....	24
3.4.1 Depth of Water Penetration .....	24

	Page
3.4.2 Degree of Saturation .....	28
3.4.3 Intrinsic Absorption .....	33
3.5 Conclusions .....	37
 CHAPTER 4. USING NEUTRON RADIOGRAPHY TO QUANTIFY THE DEGREE OF SATURATION IN AIR ENTRAINED CEMENT BASED MORTAR .....	38
4.1 Abstract .....	38
4.2 Introduction .....	38
4.3 Experimental .....	39
4.3.1 Sample Preparation .....	39
4.3.2 Neutron Imaging .....	41
4.3.3 Image Processing and Analysis .....	43
4.4 Results .....	44
4.4.1 Expansion of Beer's Law .....	44
4.4.2 Degree of Saturation .....	46
4.4.2.1 Predicted Values of $S$ Based on Composite Attenuation Coefficient .....	46
4.4.2.2 Degree of Saturation in Mortars Absorbing Water from One Edge .....	48
4.5 Conclusions .....	51
 CHAPTER 5. USING NEUTRON RADIOGRAPHY TO MEASURE THE ABSORPTION OF CALCIUM CHLORIDE SOLUTION IN MORTAR .....	53
5.1 Abstract .....	53
5.2 Introduction .....	54
5.3 Experimental .....	57
5.3.1 Sample Preparation .....	57
5.3.2 Neutron Imaging .....	60
5.3.3 Image Processing and Analysis .....	62
5.4 Results and Discussion .....	65
5.4.1 Depth of Fluid Penetration .....	65
5.4.2 Change in Degree of Saturation .....	69
5.5 Conclusions .....	75
 CHAPTER 6. NEUTRON RADIOGRAPHY EVALUATION OF DRYING IN MORTARS WITH AND WITHOUT SHRINKAGE REDUCING ADMIXTURES .....	77
6.1 Introduction .....	77
6.2 Experimental .....	80
6.2.1 Sample Preparation .....	80
6.2.2 Dynamic Vapor Sorption (DVS) testing .....	81

	Page
6.2.3 Neutron Imaging.....	81
6.3 Results .....	83
6.3.1 Theoretical Observations on the Influence of Liquid Properties on Drying .....	83
6.3.2 Desorption Isotherms .....	85
6.3.3 Moisture Diffusion Coefficient.....	88
6.3.4 Moisture Profiles.....	90
6.4 Conclusions .....	95
 CHAPTER 7. CONCLUSIONS AND FUTURE WORK .....	 97
7.1 Summary of Current Work.....	97
7.2 Suggestions for Future Work .....	100
 REFERENCES .....	 101



## LIST OF TABLES

Table	Page
3.1. Mixture proportions .....	21
3.2. Calculated and measured values for $S_{\text{matrix}}$ for each mortar.....	31
3.3. Measured intrinsic sorptivity of mortars exposed to water as determined from neutron radiographs and gravimetrically .....	36
4.1. Mixture proportions for mortar samples used for neutron radiography .....	40
4.2. Calculated and measured values of $\mu_i$ for use in Equation 5.4.....	46
5.1. Mixture proportions for the four mortars used in absorption experiments .....	58
5.2. Chemical and physical properties of ordinary Portland cement .....	58
5.3. Fluid properties for concentrations of $\text{CaCl}_2$ solutions used in this study .....	60
5.4. Calculated components of porosity according to Powers model .....	64
5.5. Summary of measured sorptivity and normalized sorptivity for mortar samples exposed to $\text{CaCl}_2$ solutions. ....	68

## LIST OF FIGURES

Figure	Page
2.1 Principal components of an X-ray or neutron radiography system. ....	6
2.2 Optical density as a function of water (step) thickness used to calculate the attenuation coefficient of water. After Hussey et al. [22] .....	11
3.1. Neutron attenuation through material. An incident beam, $I_0$ , passes through matter causing some neutrons to be absorbed, some to scatter and some to pass through resulting in the transmitted beam, $I$ . ....	20
3.2. Experimental set up of absorption testing in the neutron beam chamber. (a) Aluminum holder with 10 mortar samples and (b) a sketch of the cross section of the arrangement showing the water source in the aluminum track. ....	22
3.3. Determination of average depth of penetration from (a) normalized neutron images. (b) Images were segmented and converted to binary and a (c) mask was subtracted to (d) result in measurable line segments at 10 locations. ....	23
3.4 Typical radiograph used for analysis. The image of a wetted mortar has been normalized to an image in the dry state. The dashed rectangle is the area of analysis for water thickness calculations. ....	25
3.5. (a) Average fluid depth of penetration and (b) ASTM C1585 absorption results as determined by Equation 3.3 for air entrained and non air entrained mortar with a w/c of 0.42 .....	26
3.6. (a) Average fluid depth of penetration and (b) ASTM C1585 absorption results as determined by Equation 3.3 for air entrained and non air entrained mortar with a w/c of 0.30 .....	27
3.7 Influence of w/c on depth of water penetration in mortar with a low degree of hydration. ....	28
3.8. Calibration curve for water. The measured attenuation coefficient for water is $0.3808 \text{ mm}^{-1}$ . ....	29

Figure	Page
3.9. Degree of saturation with respect to distance from fluid source evaluated for (a) non air entrained and (b) air entrained mortar with a high degree of hydration.....	31
3.10. Degree of saturation with respect to distance from fluid source evaluated for (a) non air entrained and (b) air entrained mortar with a high degree of hydration.....	32
3.11. Degree of saturation with respect to distance from fluid source evaluated for mortars with a w/c of 0.30 and a degree of hydration of (a) 0.34 and (b) 0.43.....	32
3.12. Desorption isotherm for mortar with a w/c of 0.42 and degree of hydration of 75% with and without air entraining admixture.....	33
3.13. Calculated intrinsic absorption compared to measured depth of penetration evaluated for (a) non air entrained and (b) air entrained mortar with a high degree of hydration.....	34
3.14. Calculated intrinsic absorption compared to measured depth of penetration evaluated for (a) non air entrained and (b) air entrained mortar with a low degree of hydration.....	35
3.15. Calculated intrinsic absorption compared to measured depth of penetration evaluated for non air entrained mortar with (a) a degree of hydration of 0.34 and (b) a degree of hydration of 0.43. ....	35
4.1. Experimental set up for neutron radiography at the Neutron Imaging Facility at NIST. ....	42
4.2. Volumetric proportions of constituents of hydrated cement paste with respect to the degree of hydration.....	45
4.3. The influence of the degree of saturation on $\mu_{mortar}$ for a (a) low degree of hydration (35 %) and a (b) high degree of hydration (72 %) .....	47
4.4. Influence of degree of hydration on $\mu_{mortar}$ with $S$ of 0, w/c of 0.42, and $V_a$ of 0.55.....	48
4.5. Area of analysis of a typical mortar sample exposed to water on the bottom surface.....	49
4.6. Moisture profiles for mortar with a low degree of hydration (a) without air entrainment and (b) with air entrainment. ....	50

Figure	Page
4.7. Moisture profiles for mortar with a high degree of hydration (a) without air entrainment and (b) with air entrainment. ....	50
5.1. Plan view of the Neutron Imaging Facility at NIST .....	60
5.2. Experimental set up for chloride ponding tests.....	61
5.3. Image analysis procedure for determining the average depth of penetration. (a) Background-normalized images were (b) converted to binary. (c) A mask of vertical lines was subtracted from the binary images to result in (d) 10 measurable lines of the fluid front. ....	62
5.4. (a) Influence of mortar thickness on optical density. The shaded region is the total porosity of the four mortar samples used. (b) Relationship between the degrees of saturation as determined by neutron radiographs and by mass. ....	65
5.5. Average depth of penetration of four concentrations of CaCl <sub>2</sub> solution for mortars composed of (a) w/c of 0.36 and Type I cement, (b) w/c of 0.42 and Type I cement, (c) w/c of 0.50 and Type I cement, and (d) w/c of 0.42 and Type V cement.....	66
5.6. Normalized sorptivity with an increase in CaCl <sub>2</sub> concentration in the ponded fluid. Sorptivity values were normalized to those of DI water for each respective mortar. ....	67
5.7. Degree of saturation when exposed to deionized water for mortar with (a) w/c of 0.36 with Type I cement, (b) w/c of 0.42 with Type I cement, (c) w/c of 0.50 with Type I cement, and (d) w/c of 0.42 and Type V cement. ....	71
5.8. Degree of saturation when exposed to 10% CaCl <sub>2</sub> solution for mortar with (a) w/c of 0.36 with Type I cement, (b) w/c of 0.42 with Type I cement, (c) w/c of 0.50 with Type I cement, and (d) w/c of 0.42 and Type V cement.....	72
5.9. Degree of saturation when exposed to 20% CaCl <sub>2</sub> solution for mortar with (a) w/c of 0.36 with Type I cement, (b) w/c of 0.42 with Type I cement, (c) w/c of 0.50 with Type I cement, and (d) w/c of 0.42 and Type V cement.....	73
5.10. Degree of saturation when exposed to 29.8% CaCl <sub>2</sub> solution for mortar with (a) w/c of 0.36 with Type I cement, (b) w/c of 0.42 with Type I cement, (c) w/c of 0.50 with Type I cement, and (d) w/c of 0.42 and Type V cement. (Note change in x-axis scaling) .....	74
5.11. Increase in degree of saturation of mortars exposed to deionized water up to 96 h. ....	75

Figure	Page
6.1. Experimental set-up for neutron radiography at the Neutron Imaging Facility. The top aluminum was removed at the start of the drying experiment. ....	83
6.2. (a) equilibrium water content for mortar saturated in water or in 5 % SRA solution (standard deviation within 0.1 and 0.9% in the RH range analyzed, based on two desorption tests performed on water saturated samples); (b) normalized mass and RH versus time during vapor desorption testing. ....	86
6.3. Experimental and modeled desorption isotherms for a cementitious mortar saturated in water and 5 % SRA solution, presented in terms of volumetric degree of saturation (DOS by volume).....	88
6.4. Diffusion coefficient with respect to RH evaluated from desorption data for samples saturated in water and 5 % SRA solution .....	89
6.5. Average moisture profile in terms of degree of saturation for mortar samples drying from one edge for a system saturated in (a) lime water and (b) 5% SRA solution. ....	92
6.6. Relation between DOS, RH and capillary pressure in the systems containing water and SRA.....	93
6.7. Change in the DOS in the first 12 mm from the drying surface in a mortar saturated in lime water (a,b,c,d,e) and in a mortar saturated in 5 % SRA (aa,bb,cc,dd,ee) solution at (a, aa) 30 min, (b, bb) 2.5 h, (c, cc) 6 h, (d, dd) 16 h and (e, ee) 48 h after being exposed to the drying environment. ....	94

## ABSTRACT

Lucero, Catherine L. M.S.C.E., Purdue University, May 2015. Quantifying Fluid Transport in Cementitious Materials Using Neutron Radiography. Major Professor: W. Jason Weiss.

A portion of the concrete pavements in the US have recently been observed to have premature joint deterioration. This damage is caused in part by the ingress of fluids, like water, salt water, or deicing salts. The ingress of these fluids can damage concrete when they freeze and expand or can react with the cementitious matrix causing damage. To determine the quality of concrete for assessing potential service life it is often necessary to measure the rate of fluid ingress, or sorptivity. Neutron imaging is a powerful method for quantifying fluid penetration since it can describe where water has penetrated, how quickly it has penetrated and the volume of water in the concrete or mortar. Neutrons are sensitive to light atoms such as hydrogen and thus clearly detect water at high spatial and temporal resolution. It can be used to detect small changes in moisture content and is ideal for monitoring wetting and drying in mortar exposed to various fluids.

This study aimed at developing a method to accurately estimate moisture content in mortar. The common practice is to image the material dry as a reference before exposing to fluid and normalizing subsequent images to the reference. The volume of water can

then be computed using the Beer-Lambert law. This method can be limiting because it requires exact image alignment between the reference image and all subsequent images. A model of neutron attenuation in a multi-phase cementitious composite was developed to use in cases where a reference image is not available. The attenuation coefficients for water, un-hydrated cement, and sand were directly calculated from the neutron images. The attenuation coefficient for the hydration products was then back-calculated. The model can estimate the degree of saturation in a mortar with known mixture proportions without using a reference image for calculation.

Absorption in mortars exposed to various fluids (i.e., deionized water and calcium chloride solutions) were investigated. It has been found through this study that small pores, namely voids created by chemical shrinkage, gel pores, and capillary pores, ranging from 0.5 nm to 50  $\mu\text{m}$ , fill quickly through capillary action. However, large entrapped and entrained air voids ranging from 0.05 to 1.25 mm remain empty during the initial filling process. In mortar exposed to calcium chloride solution, a decrease in sorptivity was observed due to an increase in viscosity and surface tension of the solution as proposed by Spragg et al 2011. This work however also noted a decrease in the rate of absorption due to a reaction between the salt and matrix which results in the filling of the pores in the concrete.

The results from neutron imaging can help in the interpretation of standard absorption tests. ASTM C1585 test results can be further analyzed in several ways that could give an accurate indication of the durability of the concrete. Results can be reported in depth of penetration versus the square root of time rather than  $\text{mm}^3$  of fluid per  $\text{mm}^2$  of exposed

surface area. Since a known fraction of pores are initially filling before reaching the edge of the sample, the actual depth of penetration can be calculated. This work is compared with an ‘intrinsic sorptivity’ that can be used to interpret mass measurements.

Furthermore, the influence of shrinkage reducing admixtures (SRAs) on drying was studied. Neutron radiographs showed that systems saturated in water remain “wetter” than systems saturated in 5% SRA solution. The SRA in the system reduces the moisture diffusion coefficient due an increase in viscosity and decrease in surface tension. Neutron radiography provided spatial information of the drying front that cannot be achieved using other methods.



## CHAPTER 1. INTRODUCTION, OBJECTIVES, AND ORGANIZATION

### 1.1 Introduction

Concrete pavements are designed to last between 30 and 50 years. While most pavements perform at their anticipated level, some have shown premature deterioration, especially at the joints. This damage decreases the service life of the pavement which results in costly repairs and disruption to the traveling public. A possible cause of this deterioration is associated with fluid ingress which can potentially lead to freeze thaw damage, salt precipitation or damaging chemical reactions. There is a need to better understand fluid transport and the degree of saturation as it varies from location to location in thick sections.

There is a relationship between the degree of saturation and the freeze thaw performance [1], [2]. Once concrete reaches the critical degree of saturation, approximately 86%, damage will occur due to expansive ice formation leading to a decrease in relative stiffness ( $E/E_0$ ) during freezing. If the concrete remains below the critical degree of saturation, it can withstand many freeze thaw cycles without damage. This thesis compares the degree of saturation and rate of fluid penetration in mortars with and without entrained air. By gaining a better understanding of the rate that each type of pores fill (i.e., capillary and entrained air), concrete mixtures can be designed to contain enough entrained air to remain below the critical degree of saturation and perform well in freeze thaw cycles.

In addition to damage caused by expanding water in pores upon freezing, many concrete pavements are exposed to deicing salts (including sodium chloride, calcium chloride and magnesium chloride). The addition of chlorides to the solution will influence the absorption rate in two ways: by altering the fluid properties and by reacting with the cement matrix and filling pores with a new product. Farnam et al. have studied the effect of calcium chloride on the transport properties of mortar [3], [4]. ASTM C1585 [5] absorption results were corrected for fluid properties (including density, viscosity and surface tension) and porosity to calculate an intrinsic absorption, or an indication of the depth of penetration. In this thesis, the actual depth of fluid penetration can be determined using neutron radiography.

Shrinkage Reducing Admixtures (SRAs) are increasingly being used in concrete as a method to minimize shrinkage and restrained shrinkage cracking. SRAs reduce shrinkage by decreasing the surface tension of the pore solution; however, SRAs also impact the fluid viscosity, contact angle and density. The changes in fluid properties alter the transport properties of the mortar. Neutron radiography was used to compare the drying process in mortars saturated with lime water and 5% SRA solution.

## 1.2 Research Objectives

The main objectives of the thesis include:

- Develop a model to estimate the moisture content (in terms of degree of saturation) in neutron radiographs of mortar.

- Gain a better understanding which pores (gel, capillary or air) are filled during the stages of wetting
- Relate the degree of saturation with the pores that are filled
- Investigate the influence of  $\text{CaCl}_2$  concentration on sorptivity in terms of fluid properties (viscosity and surface tension) and reactions within the cement matrix.
- Compare drying behavior in cementitious systems with and without shrinkage reducing admixtures (SRAs)

### 1.3 Organization and Contents of Thesis

This thesis serves to present work on fluid transport and neutron imaging of cement-based mortars.

The second chapter gives a brief overview of the principles of neutron imaging and how they compare to the more widely used x-ray imaging techniques. In addition, it summarizes previous research on absorption in porous media and cementitious materials using x-ray and neutron imaging.

The third chapter investigates water absorption in air entrained and non air entrained mortar. The penetration depth was monitored with neutron radiography for 12 hours. This true penetration depth is related to the value of absorption ( $\text{mm}^3/\text{mm}^2$ ) obtained in ASTM C1585 based on the percentage of pores that are filled as determined by neutron imaging.

The fourth chapter quantifies the degree of saturation in air entrained and non air entrained mortars exposed to water. A model based on the Beer-Lambert law was developed to analyze images to calculate the degree of saturation within the mortar. This model allows for flexibility in experiments and saves time imaging because it does not require a reference image in the dry state. This work determined that as water moves through mortar, only small pores in the cement matrix are filling while the large entrapped and entrained air voids remain empty. Moisture profiles quantifying the amount of water in the pores were generated. This chapter was used to develop a paper published in 2015 titled “Using Neutron Radiography to Quantify Water Transport and the Degree of Saturation in Entrained Air Cement Based Mortar” [6]. The contributions of Mr. Dale Bentz, Dr. Daniel Hussey, Dr. David Jacobson and Prof. Jason Weiss are greatly acknowledged.

The fifth chapter investigates deleterious reactions between a common deicing salt, calcium chloride, and OPC mortar. An increase in chloride concentration results in a decrease in the rate of fluid penetration. Aside from the increase in surface tension and viscosity, there is a formation of Friedel’s and Kuzel’s salts in addition to calcium oxychloride that further hinders the absorption of fluid. This chapter was used to develop a paper to be published in 2015 titled “Using neutron radiography to measure the absorption of calcium chloride solution in mortar” [7]. The contributions of Mr. Robert Spragg, Mr. Dale Bentz, Dr. Daniel Hussey, Dr. David Jacobson and Prof. Jason Weiss are greatly acknowledged.

Drying in mortar was also investigated. Since neutron radiography has the ability to detect small changes in fluid content at high spatial and temporal resolution, it can be used to capture the small changes in the moisture gradient upon drying. The stress in the drying system can also be calculated from the degree of saturation along the drying front. Mortars saturated in shrinkage reducing admixtures (SRAs) and lime water were exposed to a drying environment and monitored over 96 hours. SRAs are used to increase concrete durability by decreasing the surface tension which decreases the stress developed within the hydrating paste, but they also increase the durability of concrete by decreasing the diffusion coefficient. The neutron radiography data from this chapter was featured in a paper published in 2015 titled “Neutron Radiography Evaluation of Drying in Mortars with and without Shrinkage Reducing Admixtures” [8]. The contributions of Ms. Chiara Villani, Mr. Dale Bentz, Dr. Daniel Hussey, Dr. David Jacobson and Prof. Jason Weiss are greatly acknowledged.

## CHAPTER 2. BACKGROUND ON THE USE OF NEUTRON IMAGING IN POROUS MEDIA RESEARCH

### 2.1 Assessing Moisture Content in Cementitious Materials Using X-Ray Imaging

All radiographic methods, including the use of X-rays or neutrons, are based on the same principle of radiation attenuation upon passing through matter. Equation 2.1 described the basic law of radiation attenuation or Beer's Law [9].

$$I = I_0 \cdot e^{-\mu t} \quad \text{Equation 2.1}$$

where  $I$  is the measured intensity,  $I_0$  is the incident intensity,  $\mu$  is the attenuation coefficient of the material and  $t$  is the material thickness. The principle is depicted in Figure 2.1. Since Beer's law is applicable to X-ray and neutron imaging, experimental methods and analysis from previous x-ray studies can be applied to neutron imaging studies.

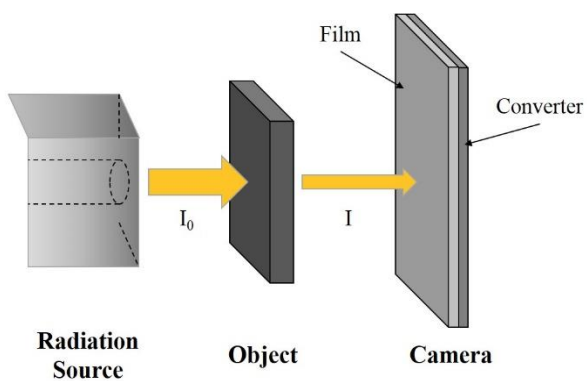


Figure 2.1 Principal components of an X-ray or neutron radiography system.

The difference between X-ray imaging and neutron imaging is the part of the atom that the radiation interacts with. X-rays interact with the electron shell of the atom [10] while neutrons interact with the nucleus. Therefore, the more electrons an atom has, the higher probability for X-ray interaction. Metals with high atomic numbers and density, such as lead, have high X-ray attenuation coefficients and appear clearly in radiographs. However, X-rays interact weakly with light atoms such as hydrogen [11].

Researchers have used X-rays to assess moisture movement in cementitious materials. Sant et al. [12] assessed fluid ingress in cement pastes using x-ray attenuation. In this work both deionized water and shrinkage reducing admixture (SRA) solutions were used. Cement pastes at high (47%) and low (10%) degrees of hydration were exposed to DI water and 5% SRA. The fluid ingress was quantified in terms of moisture content (MC) ( $\text{m}^3_{\text{fluid}}/\text{m}^3_{\text{sample}}$ ). The MC can be related to the normalized X-ray intensity by Equation 2.2.

$$MC = \frac{\ln\left(\frac{I_{wet}}{I_{dry}}\right)}{(-\mu_w t)} \quad \text{Equation 2.2}$$

where  $I_{dry}$  is the intensity of radiation transmitted through a dry material,  $I_{wet}$  is the intensity of radiation transmitted through material containing moisture,  $\mu_w$  is the attenuation coefficient of water, and  $t$  is the thickness of the material.

It was seen from the x-ray images, which were normalized to the paste in the dry state, that the depth and rate of penetration of the SRA was lower than that of the deionized water. A reduction in surface tension in a fluid will cause a reduction in penetration depth [13], [14].

The depth of penetration of the less hydrated samples was greater than that of the more mature samples due to the greater porosity in the paste [15]. This work used the moisture profile to determine diffusivity by the Boltzmann-Matano method [16]–[18].

Pour-Ghaz et al. performed a similar study using mortar rather than paste [19]. In this work water ingress was monitored in a notched specimen in attempt to quantify the effect of cracks on fluid transport. The attenuation coefficient of water ( $\mu_w$ ) was experimentally derived by imaging known thicknesses of water and measuring the intensity. The normalized intensity (normalized to a dry container with no water) was then plotted against the known thickness and  $\mu_w$  was determined as shown in [figure]. Notches were sawed into the mortar samples and a 1 mm diameter x-ray beam was used to measure the attenuation at various points. The normalized water content was determined using Equation 2.3

$$\Theta = \frac{\theta - \theta_r}{\theta_s - \theta_r} \quad \text{Equation 2.3}$$

where  $\Theta$  is the normalized moisture content,  $\theta$  is the moisture content at the measured point ( $\text{m}^3_{\text{fluid}}/\text{m}^3_{\text{sample}}$ ),  $\theta_s$  is the moisture content of a completely saturated sample, and  $\theta_r$  is the residual moisture content in an oven dried sample. For practical purposes,  $\theta_r$  is considered to equal zero. Mortar samples were notched with a saw and ponded with water or shrinkage reducing admixture solutions. The notch geometry allowed the measurement of horizontal and vertical water penetration. The samples were imaged and the normalized moisture content was evaluated at each point. Richard's equation was used to model the Darcian flow through the unsaturated, uniform, isothermal porous medium. Models of fluid transport in concrete are generally modeled with Darcian flow and an expansion of the



Richards equation. While these models are generally applicable, many anomalies are observed. For example, the Richards equation does not consider air voids in the system. Along with the fact that concrete is a heterogeneous material, the  $t^{1/2}$  linear relationship does not always hold true [20]. In this work, fitting parameters were input in the FEA package, HYDRUS with saturated boundary conditions at the notch. The x-ray results were compared to the numerical model. The model fit well in the vertical direction but tended to overestimate depth of penetration in the horizontal direction. The model fit acceptably with the measured data.

X-ray tomography is useful for determining pore structure at a high resolution [21]. Trtik et al. used a combination of x-ray and neutron tomography to investigate the release of curing water into hydrating cement paste. It was found that while it was possible to view the water movement with x-rays, the contrast and resolution wasn't sufficient. Instead, x-ray tomography was used to characterize the microstructure of the lightweight aggregate (LWA) and define boundaries between the LWA and cement paste. 901 projections were taken of two LWA particles. The reconstructed dataset had an 8.57  $\mu\text{m}$  voxel size. This dataset was registered to the neutron tomography datasets and the boundaries of the aggregate and paste were defined. From the analysis of the microstructure it was found that the solid parts (i.e. pores smaller than approximately 16  $\mu\text{m}$ ) contained more water than the porous parts of the LWA.

## 2.2 Assessing Moisture Content in Various Porous Media Using Neutron Radiography and Tomography

A neutron beam's ability to accurately detect water in-situ makes it ideal for many applications. Early research utilizing neutron imaging was associated with hydrogen fuel cells. Extensive work by researchers at the National Institute of Standards and Technology (NIST) in Gaithersburg, MD has been done to accurately quantify small amounts of water [22]–[24]. Hussey et al [22] described the quantification and calibration of water at the Neutron Imaging Facility (NIF) at NIST. To determine the coefficient of attenuation through water, an aluminum holder with various known thicknesses was imaged. The optical density, defined in Equation 2.4 was measured and plotted against the thickness.

$$OD = -\ln\left(\frac{I_{wet}}{I_{dry}}\right) = -\mu_w t_w \quad \text{Equation 2.4}$$

At low quantities of water, the relationship is linear but becomes nonlinear with large quantities of water. The data was fit with a non-linear least-squares fit. The attenuation coefficient is determined to be  $0.38483 \text{ mm}^{-1}$  and the non-linear  $\beta$  coefficient is  $-0.00947 \text{ mm}^{-2}$ .

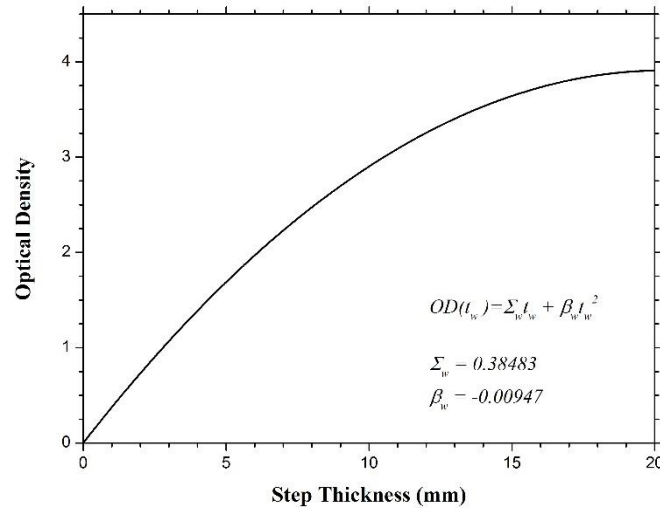


Figure 2.2 Optical density as a function of water (step) thickness used to calculate the attenuation coefficient of water. After Hussey et al. [22]

There were various systematic errors identified in which less water was observed than was actually present. These errors included beam hardening, residual water, membrane swelling, and the finite image resolution. Beam hardening is seen in Figure 2.2 where the trend becomes nonlinear at high thicknesses of water. This error is remedied with the addition of the  $\beta$  coefficient. The second source of error occurs when there is residual water in the “dry” reference image that isn’t accounted for in the “wet” image. Error due to the finite resolution can be accounted for with the correct point-spread function (PSF). It was determined that a Voight model was the best fit compared to a Lorentzian or a Gaussian. A 10-step protocol for imaging fuel cells in situ was developed in order to minimize the systematic error and accurately account for all the water.

Aside from hydrogen fuel cells, neutron radiography has been very successful in quantifying water in various porous materials [25]–[27]. Oswald et al. [28] studied the

infiltration of water in soil as well as root uptake of water. The attenuation coefficient of water was determined experimentally by imaging samples with a known volume of water. This calibration yielded an excellent fit of neutron transmission calculations and known water contents. For each experiment, a known volume of water was introduced to the plant and soil system. The samples were imaged over a period of days, mapping the water infiltration into the soil and root uptake. The experiment showed that the images generally overestimated the amount of water added to the system, presumably due to the hydrogen containing components in the roots and soil. No reference images in the “oven dried” state were obtained for reference, however, images were taken of plain dry soil (no plants) and the average intensity was used for normalization.

Researchers have investigated wetting and drying processes using neutron radiography. Early studies by de Beer et al. used neutron radiography to assess the durability of concrete [29]–[31]. The characteristics evaluated were porosity, sorptivity, and permeability. The objective of the study was to determine the ability of neutron radiography to calculate these characteristics compared to conventional standards and methods. The porosity measurements were generally underestimated compared to the lab measurement, but they followed the same trend and were considered comparable. The sorptivity was calculated by measuring the rate of water penetration with respect to the square root of time. In the lab, concrete was exposed to water and mechanically split to reveal the moisture front. The neutron radiographs slightly overestimated the sorptivity coefficient compared to the lab tests. Overall, neutron radiography was found to be a good indicator of absorption and porosity and it was favorable to lab testing because it was quicker and more repeatable.

Tomography is a powerful imaging technique because it allows researchers to see a 3-D model of the contents of a specimen. Vontobel et al. described the experimental set up and potential applications of neutron tomography [32]. The paper states that neutron tomography is mainly applied for objects in the size in the centimeter range and it can provide macroscopic information about material composition and object morphology. The author notes that neutron imaging can be used complimentary with x-ray tomography because the different beams detect different atoms. There are various parameters that influence the resolution of the image including the collimation ratio ( $L/D$ ). The thickness of the neutron scintillator screen as well as the distribution of neutrons scattered in the object or the detector box and reaching the scintillator screen also affects the resolution of the images. The tomography procedure takes a considerable amount of time due to the number of projections required.

Heller et al. at Pennsylvania State University used neutron tomography to calculate quantities of water and compute the error in the method of determining volumes of water [33]. Aluminum vessels of known dimensions were filled with water and imaged. The images were reconstructed using Octopus reconstruction software. It was found that the most accurate way to calculate the mass of water was to normalize the image to the reference grey level and multiply each voxel by the mass of water per voxel. This method yielded a 1.3% error. The mass of water was also calculated from radiographed images. Those calculations yielded a -0.1% error from the theoretical mass. A noted downside to using the reference gray levels include the time needed to scan an empty aluminum holder

as well as one filled with water. It would be preferable to improve other methods so only one set of images is needed.

Neutron tomography has been used to analyze water dynamics in columns of sand [34]. The research goal was to analyze structural effects on the fluid dynamics by measuring the 3D water content distribution in a heterogeneous (both fine and coarse) sand column during two drainage-wetting cycles using neutron transmission tomography. This method is ideal for research in soil physics because the best way to determine the connectivity of a heterogeneous medium is to directly measure it in a nondestructive way. A 5 cm x 5 cm x 4.2 cm column with 6 layers of 67% coarse and 33% fine sand was connected to a water reservoir that could vary in the z-direction to vary the pressure head. The imaging process was rapid – 280 projections were acquired in 56 seconds. The volumetric water content was determined during the wetting and drying processes. The top layer had the lowest water content and the lower levels had the highest water content. The fine sand had a higher moisture content compared to the coarse sand. Based on the spatial and temporal distribution of water, it was concluded that the drainage was most efficient where coarse sand was connected to the top of the column. Coarse sand without connections to the top drained less and later compared to the continuous coarse sand. It was also seen that coarse sand surrounded by fine sand could not be fully saturated even during slow wetting processes. The experimental data was compared to a numerical model created using HYDRUS software based on the Richard's equation. They differed greatly but it was due to the way the effects of connectivity are expressed in the Richard's equations versus other models.

Recently research has been done using neutron tomography to monitor water absorption in lightweight aggregate for internal curing of concrete [13]. This research was done in conjunction with x-ray tomography. By combining the strengths of both methods, a complete understanding of pore structure as well as fluid movement was achieved. 6mm diameter cylindrical samples of cement paste with two lightweight aggregate (LWA) particles placed in the center were imaged with 46 projections. The low number of projections was due to time sensitivity of the experiment as the paste was hydrating. Each tomography scan took approximately 10 minutes. The top LWA particle was inserted dry and the bottom was inserted pre-soaked. The images showed water uptake and later release of water into the paste by the dry LWA. The pre-soaked LWA released water into the paste throughout the hydration time. This water was quantified by segmenting the voxels identified as LWA and analyzing the mean grey level. The mean grey level was normalized to that of a dry LWA particle. It was previously calculated that there was  $8.27 \times 10^{-10}$  g of water per grey level per voxel. The research achieved two goals: quantifying the water absorbed and released in LWA and cement paste during the hydration process and quantifying the distance curing water travels through the paste.

### 2.3 Summary

Advances in neutron imaging can be applied to the study of fluid transport in concrete. Neutron imaging has been successful in applications such as mapping water flow in hydrogen cells and other porous material such as soil. Early studies using x-ray attenuation to image water absorption in concrete provide a strong baseline for further research to be modeled from. Currently, methods for determining degree of saturation and water content

are based on mass measurements. Neutron imaging allows for an accurate quantification of water content both spatially and temporally which cannot be achieved by simple mass measurements. This method is also much less time consuming and requires fewer samples to determine the water front over time. Instead of testing numerous samples and cutting them open at various times, one sample can be imaged while immersed in water. Neutron radiography and tomography have proven to be very accurate in determining in situ water content which allows for a very accurate quantification of absorbed water volume and degree of saturation. A more accurate understanding of fluid absorption in concrete is essential in creating more durable materials.



## CHAPTER 3. MONITORING FLUID PENETRATION AND QUANTIFYING MOISTURE CONTENT IN MORTAR USING NEUTRON RADIOGRAPHY

### 3.1 Abstract

This study aims to achieve three goals: to measure the depth of water penetration during the first 12 h of exposure, to quantify the local degree of saturation in the moisture front, and to relate the change in mass to the depth of fluid ingress in air entrained and non-air entrained mortar. Mortars with varying degrees of hydration and air content were imaged using neutron radiography at the Neutron Imaging Facility (NIF) at the National Institute of Standards and Technology (NIST) in Gaithersburg, MD. Neutron imaging was used due to its ability to detect small changes in water content with a high spatial and temporal resolution. It is hypothesized that the water front penetrating the mortar is not completely saturated, rather, the gel and capillary pores fill first and the large entrapped and entrained air voids remain empty as the water continues to penetrate through the mortar. In this investigation, mortar samples were exposed to water and wrapped in aluminum tape to ensure one directional flow. The volume of the water absorbed in the pores was calculated from the radiographs and used to assess the effect of entrained air on the degree of saturation over time. It was found that the air voids do not saturate within the first 12 hours of absorption. The addition of air entrainment decreased the degree of saturation in the specimen while not having a significant effect on the depth of fluid penetration.

### 3.2 Introduction

The freeze-thaw durability of concrete is related to the degree of saturation [35]. It has been shown that when the degree of saturation reaches a critical level (80 to 91%) freeze-thaw damage is unavoidable [1], [2], [35]. The degree of saturation is often measured in a macroscopic sense. However in thick sections there is a need to better understand how the degree of saturation varies from location to location.

The most typical measures of the degree of saturation are based on gravimetric methods such as ASTM C1585 [5]. ASTM C1585 defines the absorption in terms of  $I$ , the volume of absorbed water ( $\text{mm}^3$ ) per exposed surface area ( $\text{mm}^2$ ). The units used can be incorrectly interpreted as depth (mm). Some believe that this number quantifies the depth of fluid ingress at a given time which is an important parameter when determining service life of reinforced concrete structures. The results of this test are also highly dependent on the initial conditioning of the concrete before exposure to water [36].

One-dimensional absorption in cementitious materials is linear with respect to  $t^{1/2}$  according to Equation 3.1 [37], [38].

$$I = st^{1/2} \quad \text{Equation 3.1}$$

Where  $I$  ( $\text{mm}^3/\text{mm}^2$ ) is the cumulative water absorption,  $s$  ( $\text{mm}/\text{h}^{1/2}$ ) is the sorptivity (the rate of fluid absorption) and  $t$  is the elapsed time.

X-ray radiography has been used to evaluate water ingress in concrete and mortar [12], [19], [39]. Neutron radiography is more sensitive to hydrogen than x-ray radiography

consequently neutron radiography has the ability to resolve the volume of water with greater precision than x-ray radiography. As a result, neutron radiography is often used to quantify the moisture content in porous materials [27]–[29], [34]. This includes soil and plant roots [25], [27], [28], rock [29], [40], and parchment [41].

Several studies have used neutron radiography to examine cement pastes and mortar [42]–[44]. Specifically, Hanžič [43] measured the sorptivity of concrete exposed to water and three types of fuel oil. Hanžič [43] showed the accuracy that could be obtained from neutron radiography by comparing sorptivity radiographs with the results of a gravimetric method. De Beer [31] measured porosity and sorptivity with neutron radiography. Wittman and co-workers have measured sorptivity in mortars with and without water repelling agents [44], [45], in cracked cementitious materials [46], [47], and in cracks in strain hardening cement-based composites [46]. Overall, neutron imaging in concrete material has been found to correlate well with gravimetric methods.

The neutron imaging studies mentioned in the previous paragraph typically evaluate a transmission image by taking the ratio of an image of a sample after absorption to an image of a sample before absorption. The transmission image is powerful in that it allows water to be visually detected in the sample. This paper however extends what was done in many previous studies to perform a quantitative analysis of water content. This is based on only the knowledge of the attenuation coefficient of water [22] and other constituent materials. The attenuation coefficients can be used with the Beer-Lambert law of attenuation as shown in Figure 3.1. The beam that interacts with the sample ( $I_0$ ) can be absorbed,

scattered or attenuated. As a result the neutron beam that reaches the detector ( $I$ ) has a lower intensity than the original neutron beam ( $I_0$ ). The reduction in the intensity of the neutron beam can be described by Beer's Law using the attenuation coefficient,  $\mu$ , of the sample as shown in Equation 3.2.

$$I = I_0 e^{-\mu t}$$

Equation 3.2

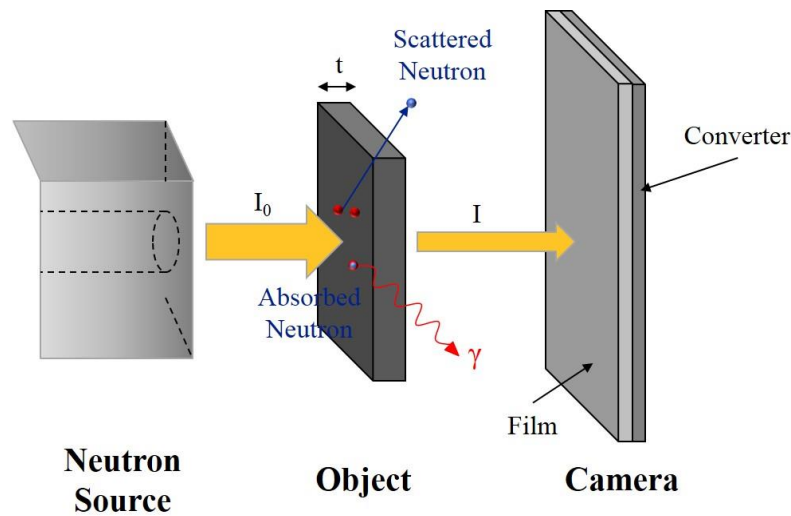


Figure 3.1. Neutron attenuation through material. An incident beam,  $I_0$ , passes through matter causing some neutrons to be absorbed, some to scatter and some to pass through resulting in the transmitted beam,  $I$ .

### 3.3 Experimental Methods

#### 3.3.1 Sample Preparation

Mortar was prepared using Type I OPC and silica quartz fine aggregate using the proportions listed in Table 3.1. BASF Micro-Air 119 was added to Mixture 0.42-AE to achieve an air content of 9 % by mortar volume. Mixing was performed in accordance with ASTM C192-13 [48]. The fresh air content was determined following ASTM C231-13 [49]. Specimen were cast in prisms (74 mm by 100 mm by 400 mm) and covered until

the times listed in Table 3.1. The remaining prisms were removed from the mold after 24 hours and sealed to continue hydration until later times listed in Table 3.1.

Table 3.1. Mixture proportions

Mixture ID	Type I OPC (kg/m <sup>3</sup> )	Water (kg/m <sup>3</sup> )	Fine Aggregate (kg/m <sup>3</sup> )	Air Content (% volume of mortar)	Time Hydrating (Sealed)	Degree of Hydration (%)
0.42-nAE	979	411	2298	5.0	16 h	34 ± 1.3
					28 d	72 ± 0.5
0.42-AE	938	394	2201	9.0	16 h	34 ± 1.3
					28 d	72 ± 0.5
0.30-nAE	1170	351	2298	6.0	18 h	34 ± 0.7
					36 h	43 ± 0.9

The mortar prisms were cut into 10 mm ± 0.7 mm slices. The slices were oven dried at 105 °C ± 5 °C for 2 d. All samples were wrapped in aluminum tape before absorption testing to ensure one-directional absorption. Three samples from each mixture and degree of hydration were used in the neutron imaging experiments.

### 3.3.2 Neutron Imaging

The imaging was performed at the Neutron Imaging Facility at the National Institute of Standards and Technology in Gaithersburg, MD. The neutron source is a 20 MW heavy-water fission reactor operated at 37 °C. The neutron beam used in this study has an aperture diameter of 10 mm, a fluence rate of 4.97x10<sup>6</sup> cm<sup>-2</sup>s<sup>-1</sup>, and a collimation ratio of 600. A LiF:ZnS scintillator and an amorphous silicon detector behind the samples converts the neutrons to light and generates an electrical signal which is recorded as a digital image with equipment outside the beam line.

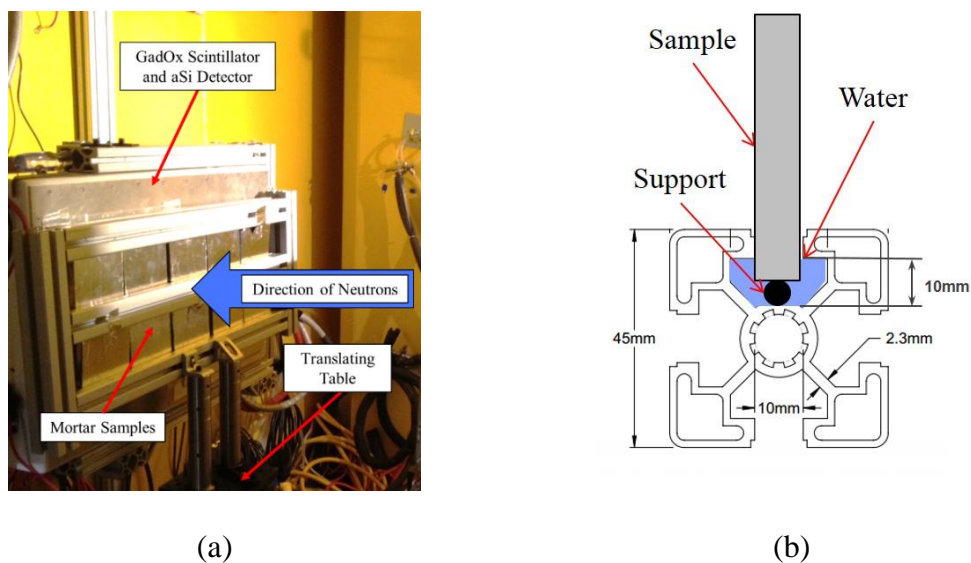


Figure 3.2. Experimental set up of absorption testing in the neutron beam chamber. (a) Aluminum holder with 10 mortar samples and (b) a sketch of the cross section of the arrangement showing the water source in the aluminum track.

Ten samples were placed in an aluminum frame filled to a level of approximately 10 mm of deionized water. In order to image all the samples, the frame was attached to a translating table that moved to three positions as shown in Figure 3.2. Images were captured at 1 frame per second for 30 s. At each location, 10 averaged images were recorded. The samples were imaged continuously, with the exception of when water was added, for 12 h.

### 3.3.3 Image Processing and Analysis

To eliminate outliers, images were combined with a median filter in groups of 3 for the series of images during water absorption. Reference images of samples prior to exposure to water were combined in groups of 10. Thirty flat field (open beam) and dark (closed beam) images were also taken and combined with a median filter. The use of a median

filter in time eliminated the appearance of streaks due to gamma rays and fast neutrons depositing energy.

All image analysis was performed using ImageJ. Images of each mortar sample during the absorption period were imported, approximately 110 images for each sample. A threshold was applied to the image and converted to binary to distinguish the wetted front (Figure 3.3b). A binary mask was created with vertical lines spaced at 10 mm as shown in Figure 3.3c. The mask was subtracted from the binary images of the moisture front to create a series of 10 line segments (Figure 3.3d). Each line segment was then measured and averaged for each image.

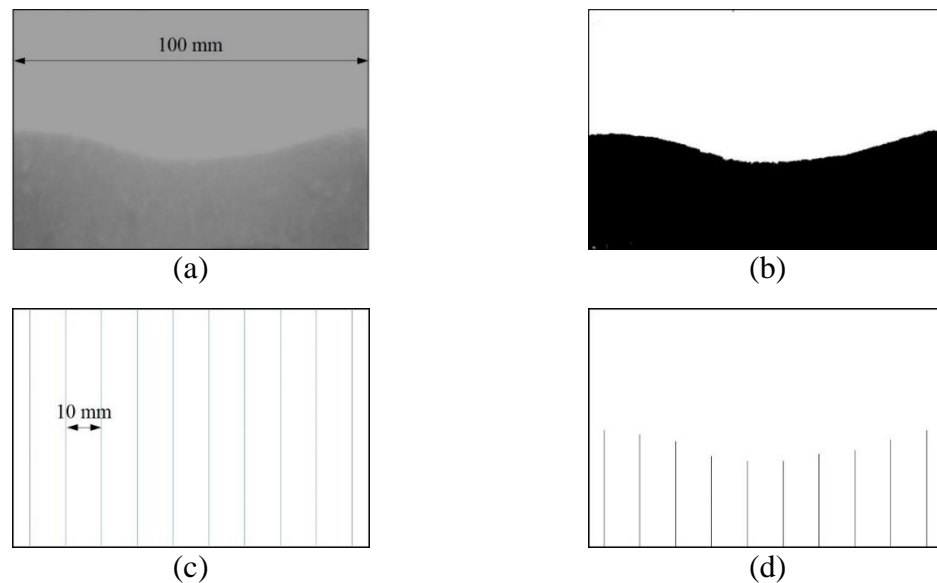


Figure 3.3. Determination of average depth of penetration from (a) normalized neutron images. (b) Images were segmented and converted to binary and a (c) mask was subtracted to (d) result in measurable line segments at 10 locations.

### 3.3.4 Gravimetric Absorption

The absorption of the mortar was determined gravimetrically using mortars with the same geometry and initial moisture condition of those used for the neutron radiography experiments. Mortar was placed on supports in approximately 2 mm of water. The mass was monitored for 12 h. Measurements were taken at 1, 5, 10, 20, and 30 m, then every hour up to 12 h. The change in mass was used to calculate the absorption,  $I$  ( $\text{mm}^3/\text{mm}^2$ ), per ASTM C1585 using Equation 3.3 [5],

$$I = \frac{m - m_0}{a \cdot d} \quad \text{Equation 3.3}$$

where  $m$  is the measured mass of the sample (g),  $m_0$  is the initial mass of the sample (g),  $a$  is the surface area exposed to the fluid ( $\text{mm}^2$ ) and  $d$  is the density of the fluid ( $\text{g}/\text{mm}^3$ ).

## 3.4 Results and Discussion

### 3.4.1 Depth of Water Penetration

The depth of fluid penetration was measured as previously described for the first 12 h of contact with fluid. Measurements at very early times and very little penetration, less than 1 h and 5 mm, were difficult to measure in some cases due to excess water trapped between the sample and the aluminum track as shown in Figure 3.4.



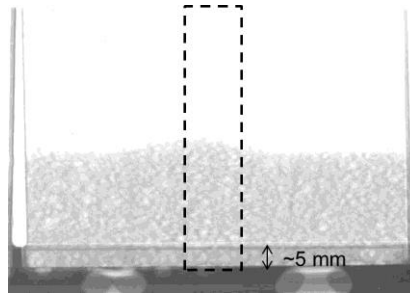


Figure 3.4 Typical radiograph used for analysis. The image of a wetted mortar has been normalized to an image in the dry state. The dashed rectangle is the area of analysis for water thickness calculations.

Figure 3.5a compares the depth of penetration in mortars with and without air entrainment. At a low degree of hydration, 34%, there is a clear difference between air entrained and non air entrained mortar, however at a high degree of hydration, 72%, there is essentially no difference between the mortars with different air contents. Interestingly, the depth of fluid at 12 h did not vary greatly between the low and high degree of hydration (between 23 mm and 26 mm of fluid penetration at 12 h). There is a decrease in pore volume with an increase in hydration, so it is expected for the 28 d samples to have a denser microstructure that would resist fluid ingress and thus decrease the rate of absorption. In the air entrained mortars, there was a 10% decrease in porosity between the mortars that cured for 16 h and those that cured for 28 d. In non air entrained mortars, there was a 20% decrease in porosity. The large volume of stable air voids in the air entrained mortar remains constant while there is a slight decrease in capillary porosity.

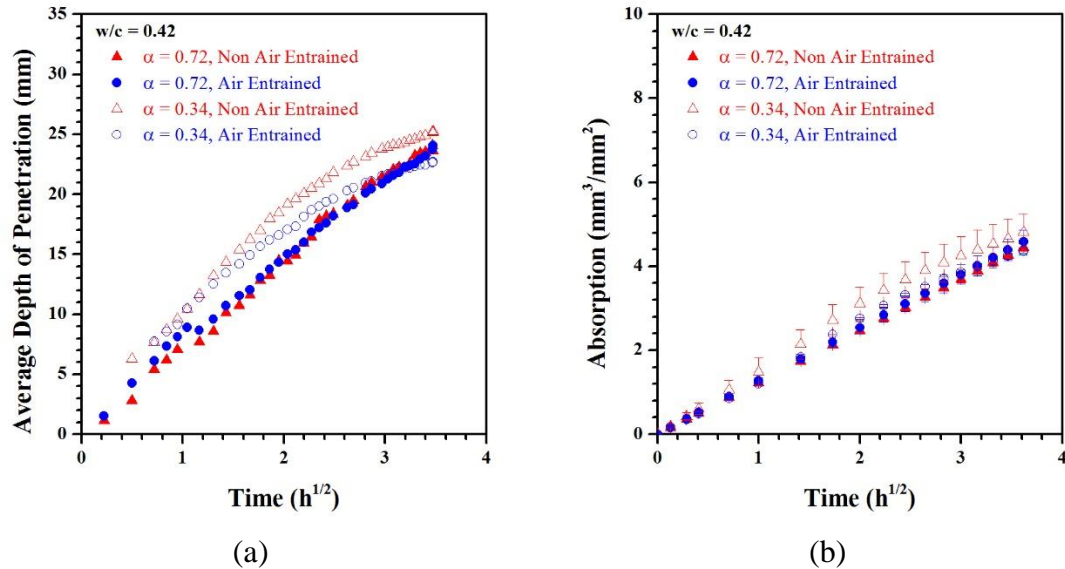


Figure 3.5. (a) Average fluid depth of penetration and (b) ASTM C1585 absorption results as determined by Equation 3.3 for air entrained and non air entrained mortar with a w/c of 0.42

From Figure 3.5 it is clear that the value for absorption ( $mm^3/mm^2$ ) is not equal to the actual depth of penetration although the units are distance. The largest difference between the actual depth of penetration and the ASTM definition of absorption can be seen in the first 6 hours (approximately  $2.44 hr^{1/2}$ ). In Figure 3.5a, the mortar with a lower degree of hydration (hollow data points) has more fluid penetration, however the change in mass is nearly the same in Figure 3.5b.

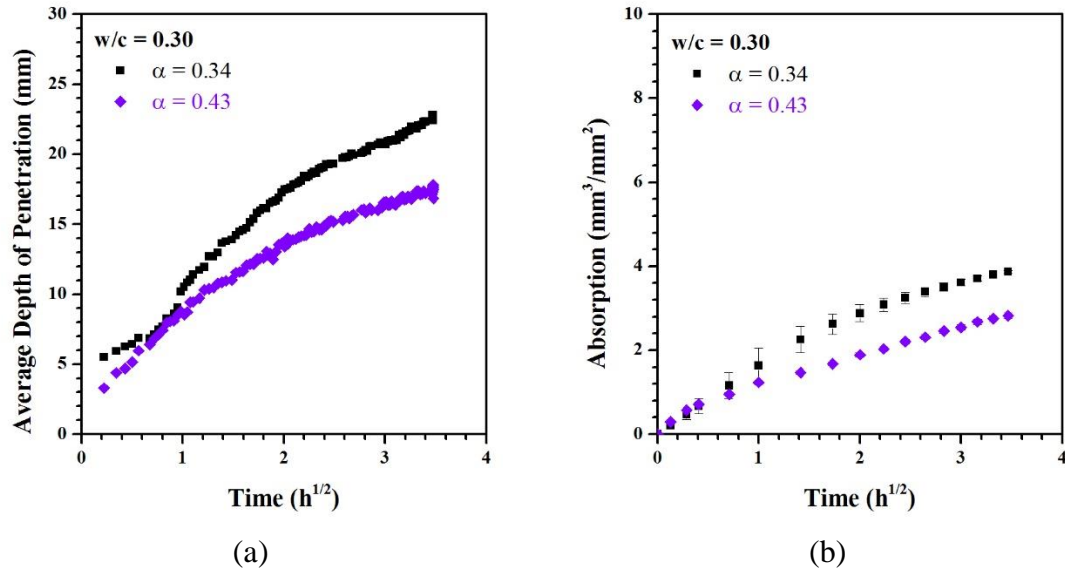


Figure 3.6. (a) Average fluid depth of penetration and (b) ASTM C1585 absorption results as determined by Equation 3.3 for air entrained and non air entrained mortar with a w/c of 0.30

Equation 3.1 predicts a linear relationship between absorbed water and the square root of time. This relationship holds true for systems at a high degree of hydration as shown in Figure 3.5a. In contrast, the mortar at a low degree of hydration (between 35 and 45%) exhibit nonlinear behavior (Figure 3.5a, and Figure 3.6a). This nonlinearity can be attributed to a decrease in porosity as well as a decrease in intrinsic permeability as the paste continues to react and create new hydration products when exposed to water [20].

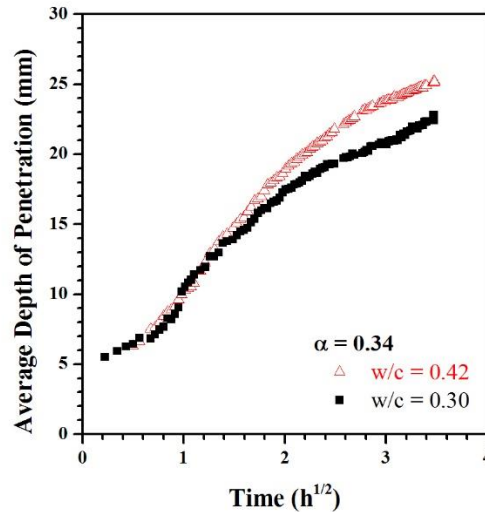


Figure 3.7 Influence of w/c on depth of water penetration in mortar with a low degree of hydration.

Figure 3.7 compares the fluid ingress in mortars with the same degree of hydration and air content and different w/c. As expected, the mixture with a 0.30 w/c has a lower rate of fluid penetration compared to the mortar with a w/c of 0.42. This is due to less capillary porosity and denser microstructure in the mixture with a lower w/c.

#### 3.4.2 Degree of Saturation

The degree of saturation along the fluid front was calculated with neutron radiography. The area of analysis used for all samples was in the middle of the mortar as shown in Figure 3.4. The change in water content in the material can be determined by normalizing an image of the mortar in the wet state to an image of the same mortar in the dry state [22], [30], [44]. Variables such as image registration errors can prevent the dry image from being accurately subtracted from the wet image. In highly heterogeneous composites such as mortar and concrete, accurately subtracting the dry image to obtain the transmission image

is crucial when measuring small quantities of water. The thickness of water ( $t_w$ ) can then be computed as

$$t_w = \frac{-\ln\left(\frac{I_{wet}}{I_{dry}}\right)}{\mu_w} \quad \text{Equation 3.4}$$

where  $I_{wet}$  is the measured intensity of the wet mortar,  $I_{dry}$  is the intensity of the dry mortar and  $\mu_w$  is the attenuation coefficient of water. The measured value of  $\mu_w$  is  $0.3808 \text{ mm}^{-1}$  [6]. The calibration curve is shown in Figure 3.8.

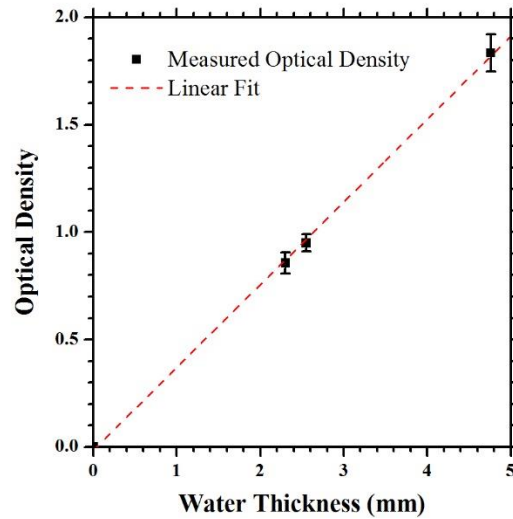


Figure 3.8. Calibration curve for water. The measured attenuation coefficient for water is  $0.3808 \text{ mm}^{-1}$

The volume of water per pixel is the thickness of water multiplied by the pixel size ( $p^2$ ) which in this experiment was  $0.01488 \text{ mm}^2$ . To compute the degree of saturation ( $S$ ), the volume of water in the pores was normalized to the total volume of pores in each pixel as expressed in Equation 3.5.

$$S = \frac{t_w \cdot p^2}{t_{sample} \cdot p^2 \cdot \phi_{total}} \quad \text{Equation 3.5}$$

where  $t_{sample}$  is the total thickness of the sample and  $\phi_{total}$  is the total porosity in volume fraction. The procedure described is accurate for mortar that is initially in the oven dried state. Since the reference image is taken when the pores are completely empty, the change in water content calculated from Equation 3.4 and Equation 3.5 represent the total degree of saturation.

Figure 3.9, Figure 3.10, and Figure 3.11 are moisture profiles of the six different mortars exposed to water. The degree of saturation as calculated with Equation 3.5 is plotted with respect to the distance from the wetting edge. The degree of saturation labeled  $S_{matrix}$  is the degree of saturation in which all the cement paste matrix pores are filled. For this calculation, gel pores, capillary pores and voids caused by chemical shrinkage in a sealed system are considered to be part of the matrix porosity. Table 3.2 summarizes the components of porosity and  $S_{matrix}$  for each mixture.  $S_{matrix}$  can be calculated from Powers model or it can be measured by vacuum saturating the mortar at different levels. The mortar specimen were placed in a vacuum chamber with deionized water and evacuated to 380 torr to fill the small voids but keep the air voids empty [52]. The samples were gently patted dry and weighed ( $m_{SS}$ ) then submerged in water and the buoyant mass was collected ( $m_{SSB}$ ). The same samples were then placed in the chamber and the vacuum was set to 6 torr. This low pressure ensures that all voids, including large air voids, and completely filled. Again, the samples were gently patted dry and weighed, then submerged in water and the buoyant mass was collected. The volume of pore space can then be calculated as:

$$V_{pores} = \frac{m_{SS} - m_{OD}}{m_{SS} - m_{SSB}} \quad \text{Equation 3.6}$$

Where  $m_{OD}$  is the oven dried mass of the sample.  $S_{matrix}$  is then the ratio of the volume of pores ( $V_{pores}$ ) when vacuumed at 380 torr to the volume of pores when vacuumed at 6 torr.

Table 3.2. Calculated and measured values for  $S_{matrix}$  for each mortar.

Mixture ID	Degree of Hydration	of	Calculated $S_{matrix}$	Measured $S_{matrix}$
0.42-nAE	0.72		77%	72%
	0.35		80%	78%
0.42-AE	0.72		62%	56%
	0.35		67%	63%
0.30-nAE	0.35		72%	69%
	0.43		71%	68%

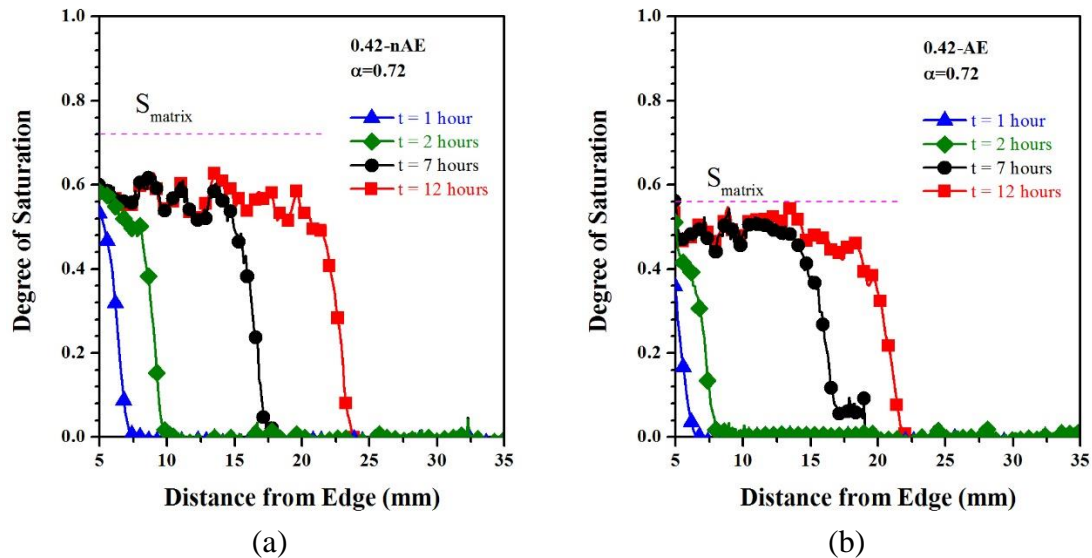


Figure 3.9. Degree of saturation with respect to distance from fluid source evaluated for (a) non air entrained and (b) air entrained mortar with a high degree of hydration.

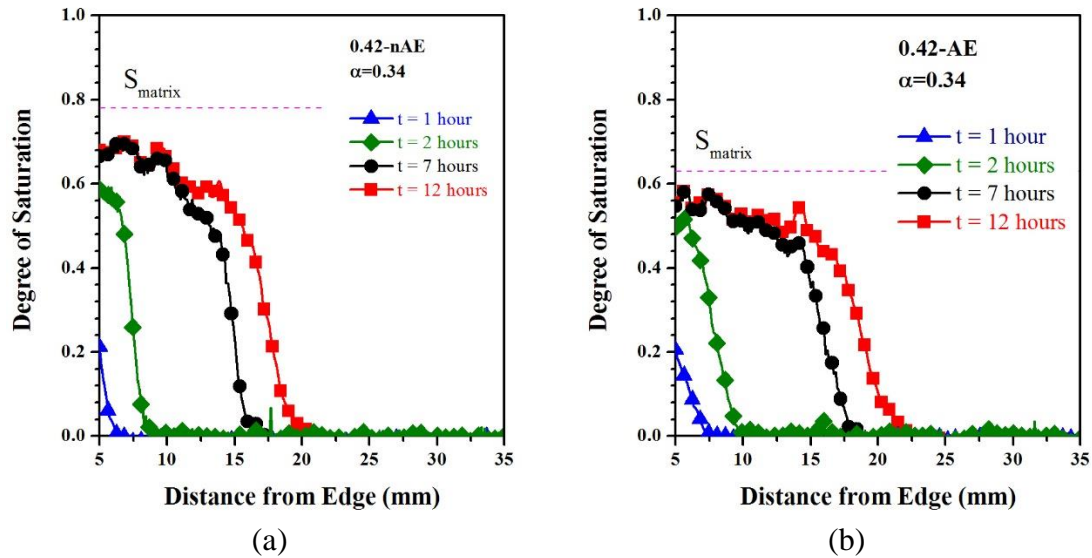


Figure 3.10. Degree of saturation with respect to distance from fluid source evaluated for (a) non air entrained and (b) air entrained mortar with a high degree of hydration.

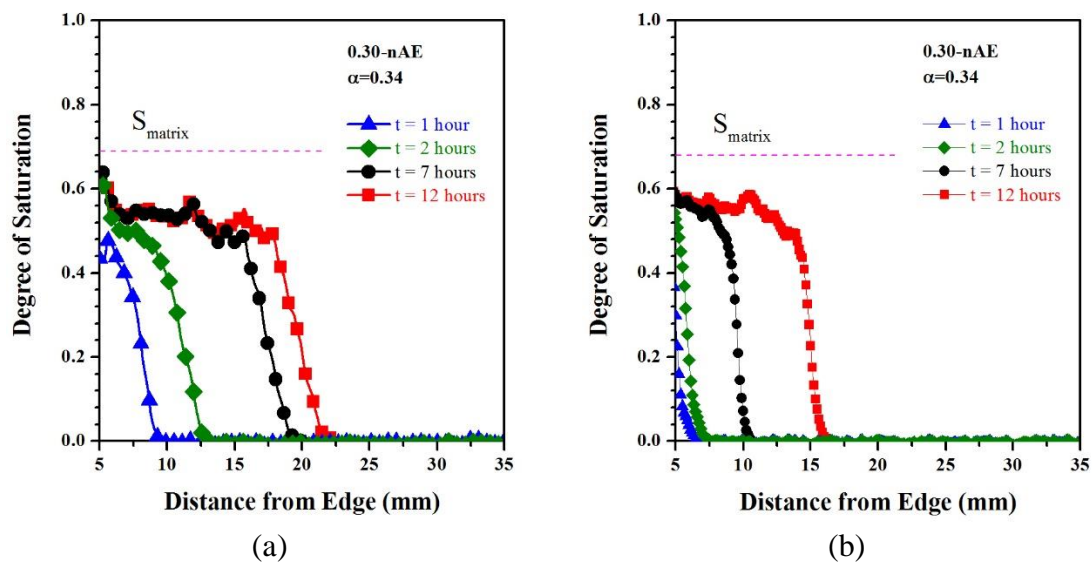


Figure 3.11. Degree of saturation with respect to distance from fluid source evaluated for mortars with a w/c of 0.30 and a degree of hydration of (a) 0.34 and (b) 0.43.

As seen from Figure 3.9 to Figure 3.11, all mortars had moisture contents less than or equal to  $S_{matrix}$  throughout the fluid front. The air voids remain empty and the fluid ingress is driven only by the capillary suction from the smaller pores. The mortar with higher air



contents have lower degrees of saturation due to a larger volume of porosity composed of air which remains empty due to very low capillary pressure generated within the large pore.

Figure 3.12 is a desorption isotherm for the mortars 0.42-nAE and 0.42-AE at a high degree of hydration. At high relative humidities, the mortar with a lower air content stays at a higher degree of saturation. At the same relative humidity, the air entrained mortar has a lower degree of saturation.

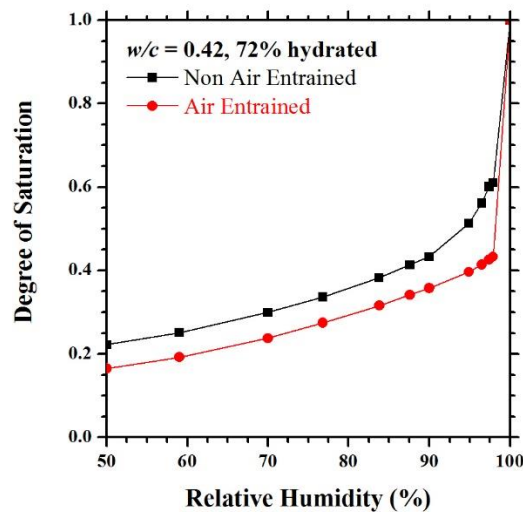


Figure 3.12. Desorption isotherm for mortar with a w/c of 0.42 and degree of hydration of 75% with and without air entraining admixture.

### 3.4.3 Intrinsic Absorption

It has been found that not all pores fill during the first 12 hours of absorption. The depth of penetration, or intrinsic absorption (mm), can be calculated by normalizing the volume of water absorbed to the surface area exposed multiplied by the volume fraction of the pores

being filled, i.e. capillary pores, gel pores, and voids resulting from chemical shrinkage in a sealed system.

The depth of penetration of water can be computed by modifying Equation 3.3. The calculated value of  $I$  can be normalized to the volume fraction of pores that are being filled listed in Table 3.2 using Equation 3.7. Figure 3.13, Figure 3.14 and Figure 3.15 show the calculated intrinsic permeability using the calculated  $S_{matrix}$  from Table 3.2.

$$I_{int\ rinsic} = \frac{m - m_0}{a \cdot d \cdot \phi_{matrix}} \quad \text{Equation 3.7}$$

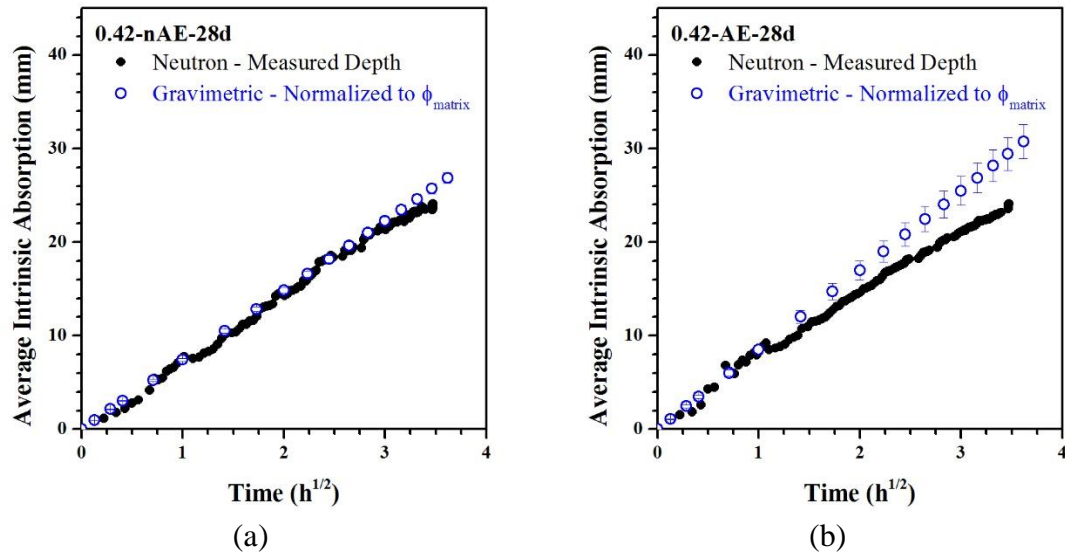


Figure 3.13. Calculated intrinsic absorption compared to measured depth of penetration evaluated for (a) non air entrained and (b) air entrained mortar with a high degree of hydration.

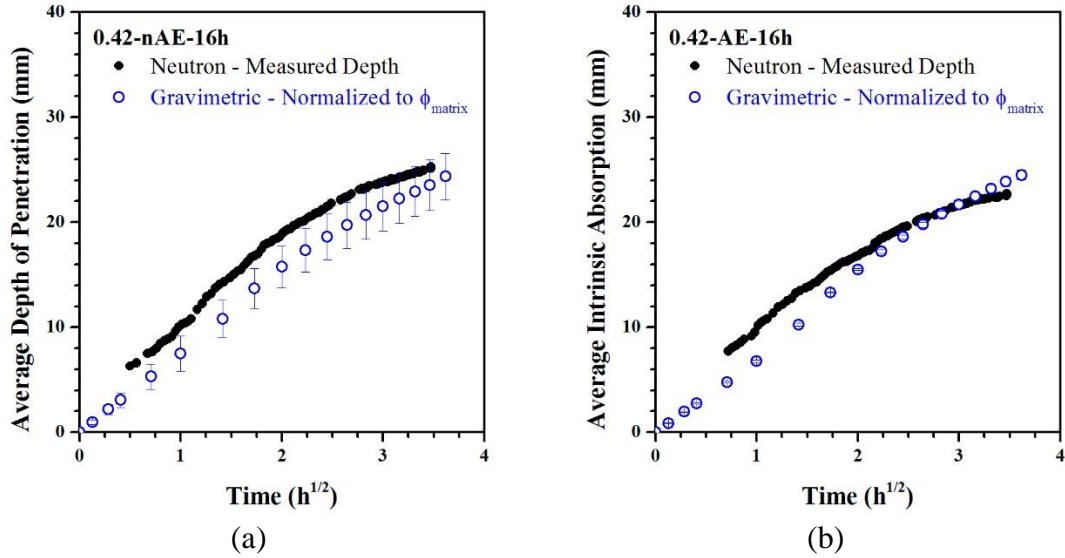


Figure 3.14. Calculated intrinsic absorption compared to measured depth of penetration evaluated for (a) non air entrained and (b) air entrained mortar with a low degree of hydration.

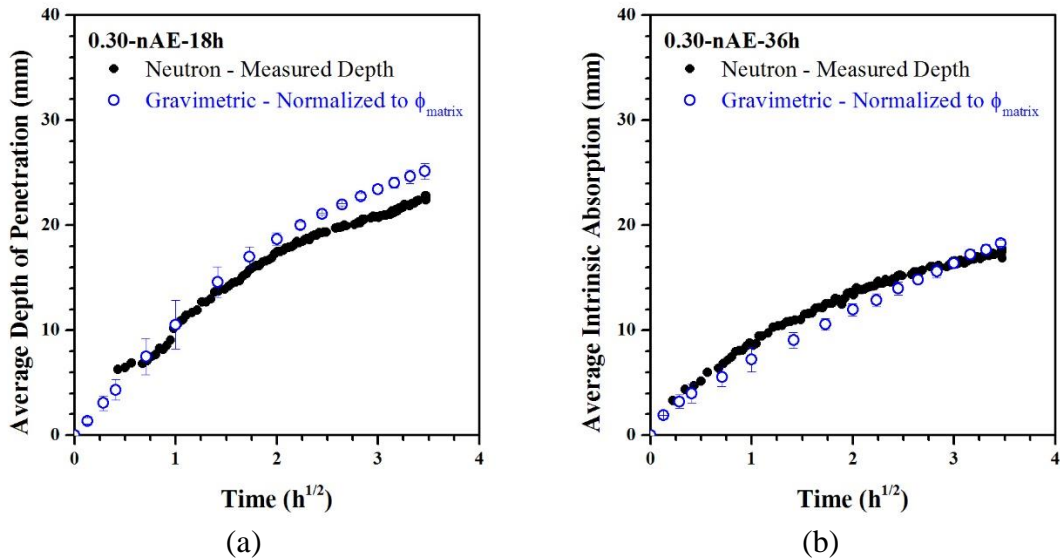


Figure 3.15. Calculated intrinsic absorption compared to measured depth of penetration evaluated for non air entrained mortar with (a) a degree of hydration of 0.34 and (b) a degree of hydration of 0.43.

Table 3.3. Measured intrinsic sorptivity of mortars exposed to water as determined from neutron radiographs and gravimetrically

Sample ID	Measured Sorptivity (mm/h <sup>1/2</sup> )	Initial Intrinsic Sorptivity (mm/h <sup>1/2</sup> )	Calculated Intrinsic Sorptivity (mm/h <sup>1/2</sup> )
0.42-nAE-28d	7.05 ± 0.60		7.42 ± 0.13
0.42-nAE-16h	8.23 ± 0.67		7.77 ± 0.61
0.42-AE-28d	6.66 ± 0.07		8.50 ± 0.42
0.42-AE-16h	7.02 ± 0.34		7.77 ± 0.03
0.30-nAE-18h	6.35 ± 0.54		8.85 ± 0.05
0.30-nAE-36h	4.46 ± 0.53		5.32 ± 0.06

The initial sorptivity as defined by ASTM C1585 as the slope of the line that is the best fit to  $I$  plotted against the square root of time for points between  $t=0$  and  $t=6$  h (approximately 2.44 h<sup>1/2</sup>). The correlation coefficient must be less than 0.98 in order for the initial sorptivity to be determined. If the correlation is poor or if there is a systematic curvature, the initial sorptivity cannot be determined [5].

Equation 3.7 is representative of the depth of penetration until the water front reaches the edge of the sample and large entrapped and entrained air voids begin to fill. The process is a piecewise function dependent on the air content of the mortar. Equation 3.7 is also only valid for oven dried mortar exposed to water. Corrections can be made to account for changes in fluid properties (such as surface tension and viscosity) as well as for initially filled porosity.

### 3.5 Conclusions

Neutron radiography was used in this study to quantify the moisture content in mortar with and without air entraining admixtures. The depth of penetration during the first 12 h was monitored of exposure to water. The fluid penetrated Mixtures 1 and 2 (mortars with a  $w/c$  of 0.42) between 23 mm and 26 mm in 12 h. However, the degree of hydration influenced the absorption behavior. The depth of penetration in the well hydrated mortars increased linearly with the square root of time while the depth of penetration was non-linear in the early-age mortars. This is likely due to the creation of new hydration products when the water is exposed to the relatively high amount of un-hydrated cement in the system. The moisture content and degree of saturation was determined along the height of the sample in the direction of fluid absorption. It was found that clearly not all the pores are filled water increasingly penetrates the mortar. The addition of entrained air lowered the degree of saturation throughout the moisture front. Air entraining admixtures effectively protect concrete and mortar from freeze thaw damage by lowering the degree of saturation and ensuring it does not surpass the critical degree of saturation. The volume of pores filled correlates to the volume of small pores (matrix porosity excluding large air voids). With this information, the analysis of absorption tests like ASTM C1585 can be modified to account for the porosity being filled. This method yields results that correlate well with the actual depth of penetration measured by neutron radiography for the first 12 h of absorption.

## CHAPTER 4. USING NEUTRON RADIOGRAPHY TO QUANTIFY THE DEGREE OF SATURATION IN AIR ENTRAINED CEMENT BASED MORTAR

### 4.1 Abstract

Air entrainment is commonly added to concrete to help in reducing the potential for freeze thaw damage. It is hypothesized that the entrained air voids remain unsaturated or partially saturated long after the smaller pores fill with water. Small gel and capillary pores in the cement matrix fill quickly on exposure to water, but larger pores (entrapped and entrained air voids) require longer times or other methods to achieve saturation. As such, it is important to quantitatively determine the water content and degree of saturation in air entrained cementitious materials. In order to further investigate properties of cement-based mortar, a model based on Beer's Law has been developed to interpret neutron radiographs. This model is a powerful tool for analyzing images acquired from neutron radiography. A mortar with a known volume of aggregate, water to cement ratio and degree of hydration can be imaged and the degree of saturation can be estimated.

### 4.2 Introduction

The ability to quantify the degree of saturation in concrete is important for many durability issues. For example, freeze thaw behavior is strongly linked with the degree of saturation [35]. Once the concrete reaches the critical degree of saturation, this is approximately 86 %,

freeze-thaw damage is unavoidable [1]. Air entraining admixtures are commonly added to concrete to increase the amount of large, stable voids (0.05 mm to 1.25 mm in diameter) [53]. The degree of saturation is often measured gravimetrically; however, there is a need to better understand how the degree of saturation varies spatially throughout the specimen. In this study, neutron radiography is used to quantify the degree of saturation both spatially and temporally, which cannot be done using the current gravimetric test methods.

The goal of this research is to determine the degree of saturation of a mortar sample as a function of depth for any mortar mixture. Many researchers normalize images to an image of the same sample in a completely dry state and measure the change in water content directly if the attenuation coefficient of water is known [12], [21], [22], [30], [54]. To determine the degree of saturation, the volume of water measured must be normalized to the total pore volume. Alternatively, a model based on Beer's Law was developed to predict the degree of saturation of mortar without using a reference image in the dry state. The volume fraction of each constituent including unhydrated cement, aggregate, empty pore space and hydrated gel product can be estimated from the mixture proportions and Powers model [15] and if the attenuation coefficient of each constituent is known, the volume fraction of filled pores ( $S$ ) can be determined.

### 4.3 Experimental

#### 4.3.1 Sample Preparation

Four mortar mixtures were made with varying air content and mass-based water to cement ratios for this study. Table 1 summarizes the mixture proportions for each mortar. The

mortar was mixed in accordance with ASTM C192/C192M-13a [48]. The samples were cast in 75 mm by 100 mm by 400 mm prisms. The prisms were cured in a sealed condition at a constant temperature of  $25\text{ }^{\circ}\text{C} \pm 2\text{ }^{\circ}\text{C}$ . The degree of hydration was determined by measuring the non-evaporable water in the paste [55]. The samples were cut into 75 mm by 100 mm by 10 mm slices with a wet saw at various times to obtain specimens having the degrees of hydration listed in Table 4.1. The Mixture ID is formatted as the water to cement ratio ( $w/c$ ) and air entrainment (AE or non-AE).

Table 4.1. Mixture proportions for mortar samples used for neutron radiography

Mixture ID	Type I OPC ( $\text{kg}/\text{m}^3$ )	Water ( $\text{kg}/\text{m}^3$ )	Fine Aggregate ( $\text{kg}/\text{m}^3$ )	Air Content (% volume of mortar)	Degree of Hydration
0.42-nAE	581.0	244.0	1363.1	5.0	$0.26 \pm .023$
					$0.35 \pm .013$
					$0.65 \pm .011$
					$0.72 \pm .005$
0.42-AE	556.5	233.8	1305.7	9.0	$0.35 \pm .013$
					$0.72 \pm .005$

The samples were oven dried at  $105\text{ }^{\circ}\text{C} \pm 5\text{ }^{\circ}\text{C}$  for 2 d and weighed to determine their oven dried mass ( $m_{OD}$ ). The specimens were then placed under vacuum and evacuated to a pressure of  $930\text{ Pa} \pm 670\text{ Pa}$  ( $7\text{ torr} \pm 5\text{ torr}$ ). After 3 h, lime water was introduced to the chamber. The chamber remained under vacuum for an additional hour. The pump was then turned off and the mortar specimen remained submerged in lime water for 18 h. The samples were then gently wiped with a towel to remove surface moisture and weighed to obtain the saturated mass ( $m_{SS}$ ). The total volume of pores ( $V_{total}$ ) is the difference between the mass of the sample completely saturated and oven dried. The density of water is assumed to be  $1.0\text{ g}/\text{cm}^3$ .



$$V_{total} = m_{SS} - m_{OD} \quad \text{Equation 4.1}$$

The degree of saturation (S) is defined as the percentage of pore volume filled with a liquid phase ( $V_{liquid}$ ) [52]. Some samples were air dried to condition them to varying degrees of saturation. After drying, the samples were weighed ( $m$ ) and the degree of saturation was determined gravimetrically.

$$S = \frac{V_{liquid}}{V_{total}} = \frac{m - m_{OD}}{V_{total}} \quad \text{Equation 4.2}$$

The selected samples were then wrapped in aluminum tape to prevent moisture loss before imaging. The remaining samples were then oven dried before beginning the absorption test. All samples were wrapped in aluminum tape before absorption testing to ensure one-directional absorption.

#### 4.3.2 Neutron Imaging

The imaging was performed at the Neutron Imaging Facility at the National Institute of Standards and Technology in Gaithersburg, MD. The neutron source is a 20 MW heavy-water fission reactor operated at 37 °C. The neutron beam used in this study has an aperture diameter of 10 mm, a fluence rate of  $4.97 \times 10^6 \text{ cm}^{-2}\text{s}^{-1}$  and a collimation ratio of 600. The field of view was 25 cm by 20 cm. A LiF:ZnS scintillator, 300  $\mu\text{m}$  thick, and an amorphous silicon detector with a pixel pitch of 127  $\mu\text{m}$  behind the samples converts the neutrons to light and generates an electrical signal which is recorded as a digital image with equipment outside the beam line.

Ten samples were placed directly in front of the detector in an aluminum frame as shown in Figure 4.1. The frame was filled with deionized water to a level of 10 mm from the bottom of the frame. In order to image all the samples, the frame was attached to a translating table that moved to three positions. Images were captured at 1 frame per second for 30 s. At each location, 10 averaged images were recorded. Due to the motor movement, 4 min elapsed between sets of images at each location. The samples were imaged continuously, with the exception of when water was added, for 12 h.

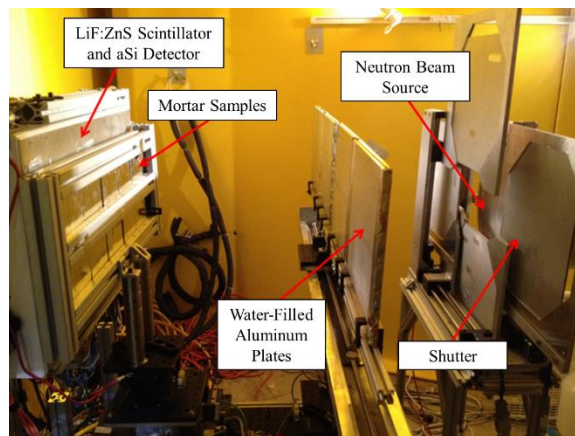


Figure 4.1. Experimental set up for neutron radiography at the Neutron Imaging Facility at NIST.

Calibration images of the individual materials were taken to calculate an attenuation coefficient for water, fine aggregate, and unhydrated cement. Aluminum plates of known thickness and spacing were imaged empty and then filled with the different materials and reimaged. The calibration set up is also pictured in Figure 4.1.

### 4.3.3 Image Processing and Analysis

To eliminate outliers, images were combined with a median filter in groups of 3 for the series of images during water absorption. Reference images of samples prior to exposure to water were combined in groups of 10. Thirty flat field (open beam) and dark (closed beam) images were also taken and combined with a median filter. The use of a median filter in time eliminated the appearance of streaks due to gamma rays and fast neutrons depositing energy.

After combining images, they were deconvolved using the Fast Fourier Transform (FFT). The measured image was the true image convoluted with the point spread function (PSF) plus noise [23], [56]. By deconvolving the images, they are transformed back to the spatial domain from the frequency domain.

The attenuation coefficients of the three raw materials ( $\mu_i$ ) were determined with Equation 4.3. The thickness of the fine aggregate and unhydrated cement powder were corrected by their estimated packing densities, based on the specific gravity of each material.

$$\mu_i = \frac{-\ln(I/I_0)}{t} \quad \text{Equation 4.3}$$

where  $I/I_0$  is the ratio of the background-corrected intensity of the sample in the state of interest to the background-corrected intensity of the empty aluminum containers and  $t$  is the material thickness.

## 4.4 Results

### 4.4.1 Expansion of Beer's Law

Assuming the average volume of each constituent of the mortar is constant throughout the cross section of the sample, Beer's Law can be expanded to be the sum of the volumes of constituents multiplied by their respective attenuation coefficients [50]. Equation 4.4 is the linear relationship between the total composite attenuation coefficient of mortar and the degree of saturation. The total porosity is the sum of the gel water ( $V_{gw}$ ), capillary water ( $V_{cw}$ ), entrapped and entrained air ( $V_{air}$ ) and the volume of empty space (created in a sealed specimen) due to chemical shrinkage ( $V_{cs}$ )

$$\mu_{\text{mortar}} = \frac{-\ln(I/I_0)}{t_{\text{mortar}}} = \mu_a V_a + \mu_c V_c + \mu_{gs} V_{gs} + \mu_w (V_{gw} + V_{cw} + V_{cs} + V_{air}) \cdot S$$

Equation 4.4

The volume of each constituent of the paste (unhydrated cement ( $V_c$ ), gel solids ( $V_{gs}$ ), gel water, capillary water, and chemical shrinkage) can be estimated from Powers model based on the degree of hydration of the paste [15], [51] as shown graphically in Figure 4.2. The volume of aggregate ( $V_a$ ) is known from the given mixture proportions.

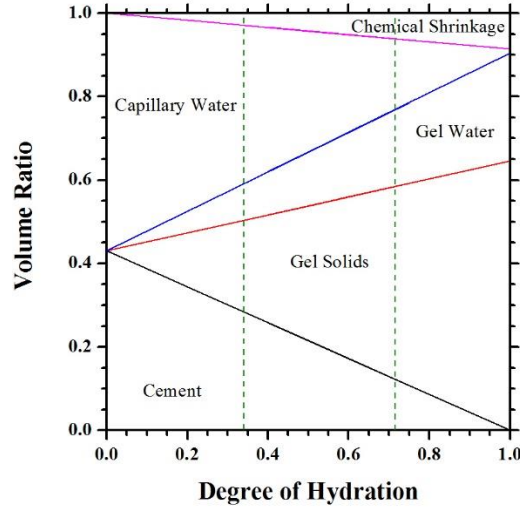


Figure 4.2. Volumetric proportions of constituents of hydrated cement paste with respect to the degree of hydration.

The attenuation coefficient ( $\mu$ ) is the equivalent to the total macroscopic scattering cross section that is the product of the material density number and the total scattering cross section. The attenuation coefficients of water, sand, aluminum, and unhydrated cement powder were determined directly from the optical density of the radiographs using Equation 4.3. The measured value of the gel solids was back calculated and averaged over 10 oven-dried ( $S=0$ ) specimens. The total composite attenuation coefficient was known, as well as the volume of each phase, so  $\mu_{gs}$  was solved for using Equation 4.5.

$$\mu_{gs} = \frac{1}{V_{gs}} \left[ \frac{-\ln(I/I_0)}{t_{mortar}} - \mu_a V_a - \mu_c V_c \right] \quad \text{Equation 4.5}$$

The attenuation coefficient was also calculated based on the chemical composition of the materials using Equation 4.6 [9]. The chemical composition of the unhydrated cement was given in the mill certificate from the cement manufacturer. The gel solids are assumed to be comprised of calcium silicate hydrate ( $C_3S_2H_3$ ) and calcium hydroxide (CH) that are

products from the hydrolysis of  $C_3S$  and  $C_2S$ . Other reaction products such as ettringite are not considered in this computation, since  $C_3S_2H_3$  and  $CH$  comprise the majority of gel solids for a typical Portland cement [53].

$$\mu_i = \frac{\sigma_T \cdot \rho \cdot N_A}{m} \quad \text{Equation 4.6}$$

where  $\sigma_T$  is the total microscopic cross section,  $\rho$  is the density,  $N_A$  is Avogadro's number and  $m$  is the molecular weight.

The differences between the calculated and measured values can be attributed to the fact that Equation 4.6 does not account for inelastic scattering and absorption effects, which is especially seen in the case of water [57], [58]. The difference in the values can also be due to inaccuracies in the estimation of the chemical composition of the materials.

Table 4.2. Calculated and measured values of  $\mu_i$  for use in Equation 4.4.

Material	Calculated $\mu$ ( $mm^{-1}$ )	Measured $\mu$ ( $mm^{-1}$ )
Aluminum ( $\mu_{Al}$ )	0.0104	$0.0095 \pm 0.0022$
Water ( $\mu_w$ )	0.5648	$0.3808 \pm 0.0036$
Fine Aggregate ( $\mu_a$ )	0.0287	$0.0339 \pm 0.0002$
Cement ( $\mu_c$ )	0.0385	$0.0369 \pm 0.0005$
Gel Solids ( $\mu_{gs}$ )	0.2394	$0.2675 \pm 0.0266$

#### 4.4.2 Degree of Saturation

##### 4.4.2.1 Predicted Values of $S$ Based on Composite Attenuation Coefficient

The attenuation coefficient of a particular mortar sample with the same degree of hydration and volume fraction of aggregates, increases linearly as the degree of saturation increases,

under the assumption that the effective thickness of water in the sample is small enough that there are no non-linear effects of beam hardening [22]. The samples used in this study were 10 mm thick with a maximum porosity of 24 % so it was assumed that the effective thickness of water when the pores were completely filled was at most 2.4 mm, which is within the linear range.

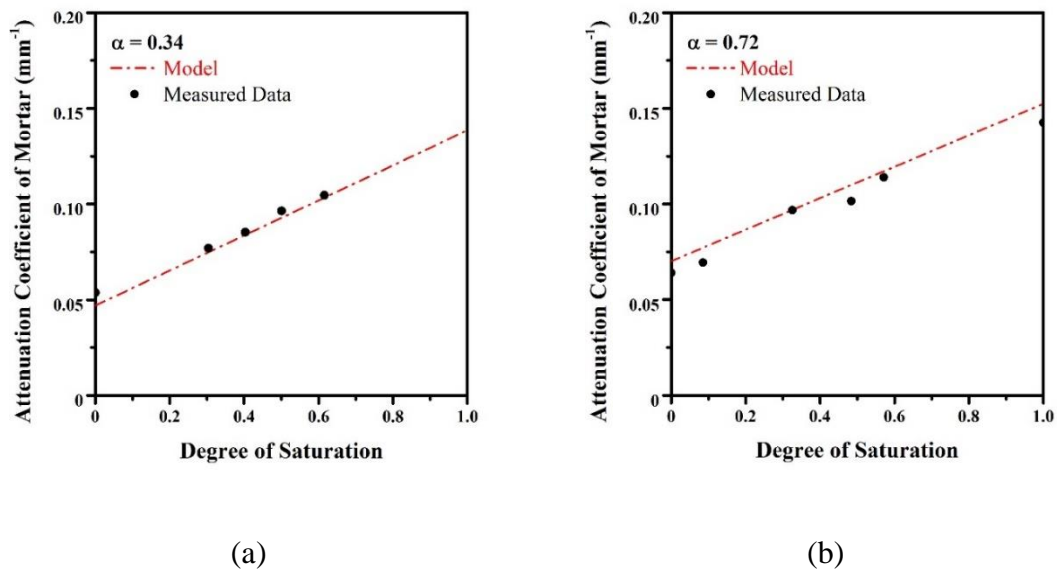


Figure 4.3. The influence of the degree of saturation on  $\mu_{mortar}$  for a (a) low degree of hydration (35 %) and a (b) high degree of hydration (72 %)

The measured data in Figure 4.3 was preconditioned as described in Section 4.3.1. The degree of saturation was determined gravimetrically. The samples were imaged and the background-corrected intensity at the center of the sample was used in Equation 4.3 to determine  $\mu_{mortar}$ . Multiple samples were imaged at  $S=0$  and the coefficient of variation (COV) of  $\mu_{mortar}$  was 4.6% for mortar with a low degree of hydration and 6.2% for mortar with a high degree of hydration. Multiple samples were also imaged at  $S=1$  and the COV

for  $\mu_{mortar}$  was 6.8% for a mortar at a high degree of hydration. The linear model, Equation 4.4, was solved at each respective degree of hydration.

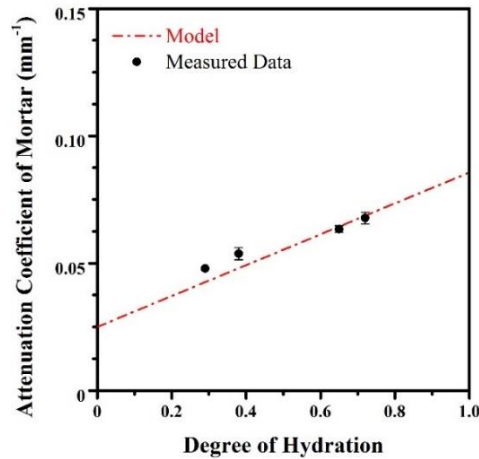


Figure 4.4. Influence of degree of hydration on  $\mu_{mortar}$  with  $S$  of 0,  $w/c$  of 0.42, and  $V_a$  of 0.55.

The model can also estimate the degree of hydration given the total composite attenuation coefficient. The measured data are oven dried samples of Mixture 0.42-nAE that were allowed to cure for varying times. The increase in attenuation coefficient is due to the production of hydration products which include hydrogen-rich calcium silicate hydrate.

#### 4.4.2.2 Degree of Saturation in Mortars Absorbing Water from One Edge

The absorption behavior of non air entrained and air entrained mortar when exposed to water was investigated over 12 h. The bottom surface was exposed to water and the moisture front was monitored. The average degree of saturation was evaluated along the center of the sample in the direction of the yellow arrow in Figure 4.5. The first 5 mm of



mortar were omitted from the analysis due to excess water trapped between the aluminum frame and sample.

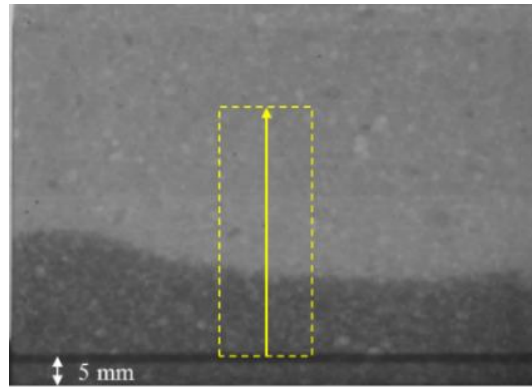


Figure 4.5. Area of analysis of a typical mortar sample exposed to water on the bottom surface.

It is expected that the small pores in the cement paste (gel and capillary pores, as well as voids due to chemical shrinkage) will fill quickly as the moisture front progresses up into the mortar, but the large entrapped and entrained air voids will remain empty [1], [59] and only begin to fill slowly later in time. In Figure 4.6 and Figure 4.7,  $S_{matrix}$  represents the degree of saturation of the mortar when the pores of the cement matrix are filled (gel and capillary pores).

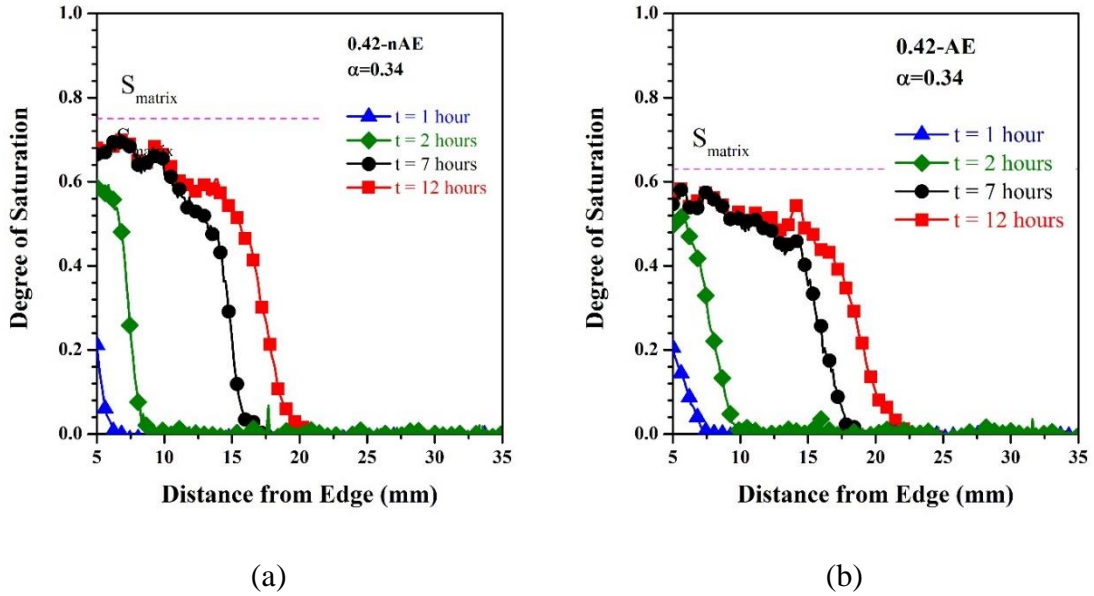


Figure 4.6. Moisture profiles for mortar with a low degree of hydration (a) without air entrainment and (b) with air entrainment.

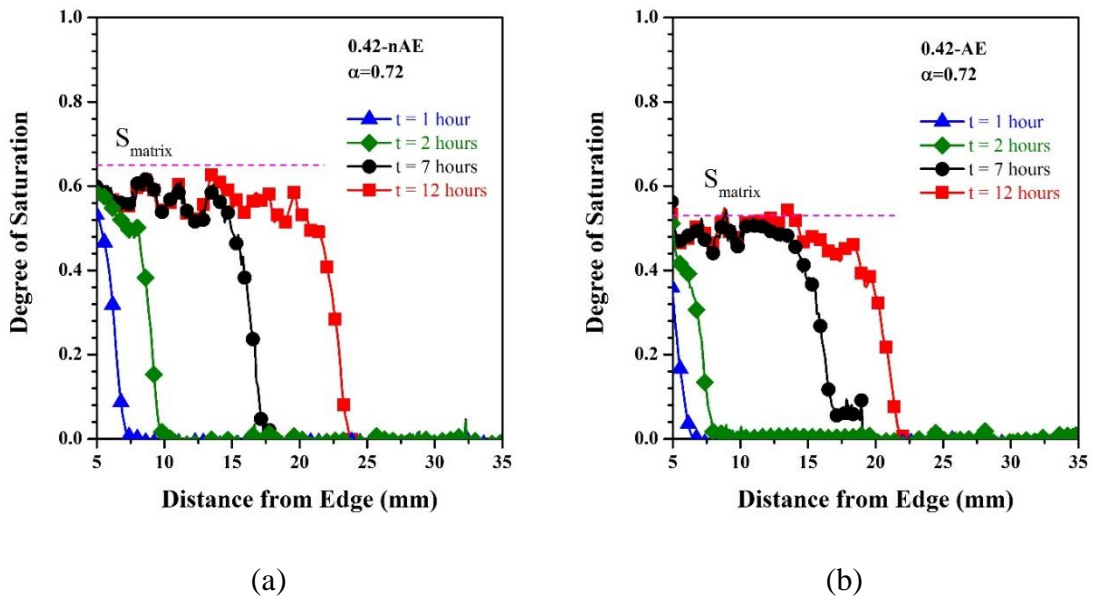


Figure 4.7. Moisture profiles for mortar with a high degree of hydration (a) without air entrainment and (b) with air entrainment.

None of the samples reached a degree of saturation greater than  $S_{matrix}$  regardless of degree of hydration or air content. This further confirms that the air voids are not filling with

water. As expected, the addition of air entrainment lowers the degree of saturation within the mortar compared to a non air entrained specimen exposed to water for the same duration. According to the Young-Laplace equation, the capillary stresses generated are inversely proportional to the pore radius. Therefore it is expected that the small pores fill quickly, whereas the large voids do not generate enough pressure to cause fluid to enter during the initial exposure to water. Standard tests for assessing the absorption rate in concrete such as ASTM C1585-13 [5] monitor mass gain in specimen exposed on one edge with respect to the square root of time. The results are typically linear for the first few hours then non-linear as it transitions to a second linear portion with a much smaller slope than the first. The transition region, or nick-point is due to the shift in the controlling pore size [60]. From the analysis of the neutron radiographs, it can be seen that the initial sorptivity is controlled solely by the volume of small gel and capillary pores.

#### 4.5 Conclusions

The degree of saturation in a mortar sample can be determined using neutron radiography using multiple methods. By expanding Beer's Law and having knowledge of mortar mixture proportions and degree of hydration, the percent of water in the pores can be estimated. This can be advantageous because samples can be pre-conditioned in the lab or samples of an unknown moisture content can be imaged and  $S$  can be determined without a dry reference. It should be noted that this model is only for mortar where the composition of the cross section is assumed to be relatively constant. This technique cannot be applied to concrete where large aggregate occupies the bulk of the cross section.

The results of the one-directional absorption tests revealed information about the absorption behavior of mortar, leading to insights on how to interpret standard absorption procedures such as ASTM C1585-13. Notably, the initial sorptivity represents only the filling of the small matrix pores. This implies that the secondary sorptivity (which is a much slower rate than the initial) is dependent on the amount and the connectivity and/or pressure associated with the air void system. From a practical standpoint, the addition of air entrainment lowers the degree of saturation through the moisture front and can be used to keep concrete below the critical degree of saturation, thus preventing freeze thaw damage.

## CHAPTER 5. USING NEUTRON RADIOGRAPHY TO MEASURE THE ABSORPTION OF CALCIUM CHLORIDE SOLUTION IN MORTAR

### 5.1 Abstract

A portion of the concrete pavements in the US have recently been observed to have premature joint deterioration. While this damage has been attributed to a wide variety of potential factors, it is hypothesized that one component of this damage can be attributed to a reaction that occurs when salt-laden water is absorbed in the concrete and reacts with the matrix. This study examines the absorption of  $\text{CaCl}_2$  solution in mortar. Due to its high spatial and temporal resolution, neutron imaging was used in this investigation to measure fluid movement. Neutrons interact with the nuclei of atoms and are therefore sensitive to light atoms such as hydrogen. This makes neutron imaging ideal for measuring changes in fluid content of a porous media. The change in the moisture content was determined along the length of the specimen during absorption.

Mortar specimens were prepared with water to cement ratios, ( $w/c$ ), of 0.36, 0.42 and 0.50 by mass. The mortar specimens were conditioned to 50 % relative humidity before being exposed to chloride solutions with concentrations ranging from 0 to 29.8 % by mass. The depth of fluid penetration was monitored continuously for approximately 12 h as the fluid penetrated and subsequently at 24 h, 48 h, and 96 h. At low concentrations of  $\text{CaCl}_2$  (10% by mass) the sorptivity ( $\text{mm/s}^{1/2}$ ) decreased by 38 %, 20 %, and 26 % in mortars with a

w/c of 0.36, 0.42 and 0.50, respectively. At high concentrations (29.8 %), the sorptivity decreased 83 %, 87 %, and 87 % in the same mortars. First, it is known that changes in the surface tension and viscosity will reduce the rate of absorption. The decrease in absorption at low concentrations can be attributed to these changes in fluid properties. Second, a reaction can occur between  $\text{CaCl}_2$  and cement paste creating products that block the pores and reduce absorption at higher concentrations.

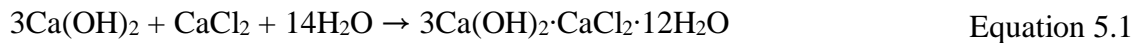
## 5.2 Introduction

Concrete pavements represent a large portion of the transportation infrastructure. While many of these pavements provide excellent long-term performance, some pavements, particularly in the northern region of the US, have recently exhibited premature joint deterioration. This damage can shorten the life of an otherwise well-functioning pavement or can necessitate costly repairs. Recently, studies have been conducted to examine causes [61], [62], early detection [63], [64], and mitigation of joint deterioration [65], [66].

Other research has focused on the development of approaches to predict how long freeze-thaw damage will take to occur. These models use fluid absorption to aid in the determination of the degree of saturation [67]. The degree of saturation influences the freeze-thaw performance of concrete [1], [2], [68]. The addition of salts to the pore fluid can increase the degree of saturation due to the higher equilibrium relative humidity of the solution [69], [70]. The addition of salts will alter properties of the fluid such as surface tension and viscosity, therefore altering the transport properties such as absorption. The fluid viscosity and surface tension both increase with an increase in concentration of salts

[69], which will decrease the rate of absorption [70]. Furthermore, salt can also precipitate out of solution and block pores, preventing further fluid ingress and locally increasing the degree of saturation [71].

In many cold climates, salt solutions are used on concrete roads and sidewalks to lower the freezing temperature of the solution to minimize the formation of ice. However, calcium chloride can react with the calcium aluminate phases ( $C_3A$ ) of cement or monosulphate (Afm) to create Friedel's salt [72], [73]. The calcium sulfo-aluminate phases (Afm and Aft) can further react with chloride-based salts to form Kuzel's salt [74]. Additionally, calcium chloride can interact with calcium hydroxide to form calcium oxychloride at room temperature (Equation 5.1). All three products can form in the voids, reducing fluid ingress, as well as reducing the volume of empty pores which increases the degree of saturation [71].



A standardized test method for quantifying absorption of water in concrete is ASTM C1585 [5]. This test is developed for water and does not provide corrections for fluids with viscosities and surface tensions that differ from those of deionized water. Additionally, the absorption behavior is influenced by the initial conditioning [36]. According to the standard, the absorption,  $I$  ( $mm^3/mm^2$ ), can be computed as shown in Equation 5.2:

$$I = \frac{m_t}{a \cdot \rho} \quad \text{Equation 5.2}$$

where  $m_t$  is the change in specimen mass at the time  $t$  after exposure to the fluid (g),  $a$  is the exposed area of the specimen ( $mm^2$ ) and  $\rho$  is the density of water ( $g/mm^3$ ). Additionally,

ASTM C1585 instructs users to plot the results of the test as  $\text{mm}^3$  of water absorbed normalized by the surface area of the specimen in  $\text{mm}^2$  versus the square root of time. This calculation provides a result in units of mm which many mistakenly interpret as the depth of water ingress. However, the test does not account for total pore volume which can affect the interpretation of the results.

The initial rate of absorption, or sorptivity as defined by ASTM C1585,  $S_i$  ( $\text{mm}/\text{s}^{1/2}$ ) is the slope of the absorption versus the square root of time up to 6 h. The secondary sorptivity,  $S_s$  ( $\text{mm}/\text{s}^{1/2}$ ) is the slope of the absorption versus the square root of time between 1 d and 7 d. However it should be noted that these times are dependent on the sample height and fluid properties [4], [17], [70].

While Equation 5.2 is used for absorption and the ASTM method for determining  $S_i$  and  $S_s$  are useful for qualifying the absorption behavior of concrete, it is not representative of the actual depth of penetration into the specimen. The rate at which the fluid travels is dependent on the fluid properties (such as surface tension, viscosity and density) and the volume of pores as well as the connectivity of the pores in the paste [13], [17], [19], [50]. To overcome this shortcoming, some have used the intrinsic absorption as defined in Equation 5.3 [4].

$$I_{\text{int}} = \frac{m_t}{a \cdot \rho \cdot \Phi \cdot (1 - D_0)} \cdot \sqrt{\frac{\gamma_w \eta_s}{\gamma_s \eta_w}} \quad \text{Equation 5.3}$$

where  $I_{\text{int}}$  (mm) is the intrinsic absorption,  $\Phi$  is the volume fraction of porosity,  $D_0$  is the volume fraction of the initial degree of saturation,  $\eta_w$  and  $\eta_s$  are the viscosities of water and



solution (Pa·s), respectively; and  $\gamma_w$  and  $\gamma_s$  are the surface tensions of water and solution (N/mm), respectively.

Neutron imaging is an accurate and powerful method of monitoring fluid penetration in porous media and has been used by many researchers [21], [25], [26], [43], [75]. This nondestructive test method can be used to monitor the actual depth of fluid penetration continuously for long periods of time. The volume of water in the system can be accurately quantified in addition to the ability to visually monitor fluid movement in situ [22], [28], [44]. This allows for the calculation of the degree of saturation in the system which is directly related to long term performance, particularly in freeze-thaw cycles.

### 5.3 Experimental

#### 5.3.1 Sample Preparation

Mortar specimen were mixed in accordance with ASTM C192/C192M-13 [48] using the mixture proportions in Table 5.1. Both ASTM C150 Type I and Type V cements were used in this study. The composition of each cement is listed in Table 5.2. It is expected that mortars made using Type V cement will produce less Friedel's and Kuzel's salts when exposed to  $\text{CaCl}_2$  due to the lower amount of aluminates ( $\text{C}_3\text{A}$ ) in the system although they form due to the increased presence of  $\text{C}_4\text{AF}$  [72], [76].

Table 5.1. Mixture proportions for the four mortars used in absorption experiments

Mixture No.	Type I Cement (kg/m <sup>3</sup> )	Type V Cement (kg/m <sup>3</sup> )	Water (kg/m <sup>3</sup> )	Fine Aggregate (SSD) (kg/m <sup>3</sup> )	w/c
1	632.6	--	227.7	1363.1	0.36
2	581.0	--	244.0	1368.3	0.42
3	524.0	--	262.0	1363.1	0.50
4	--	581.0	244.0	1363.1	0.42

Table 5.2. Chemical and physical properties of ordinary Portland cement

Component	Percent by Mass (%)	
	Type I	Type V
SiO <sub>2</sub>	19.3	21.3
Al <sub>2</sub> O <sub>3</sub>	5.2	2.6
Fe <sub>2</sub> O <sub>3</sub>	2.9	4.2
CaO	64.0	63.2
MgO	2.6	4.5
SO <sub>3</sub>	3.3	2.8
C <sub>3</sub> S	63.4	64.0
C <sub>2</sub> S	8.4	13.1
C <sub>3</sub> A	9.0	0.0
C <sub>4</sub> AF	8.7	12.8
Blaine Fineness (cm <sup>2</sup> /g)	3680	3160

The mortar was cast in 75 mm by 100 mm by 400 mm prisms. After setting, the mortar prisms were removed from their molds, sealed, and kept at 23 °C ± 1 °C until they reached 60 % hydration. The curing time to reach the desired degree of hydration was computed using isothermal calorimetry [77]. The time to reach 60 % hydration was 27 d, 78 h, 55 h, and 21 d for mixtures 1 through 4, respectively. The mortar prism was cut with a wet saw to 75 mm wide by 50 mm high by 20 mm ± 1.2 mm thick slices. The cut specimen were then placed in a chamber at 23 °C and 50 % relative humidity (RH) for 1 month. Equilibrium was determined when the change in mass was less than 0.02 % for a 15 d

period [36]. Specimens were then wrapped in aluminum tape to prevent moisture loss. The top and bottom surfaces were subsequently exposed for absorption tests.

Additional samples of each mixture were oven dried and vacuum saturated to 100 % degree of saturation. A group of additional mortar specimens with a  $w/c$  of 0.42 and Type I OPC were conditioned differently in order to compare the degree of saturation as determined from neutron images and by mass. Samples were conditioned to degrees of saturation between 30 % and 90 % by saturating samples and letting them dry in air for various amounts of time. Once dried to the desired moisture content by mass, the sample was rewrapped in aluminum tape and allowed to re-equilibrate for at least 24 h.

Calcium chloride solutions were prepared as percent of  $\text{CaCl}_2$  to water by mass. Solutions ranging from 0 % (deionized water) to 29.8 %, the eutectic concentration of calcium chloride and water, were used for this study in order to include the spectrum of concentrations that may be seen in pavements in the field. The fluid properties of each solution are summarized in Table 5.3 [70], [78], [79]. The viscosity of the solution increases by a factor of 3.3 while the surface tension only increases by a factor of 1.13. The sorptivity of fluid is influenced by the square root of the ratio of the surface tension to the viscosity [13] so the relatively large increase in viscosity will result in an overall decrease in sorptivity.

Table 5.3. Fluid properties for concentrations of CaCl<sub>2</sub> solutions used in this study

CaCl <sub>2</sub> Concentration (% by mass)	Density (kg/m <sup>3</sup> )	Viscosity (mN·s/m <sup>2</sup> )	Surface Tension (mN/m)	Theoretical Normalized Sorptivity
0	997	0.905	72.8	1.00
10	1087	1.045	75.02	0.94
20	1189	1.675	79.47	0.77
29.8	1291	2.975	85.88	0.60

### 5.3.2 Neutron Imaging

Imaging was performed at the Neutron Imaging Facility at the National Institute of Standards and Technology in Gaithersburg, Maryland. The imaging facility is located at Beam Tube 2 as shown in Figure 5.1. The thermal neutron source is a 20 MW heavy-water fission reactor operated at 37 °C. A collimation ratio (L/D) of 450 and a neutron fluence rate of  $1.4 \times 10^7 \text{ cm}^{-2}\text{s}^{-1}$  were used for the sorption experiments. A scientific complimentary oxide semiconductor (sCMOS) camera viewed a Gadolinium oxysulfide scintillator through a Nikon 85 mm f/1.8 lens with a PK-11a extension tube to create a neutron detector with an effective pixel pitch of 30  $\mu\text{m}$ .

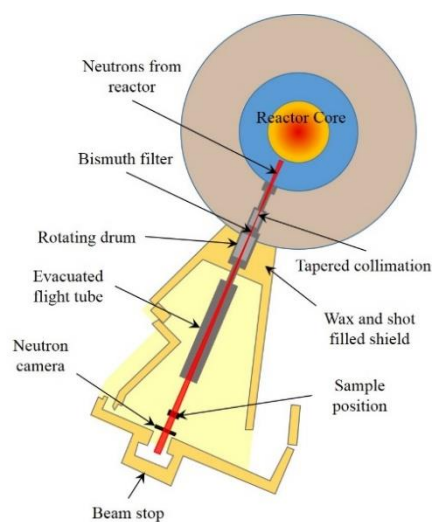


Figure 5.1. Plan view of the Neutron Imaging Facility at NIST

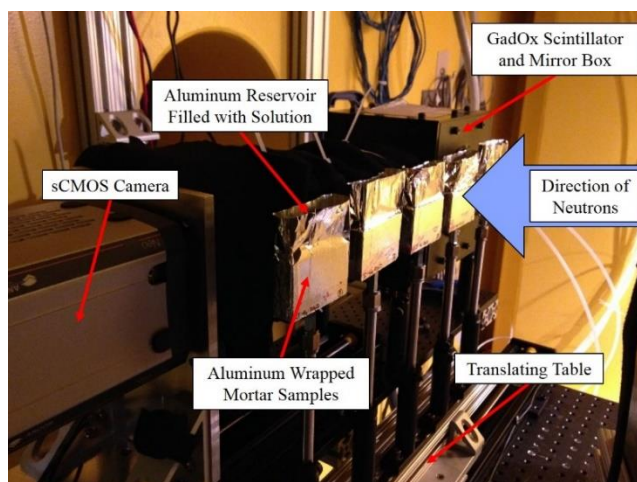


Figure 5.2. Experimental set up for chloride ponding tests.

The experiment was set up such that five samples could be imaged in each test series. The samples were placed on a motorized table so that they could be repositioned in the beam line without the beam being turned off, as shown in Figure 5.2. Nine images of each sample were taken with an exposure time of 60 s to serve as reference images of the specimen at 50 % RH before being exposed to the chloride solutions. Nine images of similar samples cut from the same prism in the oven dried and fully saturated conditions were also taken to determine the degree of saturation during absorption.

After the reference images were captured, fluid ingress could be measured. The ponding reservoirs on top of the samples were filled with approximately 30 mL of solution and the mortar began absorbing the fluid. Three images were captured of each sample before the stage moved to the next position to image the next sample. As a result of the table movement, approximately 30 min elapsed between each set of images per specimen.

### 5.3.3 Image Processing and Analysis

Images were combined with a median filter in groups of 9 for the reference images or 3 for images taken during absorption. 30 flat field (open beam) and dark (closed beam) images were also taken and combined with a median filter. The use of a median filter (in time) eliminated the appearance of streaks due to gamma rays and fast neutrons depositing energy directly into the sCMOS.

The images of the mortar in the wet state at time  $t$  after exposure to fluid were normalized to the reference image before exposure to fluid and converted to binary form as shown in Figure 5.3a and b. The depth of penetration was measured at 10 points, equally spaced at 5 mm according to Figure 5.3c, along the water front as shown in Figure 5.3d.

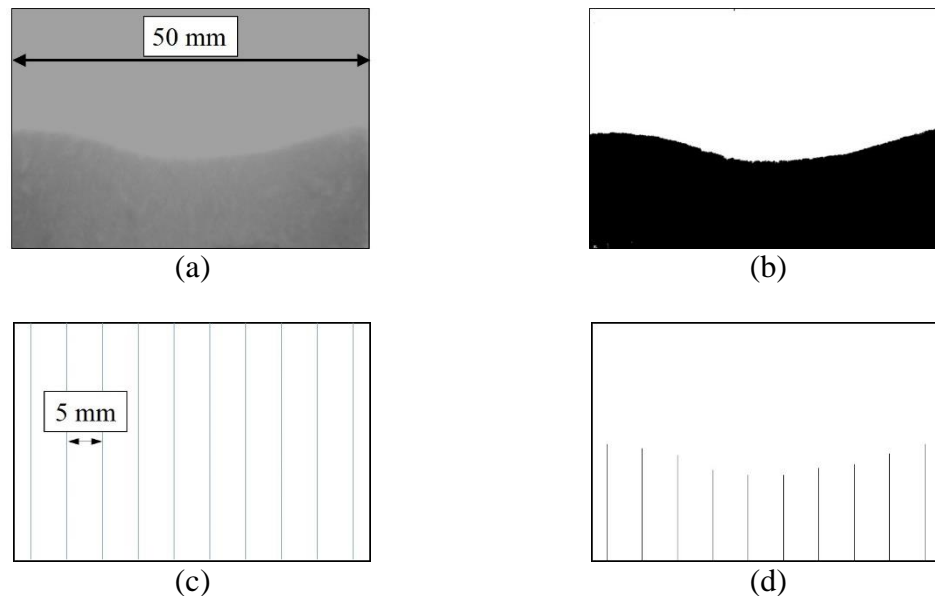


Figure 5.3. Image analysis procedure for determining the average depth of penetration.

(a) Background-normalized images were (b) converted to binary. (c) A mask of vertical lines was subtracted from the binary images to result in (d) 10 measurable lines of the fluid front.

Beam hardening effects can be seen in neutron images containing relatively large quantities (thicknesses) of water and the water thickness can be determined with Equation 5.5 [22]. These effects can make quantifying water difficult. However, with water thicknesses less than approximately 5 mm, the relationship between optical density and water thickness is linear [6], [22]. The optical density is defined as

$$OD = -\ln\left(\frac{I}{I_0}\right) \quad \text{Equation 5.4}$$

where  $OD$  is the optical density,  $I$  is the measured intensity and  $I_0$  is the intensity of the flat field.

Figure 5.4a illustrates a calculation of optical density as a function of pore volume in mortar for different sample thicknesses. The approximate volume fraction of the pores at 60 % degree of hydration was determined using Powers Model and is summarized in Table 5.4 [15], [51]. The theoretical porosity for 0.36, 0.42, and 0.50  $w/c$  mortars ranged from approximately 19 % to 24 % and is indicated in the gray shaded region of Figure 5.4a. The volume fraction was then applied to various thicknesses of mortar to determine the extent of beam hardening that can be expected.

$$OD(t_w) = \mu_w t_w + \beta_w t_w^2 \quad \text{Equation 5.5}$$

where  $t_w$  is the thickness of water,  $\mu_w$  is  $0.38483 \text{ mm}^{-1}$ , and  $\beta_w$  is  $-0.00947 \text{ mm}^{-2}$ . When using a 20 mm mortar sample as in the case of this study, beam hardening will not be significant as  $t_w \leq 4.8 \text{ mm}$ . This indicates that the relationship between the optical density and the water content can be assumed to be linear between oven dried mortar and 100 % saturated mortar.

Table 5.4. Calculated components of porosity according to Powers model

	Mixture No.			
	1	2	3	4
Capillary Porosity	0.071	0.097	0.128	0.099
Gel Porosity	0.073	0.065	0.058	0.066
Chemical Shrinkage	0.024	0.022	0.019	0.022
Measured Air	0.020	0.035	0.040	0.026
Total Calculated Porosity	18.8%	21.8%	24.4%	21.3%

The optical density can be normalized by the sample thickness to define the composite attenuation coefficient of the mortar ( $\mu_{mortar}$ ) [6]. By normalizing to the thickness of the sample ( $t_{sample}$ ), the optical density from multiple mortar samples can be compared to each other.

$$\mu_{mortar} = \frac{OD_{mortar}}{t_{sample}} \quad \text{Equation 5.6}$$

The degree of saturation in the mortar is calculated from the radiographs using the optical density normalized to the sample thickness of an oven dried sample ( $S=0$ ) and a completely saturated sample ( $S=1$ ) as calculated in Equation 5.7.

$$S = \frac{\mu_{mortar} - \mu_{DRY}}{\mu_{SAT} - \mu_{DRY}} \times 100\% \quad \text{Equation 5.7}$$

where  $\mu_{DRY}$  and  $\mu_{SAT}$  are the attenuation coefficients of the mortar in the oven dried and saturated states, respectively.



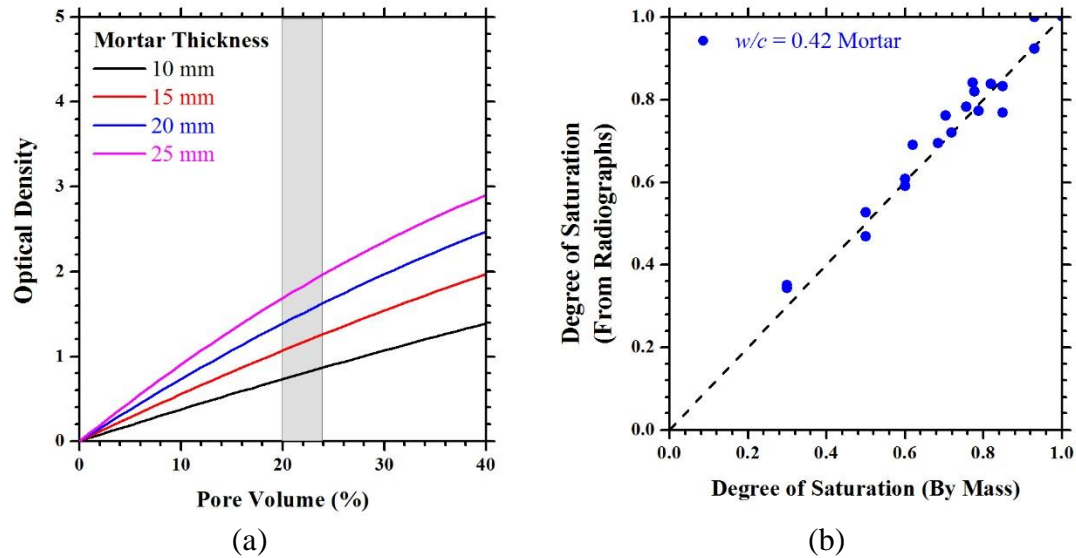


Figure 5.4. (a) Influence of mortar thickness on optical density. The shaded region is the total porosity of the four mortar samples used. (b) Relationship between the degrees of saturation as determined by neutron radiographs and by mass.

Figure 5.4b is a plot of degrees of saturation ( $S$ ) obtained via neutron radiographs versus the degree of saturation determined gravimetrically. A correlation exists between the degrees of saturation calculated from the radiographs to the actual degree of saturation determined by mass.

## 5.4 Results and Discussion

### 5.4.1 Depth of Fluid Penetration

The average depth of penetration was measured every 30 min for the first 12 h of exposure to the chloride solution. After 12 h, the depth of penetration was measured at 25 h ( $300 \text{ s}^{1/2}$ ) and 40 h ( $400 \text{ s}^{1/2}$ ). The results from each series (Mixtures 1-4) are plotted in Figure 5.5.

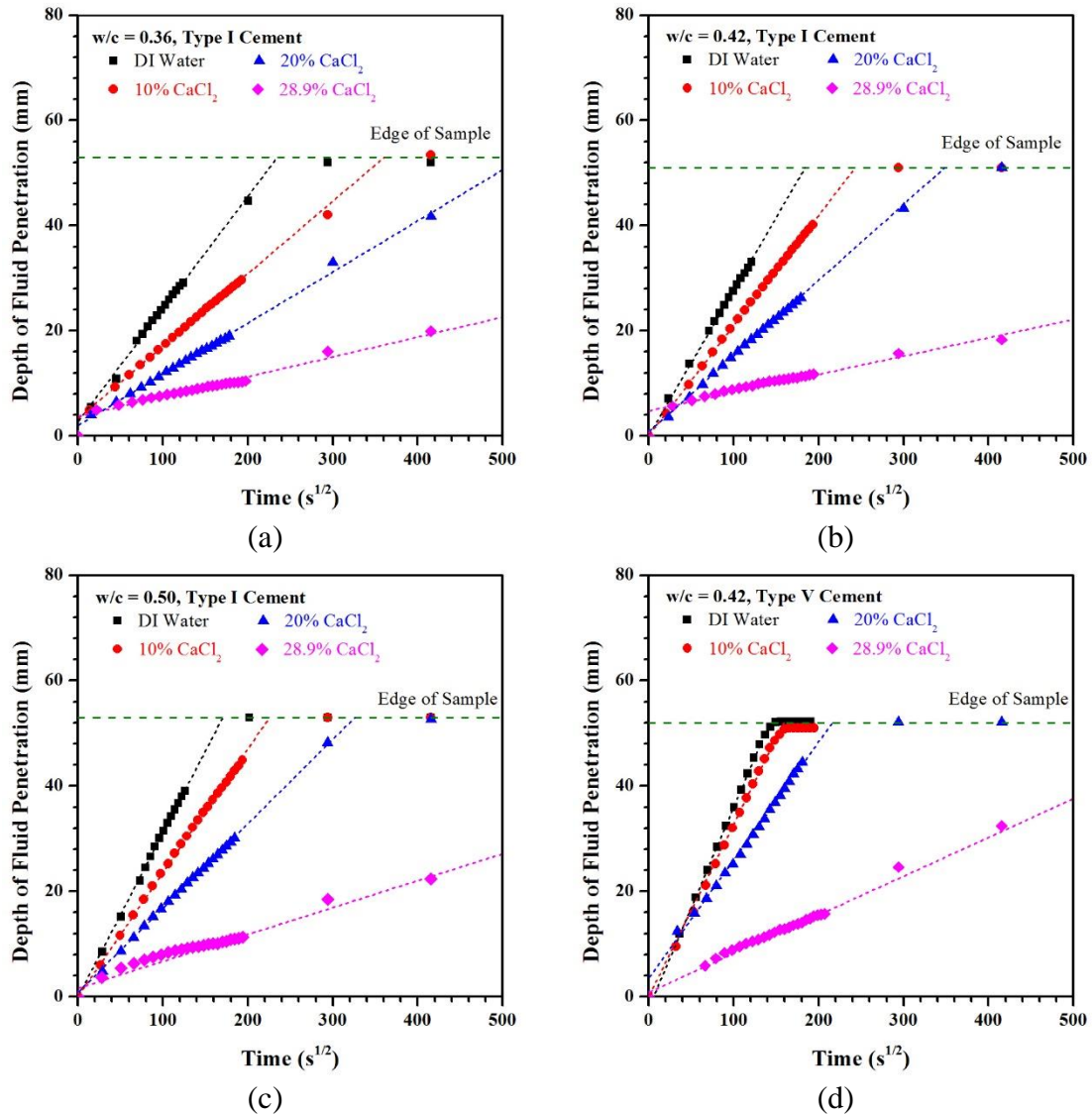


Figure 5.5. Average depth of penetration of four concentrations of  $CaCl_2$  solution for mortars composed of (a)  $w/c$  of 0.36 and Type I cement, (b)  $w/c$  of 0.42 and Type I cement, (c)  $w/c$  of 0.50 and Type I cement, and (d)  $w/c$  of 0.42 and Type V cement.

In general, the rate of fluid penetration decreases as the concentration of chlorides in the solution increases as shown in Figure 5.5. This is consistent with previous studies [4], [70], [71], [80], [81] where the rate of salt solution absorption decreases as the concentration of salts increase. When normalized to the sorptivity of water, there is a clear decrease in sorptivity with an increase in chloride concentration as shown in Figure 5.6. The

theoretical influence of the altered fluid properties (surface tension and viscosity) is plotted as a function of calcium chloride concentration.

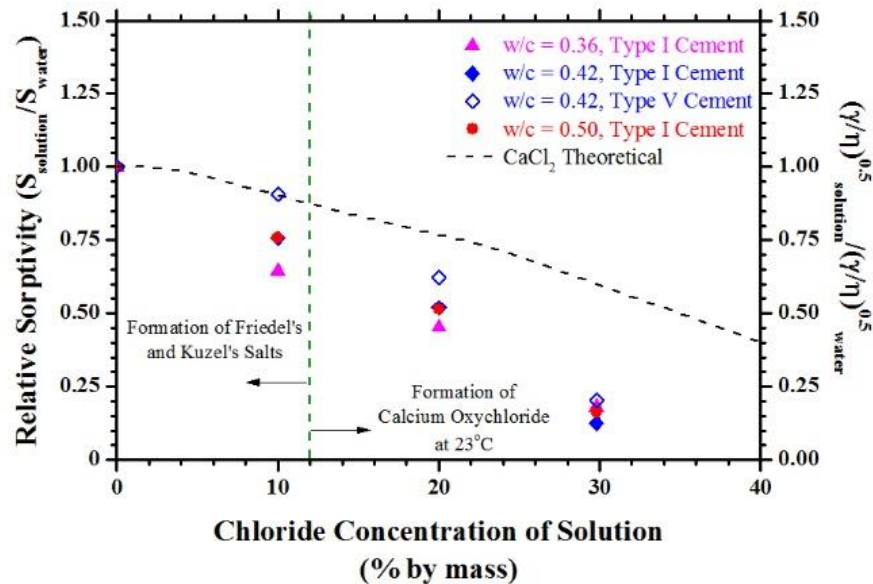


Figure 5.6. Normalized sorptivity with an increase in  $\text{CaCl}_2$  concentration in the ponded fluid. Sorptivity values were normalized to those of DI water for each respective mortar.

When exposed to 10 %  $\text{CaCl}_2$ , mortar prepared with Type V cement remains on the theoretical line, meaning the sorptivity is only influenced by the fluid properties. Mortar prepared with Type I cement also shows a decrease in absorption due to fluid properties when exposed to 10 %  $\text{CaCl}_2$  solution, however the value of normalized sorptivity deviates from the theoretical curve due to a decrease in porosity from the reaction between  $\text{C}_3\text{A}$  and calcium chloride resulting in the formation of Friedel's and Kuzel's salts [4], [72]. At room temperature, calcium oxychloride can form when the  $\text{CaCl}_2$  concentration is over 12 % by mass [3]. When exposed to solutions with 20 % and 29.8 %  $\text{CaCl}_2$ , all samples experienced a decrease in sorptivity beyond that predicted by the change in fluid properties. This

additional decrease in sorptivity is the effect of the formation of calcium oxychloride in addition to the formation of Friedel's and Kuzel's salts in the Type I mortar [4], [62], [82]. Calcium oxychloride and Friedel's salt occupies space in the pores and effectively decreases the pore volume of the matrix hindering the rate of fluid ingress. Table 5.5 summarizes the sorptivity (rate of fluid penetration), the normalized sorptivity and the percent difference between the experimental normalized sorptivity and the theoretical sorptivity.

Table 5.5. Summary of measured sorptivity and normalized sorptivity for mortar samples exposed to  $\text{CaCl}_2$  solutions.

Mixture No.	Sample Description	$\text{CaCl}_2$ Solution (%)	Sorptivity ( $\text{mm/s}^{1/2}$ )	Normalized Sorptivity ( $S_{\text{solution}}/S_{\text{water}}$ )	% Deviation from Theoretical Value
1	w/c = 0.36, Type I	0	0.214	1.00	0.0
		10	0.138	0.64	28.9
		20	0.097	0.45	41.0
		29.8	0.039	0.18	69.7
2	w/c = 0.42, Type I	0	0.277	1.00	0.0
		10	0.210	0.76	16.3
		20	0.144	0.52	32.3
		29.8	0.035	0.13	78.9
3	w/c = 0.50, Type I	0	0.311	1.00	0.0
		10	0.235	0.76	16.2
		20	0.160	0.52	32.9
		29.8	0.051	0.16	72.4
4	w/c = 0.42, Type V	0	0.361	1.00	0.0
		10	0.327	0.91	0.3
		20	0.224	0.62	19.1
		29.8	0.074	0.20	65.8

#### 5.4.2 Change in Degree of Saturation

The degree of saturation was monitored continuously for 12 h and calculated using Equation 5.7. The samples were conditioned to 50 % RH so the initial degree of saturations were approximately 20 %, 16 %, 15 %, and 18 % for Mixtures 1 through 4 respectively. The following figures monitor degree of saturation with respect to the distance from the wetting edge.

Figure 5.7a and b exhibit moisture profiles as expected with a steep gradient at the wetting front that maintains constant shape as time increases [6], [17]. However, in Figure 5.5c and d, there is a clear increase in the change in degree of saturation at the far end of the sample after the water front reaches the edge. All the small pores (gel and capillary pores [15]) quickly fill as the water front advances due to the high capillary pressure in the small pores, and once the water front reaches the edge of the sample, larger pores (entrapped and entrained air) begin to fill slowly as the mortar continues to absorb water.

The increase in salt concentration to 10% does not greatly influence the change in degree of saturation. However, as noted in the previous section, it does decrease the rate of fluid penetration in mortars prepared with Type I cement. The moisture profiles have similar gradients at the wetting front compared to deionized water. Again, in Figure 5.8d, there is an increase in the degree of saturation at the far edge of the sample after the moisture front reached the edge.

With higher chloride concentrations, like 20 % shown in Figure 5.9, the gradient at the fluid front becomes less sharp. In addition, there is a gradient throughout the entire distance of the wetted portion. In the case of deionized water and 10 %  $\text{CaCl}_2$  solution, the moisture content through the wetted portion was generally constant. This could be due to the change in fluid properties with highly concentrated solutions. The viscosity of  $\text{CaCl}_2$  solution doubles when the solution concentration is increased from 10 % to 20 % by mass [69]. It can also be due to the formation of calcium chloroaluminate phases (Friedel's and Kuzel's salts) decreasing the pore volume. When these phases form and fill porosity, the resulting thickness of water measured will decrease.

Finally, at very high concentrations of  $\text{CaCl}_2$ , 29.8 % by mass, it is clear that the penetration of fluid has been greatly hindered in all mortar samples including the one prepared with the Type V cement. In Figure 5.10, there is a two-part moisture front. There is a highly saturated portion near the exposed surface followed by a sharp decrease in moisture content for the remainder of the wetted portion. There may be a build-up of chlorides near the exposed surface that accounts for the peaks seen within the first 5 mm. Chlorine has an attenuation coefficient that is approximately one third that of hydrogen [57], [83] so it could influence the attenuation of neutrons if there are large quantities accumulated. The wetting front gradually declines, which is a much different behavior compared to that of the mortars exposed to lower concentrations of calcium chloride.

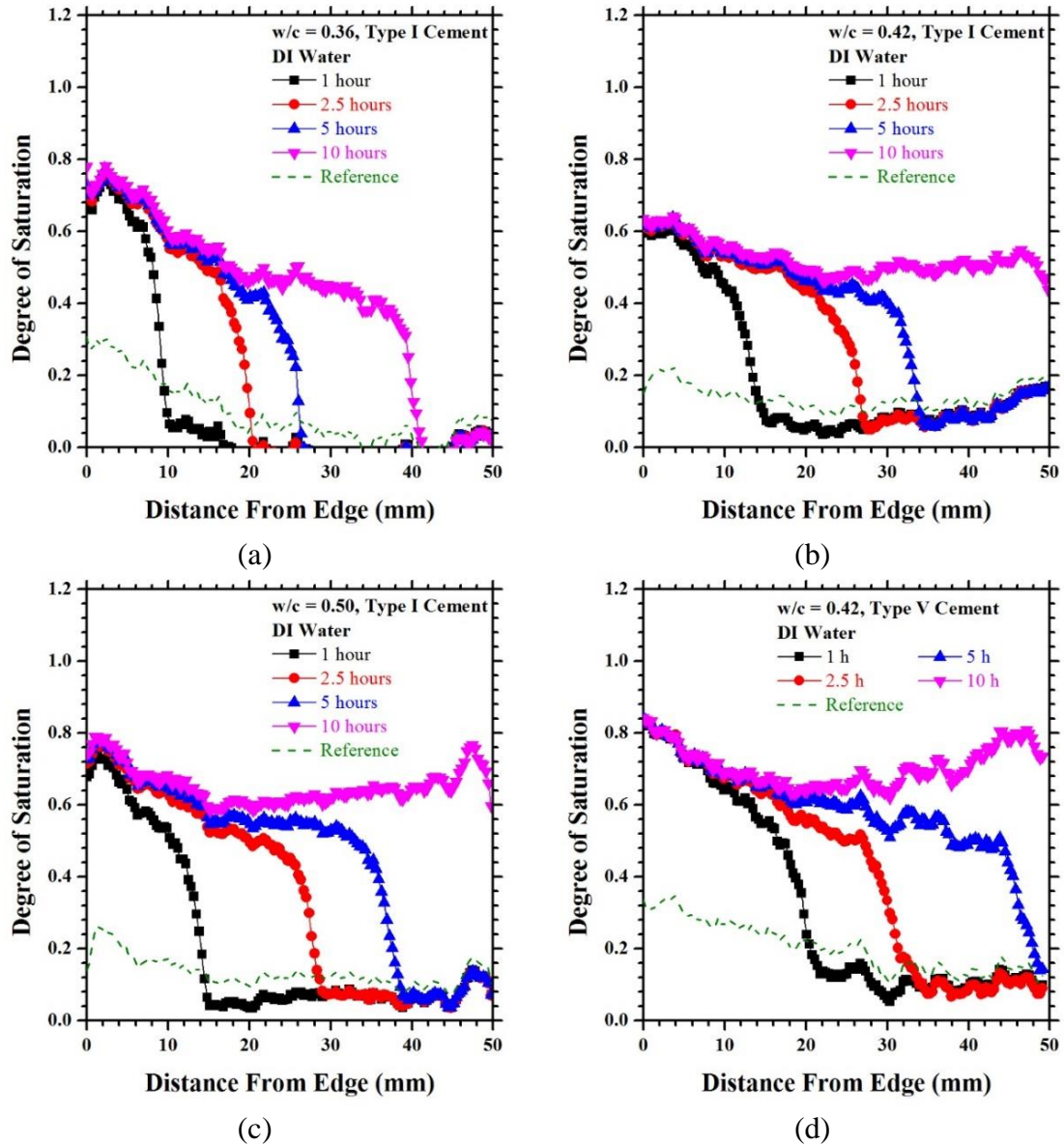


Figure 5.7. Degree of saturation when exposed to deionized water for mortar with (a) w/c of 0.36 with Type I cement, (b) w/c of 0.42 with Type I cement, (c) w/c of 0.50 with Type I cement, and (d) w/c of 0.42 and Type V cement.

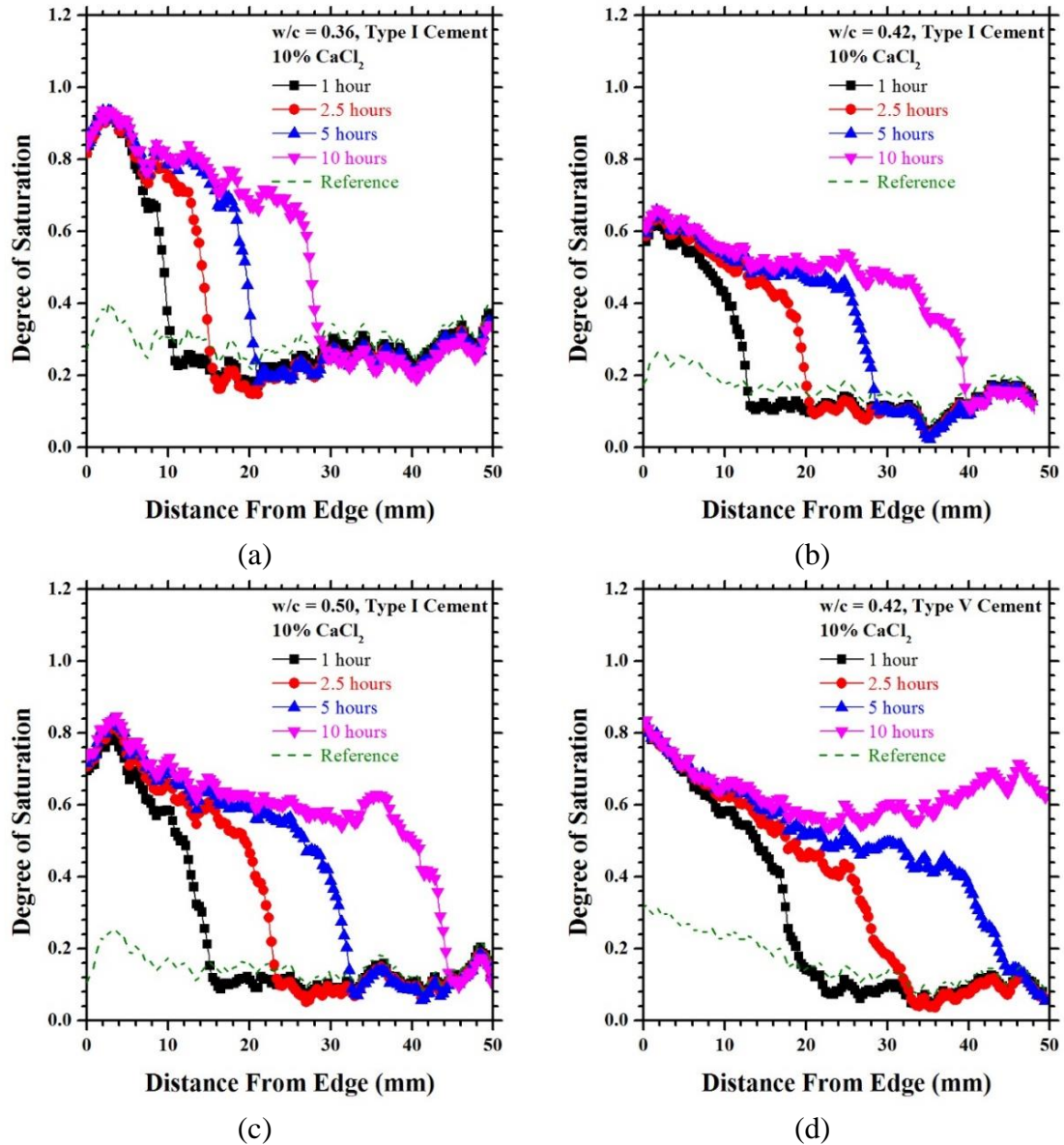


Figure 5.8. Degree of saturation when exposed to 10% CaCl<sub>2</sub> solution for mortar with (a) w/c of 0.36 with Type I cement, (b) w/c of 0.42 with Type I cement, (c) w/c of 0.50 with Type I cement, and (d) w/c of 0.42 and Type V cement.



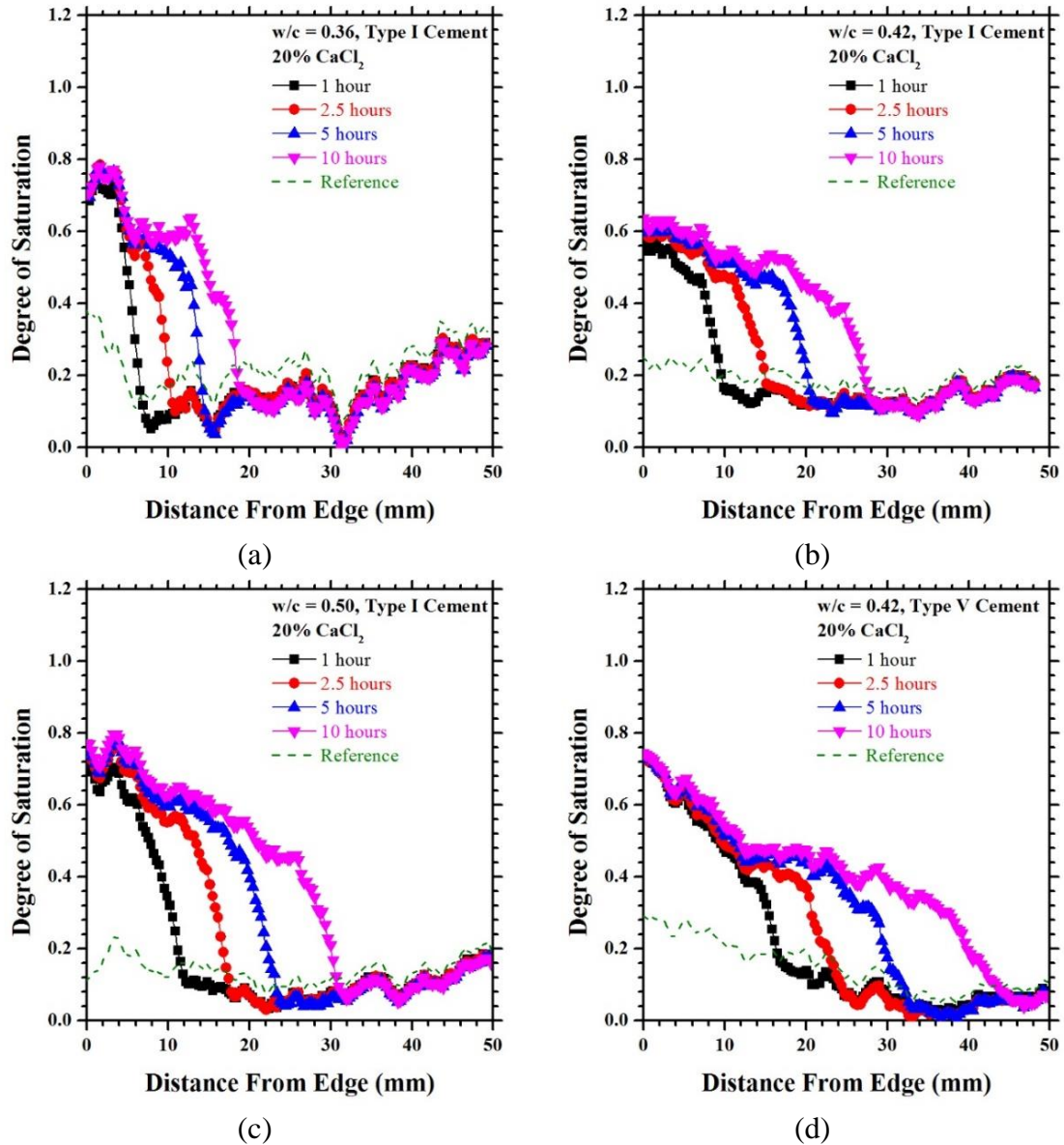


Figure 5.9. Degree of saturation when exposed to 20%  $\text{CaCl}_2$  solution for mortar with (a) w/c of 0.36 with Type I cement, (b) w/c of 0.42 with Type I cement, (c) w/c of 0.50 with Type I cement, and (d) w/c of 0.42 and Type V cement.

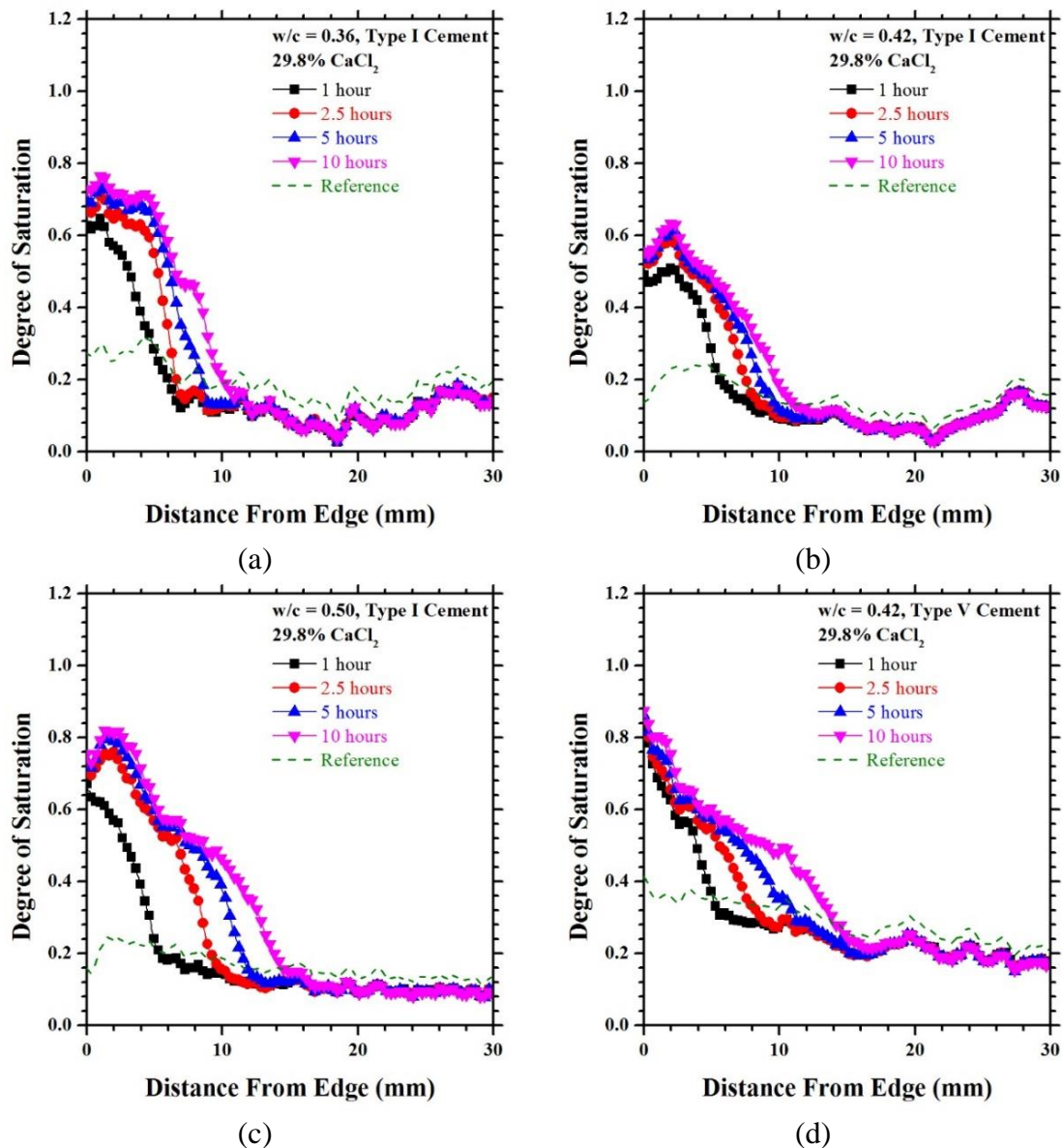


Figure 5.10. Degree of saturation when exposed to 29.8%  $\text{CaCl}_2$  solution for mortar with (a)  $w/c$  of 0.36 with Type I cement, (b)  $w/c$  of 0.42 with Type I cement, (c)  $w/c$  of 0.50 with Type I cement, and (d)  $w/c$  of 0.42 and Type V cement. (Note change in x-axis scaling)

In many of the mortars, the fluid front reached the edge of the sample within 10 h (See Figure 5.7 and Figure 5.8). By 24 h, the deionized water, 10%  $\text{CaCl}_2$ , and 15%  $\text{CaCl}_2$  solutions had completely penetrated the mortar. The mortar continued to absorb fluid after

24 h until monitoring stopped at 96 h. This slow uptake in fluid corresponds to the secondary sorptivity in ASTM C1585. Figure 5.11 shows the continued increase in the degree of saturation after the fluid reached the edge of the sample between 24 h and 96 h. The rate of absorption is much slower at longer times (days) due to the low capillary suction in the larger voids [59], [60].

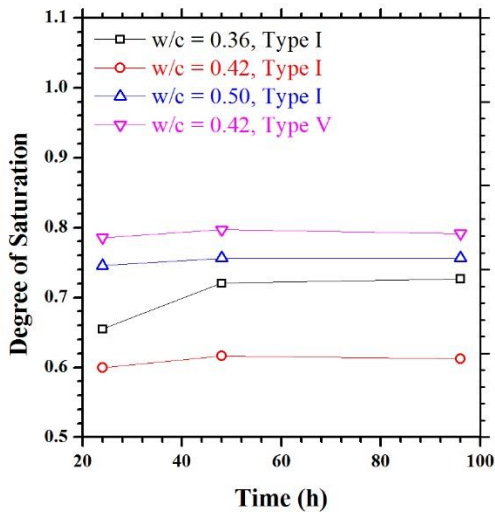


Figure 5.11. Increase in degree of saturation of mortars exposed to deionized water up to 96 h.

## 5.5 Conclusions

This study utilized neutron radiography to measure the depth of fluid penetration and the degree of saturation in four mortars (Type I cement with  $w/c$ 's of 0.36, 0.42, and 0.50 and Type V cement with a  $w/c$  of 0.42) exposed to varying concentrations of  $\text{CaCl}_2$ . The addition of chlorides influences the transport properties of fluid in mortar due to changes in the fluid properties such as surface tension, viscosity and density. In addition,  $\text{CaCl}_2$  salt solutions can react with the cement paste resulting in the formation of expansive reaction

products such as Friedel's salts, Kuzel's salts and calcium oxychloride that can fill in the porosity and damage the matrix. At a low concentration (10% by mass), mortars prepared with Type I cement experienced a reduction in sorptivity between 20 % and 38 % due to a change in fluid properties and the creation of Friedel's and Kuzel's salts, whereas the mortar prepared with Type V cement only reduced in sorptivity by 10 %, due to the change in fluid properties. Cements containing aluminates ( $C_3A$ ) will react with  $CaCl_2$  even at low concentrations to produce pore-blocking salts that reduce the subsequent rate of absorption. At high concentrations, all mortars experienced a dramatic decrease (between 80 % and 87 % decrease) in sorptivity due to the change in fluid properties (increase in viscosity and surface tension) and the formation of calcium oxychloride.

The neutron radiographs enabled the fluid ingress depth and change in degree of saturation to be calculated. From this information, the shape or gradient of the wetting front could be monitored. The wetting front became clearly less sharp as the concentration of chlorides increased. In addition, the phenomenon of pore-blocking with chlorides was observed at high concentrations (29.8 %) of chloride solutions. In this scenario, there is a build-up of chlorides close to the fluid source and a sharp decrease in the amount of fluid past the build-up. This implies that the pores have decreased in volume, therefore the volume of fluid that can penetrate past that barrier decreases as does the rate of further ingress.

## CHAPTER 6. NEUTRON RADIOGRAPHY EVALUATION OF DRYING IN MORTARS WITH AND WITHOUT SHRINKAGE REDUCING ADMIXTURES

### 6.1 Introduction

Research on Shrinkage Reducing Admixtures (SRA) in concrete began in Japan in the 1980's [84]–[86]. In the late 1990s, research in the US began to explore new formulations of SRA as well [87]–[91], as a way to reduce shrinkage and cracking in normal and high strength concrete.

This work builds on the early research to quantify the role of SRA in moisture gradients. The SRAs are chemical surfactants that are added to concrete to reduce the surface tension of the pore fluid. This reduction in surface tension reduces drying shrinkage by reducing the capillary pressure generated and reducing the drying rate that generates higher degrees of saturation (Weiss et al., 1999). Review articles have been developed on the use of SRAs in concrete. These articles describe how the SRAs alter the shrinkage, cracking resistance, mechanical properties and fluid transport [92]–[96]. Many of these properties are measured and related to the properties of the pore solution.

Ai and Young [91] and Pease et al. [97] have provided measures of surface tension of water-SRA solutions. Other authors reported results of surface tension in both water- SRA

solutions and pore solution-SRA solutions at one temperature [98], [99]. Bentz reported that SRA significantly increased solution viscosity at 22 °C at a 10 % concentration [92]. Villani [8], [100] performed a detailed examination of the surface tension and viscosity of SRA solutions at various temperatures.

At a molecular level, surfactants (like SRA) are amphiphilic. Each surfactant molecule is composed of a hydrophilic head that is covalently bonded to a hydrophobic (i.e., non-polar) tail [101]. The hydrophilic head is attracted by polar and hydrogen bonding solvents, such as water, and oppositely charged surfaces. The hydrophobic tail is a non-polar hydrocarbon chain and is attracted by non-polar solvents, such as oil, but is repelled from polar molecules such as water [98]. Adsorption of surfactants at interfaces causes a reduction in the interfacial energy; as such, addition of SRA produces a reduction in the surface tension of the water-air interface.

Schießl [102] examined drying profiles in plain concrete and concrete containing SRA using electrical resistivity. They reported similar electrical resistivity profiles at early ages, implying similar moisture content, however the resolution of the resistivity measurement seemed insufficient for capturing differences between the plain and the SRA system during drying at early age. Bentz et al. [88] reported a change in the drying profile in presence of SRA. While in presence of pure water the drying front remains uniform across the depth (i.e., loss of water simultaneously at all depths during drying), but when SRA are present in the system a sharp drying front forms (i.e. large moisture content change within a few millimeters in depth). Reduction in penetration depth and sorptivity rate of water in dried

samples containing SRA was reported by Weiss [89] and Sant et al. [50]. This was theoretically predicted and related to the increase in viscosity and reduction in surface tension of the fluid [12], [89], [98], as the sorptivity coefficient scales as the square root of surface tension divided by viscosity [13], [14].

Radlinska et al. and Weiss et al. [103], [104] showed the influence of surface tension on the size of the pores emptying during drying and shrinkage over a wide range of relative humidity (RH). Eberhardt [99] reported a change in the desorption isotherm response of systems containing SRA that showed a lower saturation for the same RH compared to systems without shrinkage reducing admixtures..

Neutron radiography is sensitive to hydrogen and therefore can accurately quantify in situ water movement [22]. This method provides a powerful tool in quantifying water in porous materials such as soil and plant roots [25], [27], [28]. Researchers have applied neutron imaging to concrete to assess properties including sorptivity and porosity. Hanžič [43] measured the sorptivity of concrete exposed to water and three types of fuel oil. The results from neutron radiography were compared with sorptivity obtained from a gravimetric method. De Beer [31] measured porosity and sorptivity with neutron radiography and using standard procedures in the lab. There have been previous studies investigating the drying of mortar using neutron imaging [21], [30], [105], [106], but modified solutions such as SRA have yet to be investigated.

## 6.2 Experimental

### 6.2.1 Sample Preparation

One commercially available shrinkage reducing admixture has been used throughout this study [100]. A 5 % SRA solution by mass was used to perform desorption tests and neutron radiography.

Desorption tests and neutron radiography were performed on plain mortar samples that were previously exposed to mild drying and then saturated in the 5 % SRA solution. The mortar used had a water-to-cement mass ratio ( $w/c$ ) of 0.42 and 55 % of fine aggregate by volume. The mixing procedure was in accordance with ASTM C192 [48]. Mortar beams (10 cm wide by 7.5 cm tall by 35.5 cm in length) were cast, demolded after 24 h and then sealed in double bags for one year.

For desorption testing, thin slices were cut ( $0.8 \pm 0.05$ ) mm using a water-cooled diamond-tipped wafer saw, then exposed to drying ( $50 \text{ }^\circ\text{C} \pm 0.5 \text{ }^\circ\text{C}$ ) for 2 d and subsequently submerged in lime water or in 5 % SRA solution for 24 h before testing. A 50 mg to 70 mg portion of the slice was used for testing.

For neutron radiography, 75 mm by 50 mm rectangular slices were cut to  $20 \text{ mm} \pm 1.5 \text{ mm}$  thick with a wet saw. The specimens were then placed under vacuum and evacuated to a pressure of  $(930 \pm 670) \text{ Pa}$  ( $7 \text{ torr} \pm 5 \text{ torr}$ ). After 3 h, lime water or 5 % SRA solution was introduced to the vacuum chamber. The chamber remained under vacuum for an additional hour. The pump was then turned off and the mortar specimen remained submerged in the



solution for 18 h. Each specimen was then removed and completely wrapped in aluminum tape and stored in an airtight plastic container until being imaged (approximately two weeks).

### 6.2.2 Dynamic Vapor Sorption (DVS) testing

Vapor desorption isotherms were measured using a dynamic vapor desorption analyzer (TGA Q5000), where the samples were subjected to a constant temperature while the RH was varied in controlled steps and the mass recorded as a function of time. The test started by equilibrating the sample at 97.5 % RH for either 96 h or until the sample had achieved a stable mass (less than 0.001 % mass change/15 min). The RH was then reduced in the multiple steps (96.5 %, 94.9 %, 90 %, 87.6 %, 83.8 %, 76.8 %, 70 %, 59 %, 50 % and 40 %) and the specimen finally dried to 0 % RH. The multiple steps were chosen in order to accurately capture the desorption curve at high RH where the two systems were expected to differ more substantially. The specific RH steps were chosen to empty specific size pores approximated using the Kelvin-Laplace equation, namely 40 nm, 30 nm, 20 nm, 10 nm, 8 nm, 6 nm, 4 nm, 3 nm, 2 nm and 1.5 nm, when the evaporating fluid is pure water. For each RH step, the sample was allowed to equilibrate for 12 h or 0.001 % (of initial mass of the sample) change in mass over 15 min.

### 6.2.3 Neutron Imaging

Neutron radiography was performed at the Neutron Imaging Facility at the National Institute of Standards and Technology (NIST) in Gaithersburg, MD. The beam-defining aperture had a diameter of 15 mm, a collimation ratio of 450, and a fluence rate of 1.4 x

$10^7 \text{ cm}^{-1}\text{s}^{-1}$ . A scientific complimentary oxide semiconductor (sCMOS) camera viewed a Gadolinium oxysulfide scintillator through a Nikon 85 mm f/1.8 lens with a PK-11a extension tube to create a neutron detector with an effective pixel pitch of  $30 \mu\text{m}$ .

The experiment was set up such that five samples could be imaged in sequence. The samples were placed on an automated, motorized table so that they could be positioned without the beam being turned off, as shown in Figure 6.1. Nine reference images of the fully saturated specimens were captured, each with an exposure time of 60 s. Images of similar samples cut from the same prism in the oven dried condition were also taken. After taking the initial saturated images for each specimen, the top surface of the specimen was exposed to the drying environment. Three images were captured before the stage moved to the next position to image the next sample. As a result of the table movement, approximately 30 min elapsed between each set of images per specimen. To eliminate outliers, images were combined with a median filter in groups of 9 or 3 for reference or drying images, respectively. 30 flat field (open beam) and dark (closed beam) images were also taken and combined with a median filter. The use of a median filter in time eliminated the appearance of streaks due to gamma rays and fast neutrons depositing energy directly into the sCMOS.

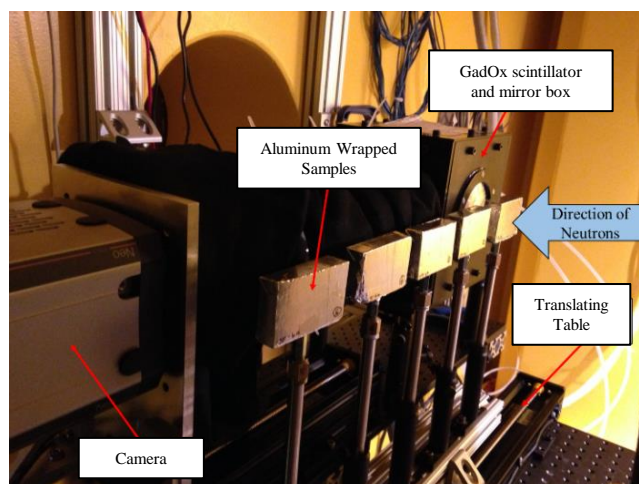


Figure 6.1. Experimental set-up for neutron radiography at the Neutron Imaging Facility. The top aluminum was removed at the start of the drying experiment.

## 6.3 Results

### 6.3.1 Theoretical Observations on the Influence of Liquid Properties on Drying

The change in liquid properties in presence of SRA will affect the mechanism of drying in its various phases [107]. With reference to the three stages of drying widely known (Constant Rate Period, First Falling Rate Period and Second Following Rate Period), the movement of fluid in the same pore structure will be influenced by the changes in viscosity, surface tension and contact angle in each stage as following. It should be noted that liquid properties are continuously changing as drying occurs in a system containing SRA, since water is the principal component leaving the porous system, while SRA remains, thus generating a solution that becomes more and more concentrated as drying proceeds.

The reduction in surface tension and contact angle will increase the liquid vapor pressure, thus increasing the evaporation speed in the *Constant Rate Period* [108], while the increase in viscosity will reduce the fluid flow according to Darcy's law [109].

In the two *Falling Rate Periods*, when the menisci are driven into the pores, evaporation from pendular regions occurs and flow in the funicular region will occur. While the reductions in surface tension and contact angle tend to increase the rate of evaporation in the pendular regions, the increase of viscosity of the SRA solution with respect to pure water will decrease the flow rate of the fluid to these regions.

Additionally, according to the Kelvin-Laplace equation at equilibrium, smaller pores will be emptied in the specimens with SRA for the same external pressure ( $p_a$ ), due to the reduction in surface tension ( $\gamma$ ) and of liquid water activity ( $p_o$ ) (Equation 6.1):

$$r = \frac{2\gamma V_m}{RT \ln(p_a / p_o)} \quad \text{Equation 6.1}$$

where  $V_m$  is the molar volume of the fluid and  $r$  is the capillary radius.

Liquid properties are also expected to influence the drying front generated. Shaw [110] experimentally proved that the width of the drying front in a porous material is inversely proportional to the square root of the capillary pressure gradient [110], [111] and inversely proportional to the velocity of the drying front. Shaw also suggested that in presence of fast drying, which is the case studied in this work, the fluid flow is the dominant mechanism that controls the pressure gradient generated across the drying front. In the presence of fluid

flow, the velocity of the drying front can be then related to the pressure gradient and viscosity according to Darcy's law:

$$v = -\frac{\kappa}{\Phi} \cdot \frac{\Delta p}{\mu} \quad \text{Equation 6.2}$$

where  $v$  is the velocity of the fluid,  $k$  is the liquid permeability,  $\Phi$  is the total porosity,  $\Delta P$  is the capillary pressure gradient across the drying front and  $\mu$  is the viscosity of the wetting fluid. It is hypothesized that in presence of SRA, during the first, instantaneous, phase of drying a larger pressure gradient is generated as a consequence of the reduction in surface tension. The velocity of the drying front will be then defined by the combination of the effect of the increased pressure gradient and of the increased viscosity.

### 6.3.2 Desorption Isotherms

Changes in the desorption curves are expected when liquid properties are altered. Assuming the validity of the Kelvin-Laplace equation (Equation 6.1), surface tension, contact angle and density will be responsible for altering the amount of fluid in equilibrium at different relative humidities. Conversely, viscosity will mainly alter the rate of drying, modifying the flow of fluid in funicular conditions according to Darcy's law (Equation 6.2). Specifically, the equilibrium water content at different relative humidities is supposed to decrease in the presence of SRA due to the reduction in surface tension and contact angle since smaller pores are emptying out. Conversely, the drying time would increase due to the increase of viscosity especially when the funicular conditions are prevailing at high relative humidities.

The desorption curves are presented in Figure 6.2(a), where the equilibrium water content is shown as a function of RH for the systems saturated in water and in 5 % SRA solution. It can be seen that at high relative humidities, the sample containing SRA shows a lower mass at equilibrium, as expected from theory. The longer drying time at high RH for the sample initially saturated in SRA solution is experimentally confirmed in Figure 6.2(b) where it can be noticed that the equilibrium mass at 60 % RH is reached after 78 h (280000 s) while for the sample containing only water, the equilibrium is reached after only 33 h (120000 s).

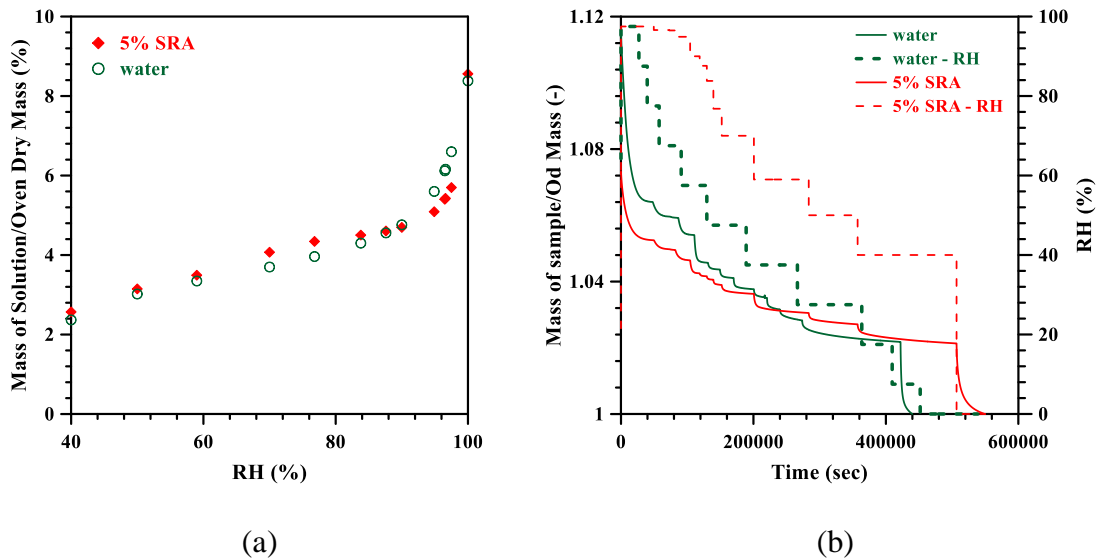


Figure 6.2. (a) equilibrium water content for mortar saturated in water or in 5 % SRA solution (standard deviation within 0.1 and 0.9% in the RH range analyzed, based on two desorption tests performed on water saturated samples); (b) normalized mass and RH versus time during vapor desorption testing.

Information on the porous structure and on the liquid properties allow one to predict changes in the desorption isotherm. Changes in the desorption curve can be evaluated adopting a two-step approach:

First, perform a desorption test for a sample initially saturated in water to evaluate the cumulative pore size distribution and vacuum saturate a sample to quantify the total porosity of the material [52]. The differential pore volume can then be quantified for each pore range analyzed, assuming the validity of the Kelvin-Laplace equation. In this study, the last step has been done considering the density of water to be equal to  $1000 \text{ kg/m}^3$ .

Second, assuming that no changes occur in the porous system (total porosity and pore size distribution) of a fully hydrated material (degree of hydration  $> 85 \%$ ) during saturation in SRA solution, the desorption isotherm of the system containing SRA solution can be approximately quantified considering only the reduction in surface tension. The lone influence of surface tension can be considered if presenting the desorption isotherm in volumetric terms and assuming the validity of the Kelvin-Laplace equation when negligible changes in the liquid vapor pressure and liquid molar volume occur. For a 5 % SRA solution, the surface tension is assumed constant and equal to  $0.036 \text{ N/m}$  [100].

The comparison between the experimental desorption curve and the model is presented in Figure 6.3. A very good correspondence between the model and the experimental curve is obtained at high relative humidities ( $> 95 \%$ ), while the two curves deviate at lower RH, likely due to the non-uniformity of the remaining, concentrated SRA solution. However,

if a gravimetric type of desorption isotherm is required, information on the density of the fluid needs to be provided. Knowing the density is challenging, since it is directly related to the mass loss (i.e., the density of the solution is a function of the SRA solution concentration) which is unknown in the problem. A first order approximation can be obtained assuming that water is the only component leaving the system (not SRA) and that SRA does not modify the way water leaves the porous system.

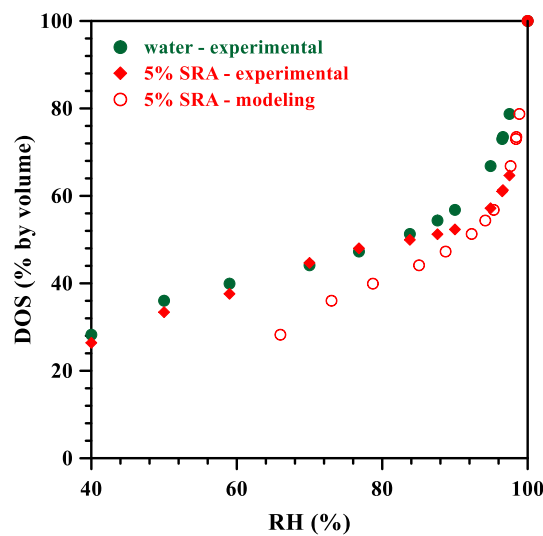


Figure 6.3. Experimental and modeled desorption isotherms for a cementitious mortar saturated in water and 5 % SRA solution, presented in terms of volumetric degree of saturation (DOS by volume)

### 6.3.3 Moisture Diffusion Coefficient

The desorption data can further be used to quantify the non-linear diffusion coefficient with respect to RH according to an approach proposed by Anderberg and Wadsö [112]. This approach assumes the sample can be approximated as a slab drying from two sides and assumed a linear change of mass over the square root of time within a specific range. The



diffusion coefficient with respect to RH for samples initially saturated in water and 5 % SRA are presented in Figure 6.4. The calculation has been performed in this study considering the mass range corresponding to 10 % to 50 % of the total mass lost in each RH step. Slower drying is confirmed for the system containing SRA that shows a lower diffusion coefficient for the entire range of relative humidities compared to the sample saturated in water.

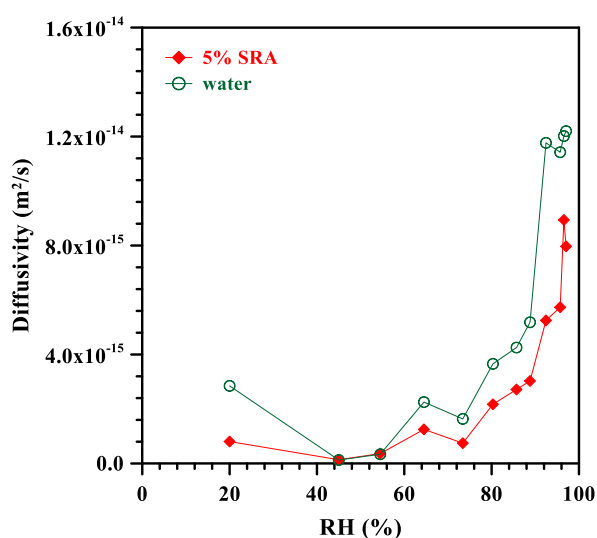


Figure 6.4. Diffusion coefficient with respect to RH evaluated from desorption data for samples saturated in water and 5 % SRA solution

Changes in the diffusion coefficient when liquid properties are altered can be predicted using the approach introduced by Villani et al. [100]. The increase in viscosity due to SRA alters the portion of the diffusion coefficient associated with liquid diffusion at high relative humidities, while the surface tension alters both the vapor and the liquid portions [100], [113], [114]. Specifically, the increase of viscosity and the decrease of surface tension are

both responsible for the reduction in the diffusion coefficient as confirmed experimentally in Figure 6.4.

#### 6.3.4 Moisture Profiles

The spatial change in water content was measured using neutron radiography. The water content was determined for the middle third of the sample. Many researchers normalize images to an image of the same sample in a completely dry state and measure the change in water content directly, if the attenuation coefficient of water is known [22], [29], [50], [115]. Since the final goal was to determine the degree of saturation, the mass of water lost while drying had to be normalized by the total volume of pores. As the volume of water that is lost from the samples is smaller than an equivalent thickness of 5 mm [7], beam hardening effects can be neglected in this analysis. Assuming the volume of pores is constant through the 20 mm cross section of the mortar, the total volume of pores per pixel can be estimated by Equation 6.3 where the quantity  $I_{dry}/I_{sat}$  is the constant value of the ratio of the average intensity of a mortar sample in the oven dried condition to the intensity completely saturated,  $t_{sample}$  is the thickness of the sample and  $\mu_w$  is the attenuation coefficient of water.

$$V_{total} = \frac{\ln\left(\frac{I_{sat}}{I_{dry}}\right)}{\mu_w t_{sample}} \quad \text{Equation 6.3}$$

Similarly, the change in volume of water per pixel can be computed at each position from the drying edge,  $i$  and time  $t$ . The quantity  $(I_{i,t}/I_{i,0})$  is simply the image intensity of a sample

at a specified time normalized to the image intensity of that sample at time  $t=0$  when fully saturated.

$$\Delta V = \frac{\ln\left(\frac{I_{i,t}}{I_{i,0}}\right)}{\mu_w t_{sample}} \quad \text{Equation 6.4}$$

The degree of saturation at each position from the drying edge,  $i$  and time  $t$  can be computed using Equation 6.5. Assuming the thickness of the samples to be constant, Equation 6.5 has the advantage of not having to measure the attenuation coefficient of water.

$$S_{i,t} = 1 - \frac{\ln\left(\frac{I_{i,0}}{I_{i,t}}\right)}{\ln\left(\frac{I_{sat}}{I_{dry}}\right)} \quad \text{Equation 6.5}$$

The computed degree of saturation along the sample is presented in Figure 6.5. It is clear that the moisture gradient is sharper in the SRA system and initially only acts within the first 5 mm from the drying surface. The water system shows a highly variable gradient through the first 10 mm from the drying surface. As described previously, the mortar with the SRA solution maintained a higher degree of saturation (more moisture) due to a reduced diffusion coefficient. This can also be seen visually throughout the samples in Figure 6.7. The water system appears to lose more water, particularly near the surface, as compared to the SRA system. Similar results, but with an even more pronounced difference in the drying fronts between plain and SRA systems, have been obtained on fresh cement pastes prepared with water and with SRA solutions (SRA content of 2 % by mass of cement) using X-ray transmission [88].

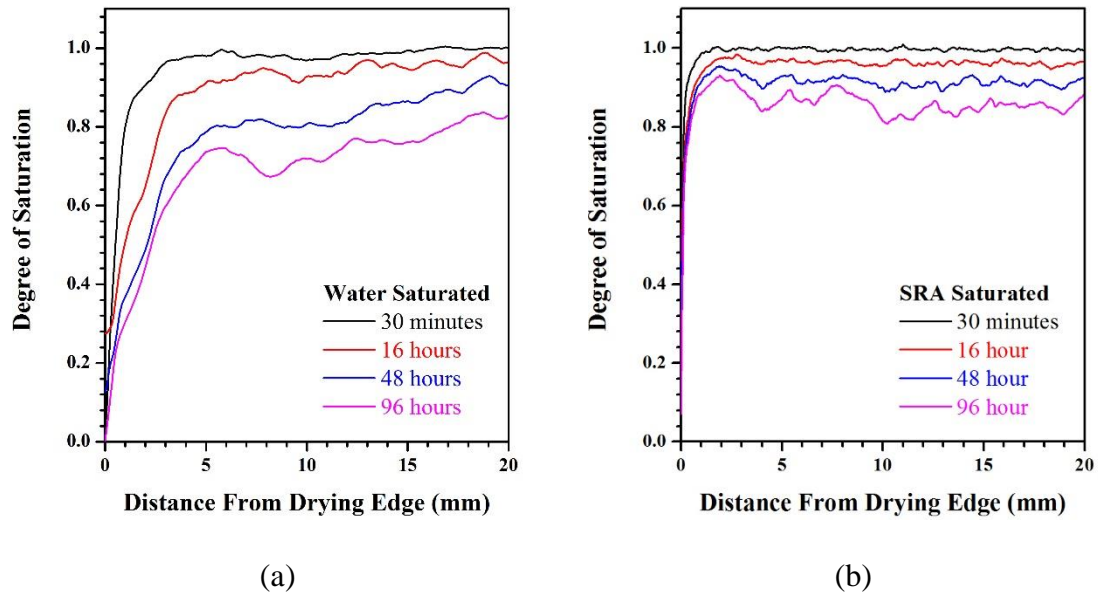


Figure 6.5. Average moisture profile in terms of degree of saturation for mortar samples drying from one edge for a system saturated in (a) lime water and (b) 5% SRA solution.

The results of Figure 6.5 can be analyzed in terms of RH or capillary pressure. In Figure 6.6, the degree of saturation of both samples at their core after 96 h of drying has been converted into RH and then into capillary pressure, using the experimental desorption isotherms and the Kelvin-Laplace equation, respectively. The conversion between degree of saturation and RH has been used in the regions (drying edge and core of the samples) where quasi-equilibrium conditions are verified. It can be seen from Figure 6.6. Relation between DOS, RH and capillary pressure in the systems containing water and SRA that the capillary pressure gradient generated across the drying front with respect to the edge of the sample is higher for the sample containing SRA, while the width of the drying front is smaller [110]. The velocity of the movement of the drying front (Figure 6.5), however,

seems lower in the presence of SRA, highlighting that the effect of the increased viscosity in presence of SRA is significant with respect to the effect of the capillary pressure gradient.

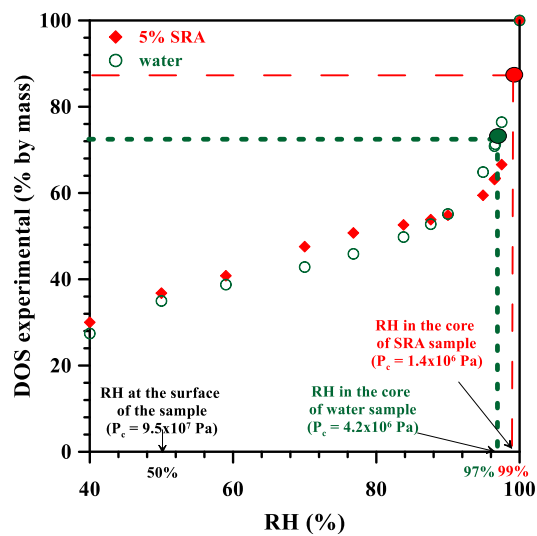


Figure 6.6. Relation between DOS, RH and capillary pressure in the systems containing water and SRA

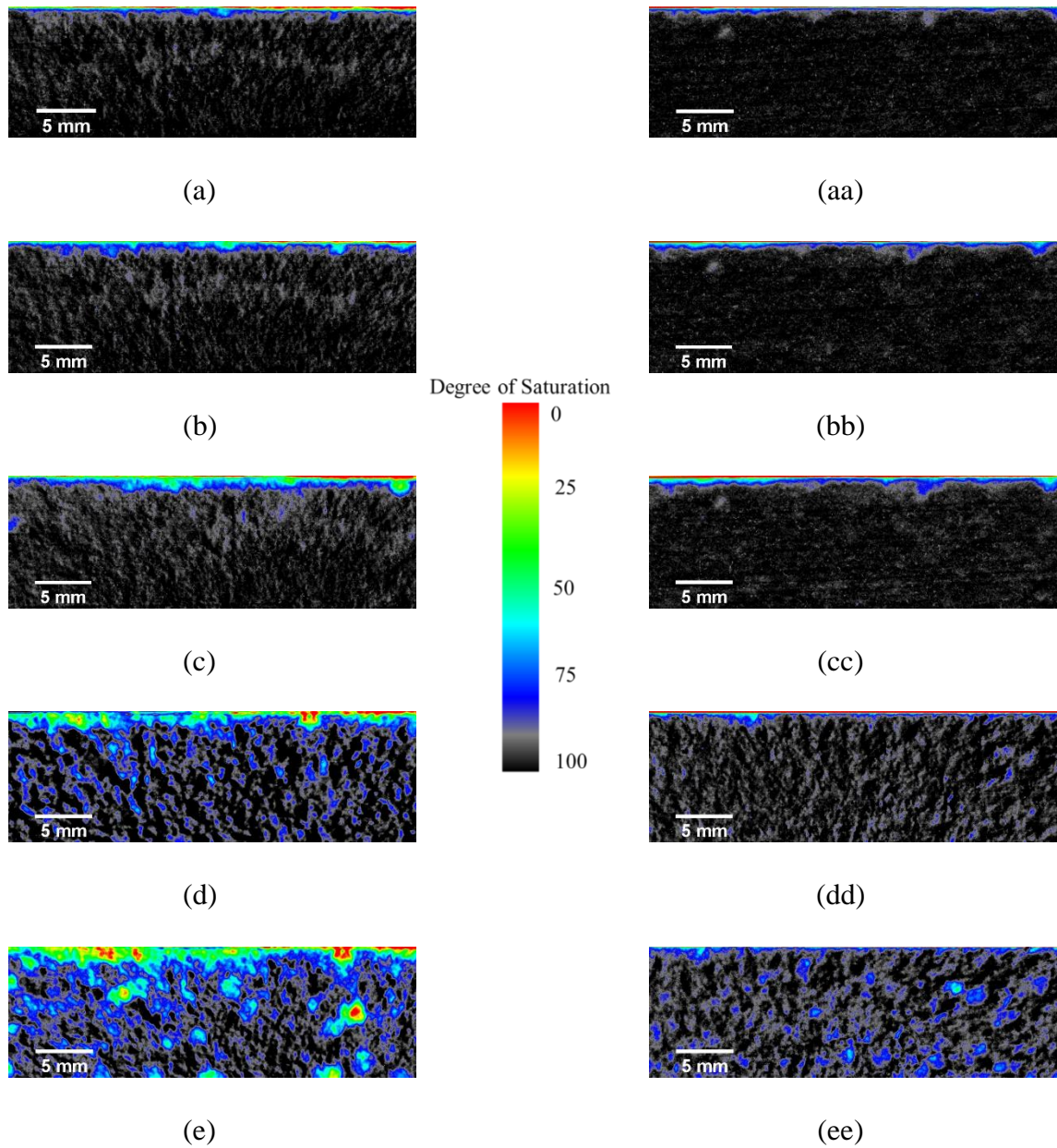


Figure 6.7. Change in the DOS in the first 12 mm from the drying surface in a mortar saturated in lime water (a,b,c,d,e) and in a mortar saturated in 5 % SRA (aa,bb,cc,dd,ee) solution at (a, aa) 30 min, (b, bb) 2.5 h, (c, cc) 6 h, (d, dd) 16 h and (e, ee) 48 h after being exposed to the drying environment.

#### 6.4 Conclusions

Shrinkage Reducing Admixtures (SRA) have been known to reduce the capillary pressure and minimize restrained shrinkage cracking by reducing surface tension of the pore solution. SRA however also impacts other fluid properties such as viscosity, contact angle and density, resulting in alteration of absorption and desorption processes in cementitious materials.

The drying process is influenced by the presence of SRA in solution, due to the reductions of surface tension and contact angle that increase the rate of evaporation in pendular conditions. The viscosity increase of SRA solution slows the flow in funicular regions. The desorption curves will be consequently altered. Specifically the decrease in surface tension and contact angle modified the amount of solution in equilibrium at different relative humidities (“volumetric” desorption curve) and reduced the size of pores emptying at certain RH. The increased viscosity of SRA solution extended the drying time of cementitious samples during desorption testing.

From theoretical considerations, the increase in viscosity and the reduction in surface tension would be responsible for a decrease in the moisture diffusion coefficient. This aspect was confirmed by calculating diffusion coefficient values from desorption isotherms. The diffusion coefficients were lower for the cementitious system saturated in SRA solution compared to the system saturated in water, for the entire range of relative humidities analyzed.

The effect of SRA on solution properties and further on drying was confirmed from measurements performed using neutron radiography. Moisture profiles, in terms of degree of saturation, were obtained that further confirmed the higher degree of saturation experienced in systems containing SRA related to the proven reduction of the moisture diffusion coefficient. From neutron radiography measurements, it was also possible to visualize the sharper drying front generated in the system containing SRA, which appears related to their increased capillary pressure gradient and higher solution viscosity.



## CHAPTER 7. CONCLUSIONS AND FUTURE WORK

### 7.1 Summary of Current Work

Understanding transport properties is becoming increasingly more important as the industry strives to accurately predict the service life of concrete elements. Neutron radiography is an effective method for visualizing and quantifying small changes in moisture content in mortar and can provide information that is unattainable using standard concrete test methods. This thesis focused on fluid absorption in an unsaturated system, and drying in systems containing SRA.

The first part of this thesis, CHAPTER 3, compared typical results for standard absorption test with measured depth of penetration from neutron radiographs. The results from the standard test should be carefully analyzed and not interpreted as the depth of fluid penetration although the units of absorption are  $\text{mm}^3/\text{mm}^2$  or mm. Mortars with and without entrained air were exposed to water for 12 hours. This duration of time is within the expected range of the initial absorption which is controlled by capillary action through the small pores rather than the slow secondary absorption that is controlled by the air voids. Using neutron radiography, it can be known with certainty where the water flows and the volume of fluid occupying the pores. Standard laboratory test methods based on changes in mass during absorption do not describe the spatial distribution or the degree of saturation

in the wetted front. However, by normalizing the volume of absorbed water to the volume of small pores (namely gel and capillary, as computed by Powers Model), the actual depth of penetration can be calculated until the water front reaches the edge of the specimen.

The implications of the results of CHAPTER 3 exceed the reinterpretation of ASTM C1585 results. The results of the neutron imaging definitively quantified the degree of saturation throughout the mortar while absorbing water. This degree of saturation ( $S_{matrix}$ ) is the degree of saturation that an element of concrete will achieve before the slow process of filling air voids will begin. The degree of saturation is strongly linked with freeze-thaw performance and entrained air is added in order to lower the degree of saturation. By knowing that the gel and capillary pores fill initially, the value of can  $S_{matrix}$  be calculated and concrete mixtures can be designed such that  $S_{matrix}$  remains well below the critical degree of saturation [116].

A model for the attenuation of neutrons through mortars was developed as described in CHAPTER 4. The attenuation coefficients of the raw materials were measured and the attenuation of the hydration products was calculated. Using these coefficients in conjunction with the known volume fraction of each constituent, the total amount of water in the system can be determined. This model allows for flexibility in experiments. For example, mortar can be pre-conditioned to an initial relative humidity and the total moisture content can be calculated.

The work presented in CHAPTER 5 builds upon previous research on absorption of chloride solutions in mortar. The current ASTM standard for measuring absorption in concrete does not have specific corrections for fluids aside from water, but other researchers have made corrections based on fluid properties such as density, viscosity, and surface tension. Theoretically, the rate of fluid absorption is reduced by the square root of the ratio of surface tension to viscosity. Neutron radiography allowed for the direct measurement of the sorption and it was found that the sorption was lower than the expected theoretical sorption for mortar prepared with Type I cement. In the mortar prepared with Type V cement, the value of sorption was essentially the same when exposed to 10 %  $\text{CaCl}_2$ , but deviated from the theoretical expectation at 20 % and 29.8 %  $\text{CaCl}_2$ . This implies that mortar with Type I cement containing calcium aluminates are forming Friedel's and Kuzel's salts at low concentrations while mortars with Type V cement are not. However, at high concentrations, the large decrease in sorptivity can be attributed to the additional formation of calcium oxychloride in all mortars, regardless of cement composition.

CHAPTER 6 investigated the drying behavior of mortar containing water or 5 % shrinkage reducing admixtures. Neutron radiography allowed for the moisture profile of the drying mortar to be measured at a high resolution. SRA solutions increase the viscosity of the pore solution which slows the flow of the (and decreases the depth of the drying front) while the decrease in surface tension decreases the diffusivity (thus the bulk of the mortar remains at a higher degree of saturation).

## 7.2 Suggestions for Future Work

The data collected from neutron radiography opens up many future research opportunities.

- The mortars used in CHAPTER 3 and CHAPTER 4 were oven dried prior to exposure to water. Future studies can monitor absorption using radiography with varying initial relative humidities. Equation 3.7 can be expanded to account for initially filled porosity to estimate the depth of penetration.
- Mortars exposed to 29.8%  $\text{CaCl}_2$  in CHAPTER 5 showed very little fluid penetration with a two-part moisture front. To expand on this work, samples exposed to high concentrations of calcium chloride can be imaged oven dried before exposure, during absorption, then oven dried again and imaged. This series of images separates the fluid from the reaction products (Kuzel's or Friedels salts or calcium oxychloride) and could explain the peaks in Figure 5.10.
- Shrinkage strains can be computed from the moisture profiles of mortar drying with and without shrinkage reducing admixtures. This data can be related to experimental curling or measured shrinkage.
- Neutron radiography or tomography can be used to investigate the moisture movement from a repair material to a mortar substrate.

## REFERENCES

- [1] W. Li, M. Pour-Ghaz, J. Castro, and J. Weiss, “Water Absorption and Critical Degree of Saturation Relating to Freeze-Thaw Damage in Concrete Pavement Joints,” *J. Mater. Civ. Eng.*, vol. 24, no. 3, pp. 299–307, 2012.
- [2] G. Fagerlund, “The international cooperative test of the critical degree of saturation method of assessing the freeze/thaw resistance of concrete,” *Mater. Struct.*, vol. 10, no. 4, pp. 231–253, 1977.
- [3] Y. Farnam, S. Dick, A. Weise, J. Davis, D. Bentz, and W. J. Weiss, “The Influence of Calcium Chloride Deicing Salt on Phase Changes and Damage Development in Cementitious Materials,” *Submitt. to Cem. Concr. Compos.*, p. 41, 2014.
- [4] Y. Farnam, T. Washington, and J. Weiss, “The Influence of Calcium Chloride Salt Solution on the Transport Properties of Cementitious Materials,” *Submitt. to J. Adv. Civ. Eng.*, 2015.
- [5] ASTM Standard C1585-13, “Standard Test Method for Measurement of Rate of Absorption of Water by Hydraulic-Cement Concretes.” ASTM International, West Conshohocken, PA, 2013.

- [6] C. L. Lucero, D. P. Bentz, D. S. Hussey, D. L. Jacobson, and W. J. Weiss, “Using Neutron Radiography to Quantify Water Transport and the Degree of Saturation in Entrained Air Cement Based Mortar,” *Phys. Procedia*, 2015.
- [7] C. L. Lucero, R. P. Spragg, D. P. Bentz, D. S. Hussey, D. L. Jacobson, and W. J. Weiss, “Using neutron radiography to measure the absorption of calcium chloride solution in mortar,” *Prep.*, 2015.
- [8] C. Villani, C. L. Lucero, D. P. Bentz, D. S. Hussey, D. L. Jacobson, and W. J. Weiss, “Neutron Radiography Evaluation of Drying in Mortars with and without Shrinkage Reducing Admixtures,” *ACI Spec. Publ.*, 2015.
- [9] J. C. Domanus, *Practical Neutron Radiography*. 1992, p. 270.[10] R. P. Feynman, R. B. Leighton, and M. L. Sands, *The Feynman Lectures on Physics*, vol. 1. Addison-Wesley, 1963.[11] H. Berger, “Neutron Radiography,” *Annu. Rev. Nucl. Sci.*, vol. 21, pp. 335–364, 1971.
- [12] G. Sant, A. Eberhardt, D. Bentz, and J. Weiss, “Influence of Shrinkage-Reducing Admixtures on Moisture Absorption in Cementitious Materials at Early Ages,” *J. Mater. Civ. Eng.*, no. March, pp. 277–286, 2010.
- [13] S. Kelham, “A water absorption test for concrete,” *Mag. Concr. Res.*, vol. 40, no. 143, p. 106, 1988.
- [14] C. Hall, “Barrier performance of concrete - A review of fluid transport theory,” *Mater. Struct.*, pp. 291–306, 1994.
- [15] T. C. Powers and T. L. Brownyard, “Studies of the physical properties of hardened portland cement paste,” *PCA Bull. Portl. Cem. Assoc.*, vol. 43, pp. 1–356, 1948.

- [16] C. Matano, "On the relation between the diffusion-coefficients and concentrations of solid metals (The nickel-copper system)," *Jpn. J. Phys.*, vol. 8, pp. 109–113, 1933.
- [17] C. Hall and W. D. Hoff, *Water Transport in Brick, Stone and Concrete*, 2nd ed. CRC Press, 2009, p. 392.
- [18] L. H. Boltzmann, "Zur Integration der Diffusions Gleichung bei Variablen Diffusions Coeffiecienten.," *Ann. Der Phys.*, p. 289, 1894.
- [19] M. Pour-Ghaz, F. Rajabipour, J. Couch, and J. Weiss, "Numerical and Experimental Assessment of Unsaturated Fluid Transport in Saw-Cut (Notched) Concrete Elements," *ACI Spec. Publ.*, pp. 73–86, 2009.
- [20] C. Hall, "Anomalous diffusion in unsaturated flow: Fact or fiction?," *Cem. Concr. Res.*, vol. 37, no. 3, pp. 378–385, Mar. 2007.
- [21] P. Trtik, B. Münch, W. J. Weiss, A. Kaestner, I. Jerjen, L. Josic, E. Lehmann, and P. Lura, "Release of internal curing water from lightweight aggregates in cement paste investigated by neutron and X-ray tomography," *Nucl. Instruments Methods Phys. Res. Sect. A Accel. Spectrometers, Detect. Assoc. Equip.*, vol. 651, no. 1, pp. 244–249, Sep. 2011.
- [22] D. S. Hussey, D. Spornjak, a. Z. Weber, R. Mukundan, J. Fairweather, E. L. Brosna, J. Davey, J. S. Spendelow, D. L. Jacobson, and R. L. Borup, "Accurate measurement of the through-plane water content of proton-exchange membranes using neutron radiography," *J. Appl. Phys.*, vol. 112, no. 10, p. 104906, 2012.

- [23] D. S. Hussey, K. J. Coakley, E. Baltic, and D. L. Jacobson, “Improving quantitative neutron radiography through image restoration,” *Nucl. Instruments Methods Phys. Res. Sect. A Accel. Spectrometers, Detect. Assoc. Equip.*, vol. 729, pp. 316–321, Nov. 2013.
- [24] D. S. Hussey, E. Baltic, and D. L. Jacobson, “Water content measurement of gas diffusion media and membranes by neutron radiography,” *ECS Trans.*, vol. 33, no. 1, pp. 1385–1395, 2010.
- [25] C. L. Cheng, M. Kang, E. Perfect, S. Voisin, J. Horita, H. Z. Bilheux, J. M. Warren, D. L. Jacobson, and D. S. Hussey, “Average Soil Water Retention Curves Measured by Neutron Radiography,” *Soil Sci. Soc. Am. J.*, vol. 76, no. 4, p. 1184, 2012.
- [26] F. C. de Beer, M. F. Middleton, and J. Hilson, “Neutron radiography of porous rocks and iron ore.,” *Appl. Radiat. Isot.*, vol. 61, no. 4, pp. 487–95, Oct. 2004.
- [27] U. Matsushima, W. B. Herppich, N. Kardjilov, W. Graf, A. Hilger, and I. Manke, “Estimation of water flow velocity in small plants using cold neutron imaging with D2O tracer,” *Nucl. Instruments Methods Phys. Res. Sect. A Accel. Spectrometers, Detect. Assoc. Equip.*, vol. 605, pp. 146–149, Jun. 2009.
- [28] S. E. Oswald, M. Menon, A. Carminati, P. Vontobel, E. Lehmann, and R. Schulin, “Quantitative Imaging of Infiltration, Root Growth, and Root Water Uptake via Neutron Radiography,” *Vadose Zo. J.*, vol. 7, no. 3, p. 1035, 2008.



- [29] F. C. De Beer, M. F. Middleton, and J. Hilson, "Neutron radiography of porous rocks and iron ore," *Appl. Radiat. Isot.*, vol. 61, pp. 487–495, 2004.
- [30] F. C. de Beer, W. J. Strydom, and E. J. Griesel, "The drying process of concrete: a neutron radiography study.," *Appl. Radiat. Isot.*, vol. 61, no. 4, pp. 617–23, Oct. 2004.
- [31] F. C. de Beer, J. J. le Roux, and E. P. Kearsley, "Testing the durability of concrete with neutron radiography," *Nucl. Instruments Methods Phys. Res. Sect. A Accel. Spectrometers, Detect. Assoc. Equip.*, vol. 542, pp. 226–231, Apr. 2005.
- [32] P. Vontobel, E. H. Lehmann, R. Hassanein, and G. Frei, "Neutron tomography: Method and applications," *Phys. B Condens. Matter*, vol. 385–386, pp. 475–480, Nov. 2006.
- [33] A. K. Heller, L. Shi, J. S. Brenizer, and M. M. Mench, "Initial water quantification results using neutron computed tomography," *Nucl. Instruments Methods Phys. Res. Sect. A Accel. Spectrometers, Detect. Assoc. Equip.*, vol. 605, no. 1–2, pp. 99–102, Jun. 2009.
- [34] J. D. Schaap, P. Lehmann, a. Kaestner, P. Vontobel, R. Hassanein, G. Frei, G. H. de Rooij, E. Lehmann, and H. Flühler, "Measuring the effect of structural connectivity on the water dynamics in heterogeneous porous media using speedy neutron tomography," *Adv. Water Resour.*, vol. 31, no. 9, pp. 1233–1241, Sep. 2008.
- [35] G. Fagerlund, "The long-time water absorption in the air-pore structure of concrete," 1993.

- [36] J. Castro, D. Bentz, and J. Weiss, “Effect of sample conditioning on the water absorption of concrete,” *Cem. Concr. Compos.*, vol. 33, no. 8, pp. 805–813, Sep. 2011.
- [37] C. Hall and M. H. Raymond Yau, “Water movement in porous building materials—IX. The water absorption and sorptivity of concretes,” *Build. Environ.*, vol. 22, no. 1, pp. 77–82, Jan. 1987.
- [38] N. Martys, “Survey of Concrete Transport Properties and their Measurement,” NISTIR 5592, 1995.
- [39] J. Weiss, M. R. Geiker, and K. K. Hansen, “Using X-Ray Transmission / Attenuation to Quantify Fluid Absorption in Cracked Concrete,” *ASTM Int.*, pp. 1–18, 2002.
- [40] S. A. Hall, D. Hughes, and S. Rowe, “Local characterisation of fluid flow in sandstone with localised deformation features through fast neutron imaging,” *EPJ Web Conf.*, vol. 6, p. 7, Jun. 2010.
- [41] S. N. Herringer, G. Bearman, and H. Z. Bilheux, “Quantification of water absorption and transport in parchment,” *World Conference of Neutron Radiography*. Grindelwald, Switzerland.
- [42] D. R. M. Brew, F. C. de Beer, M. J. Radebe, R. Nshimirimana, P. J. McGlenn, L. P. Aldridge, and T. E. Payne, “Water transport through cement-based barriers—A preliminary study using neutron radiography and tomography,” *Nucl. Instruments Methods Phys. Res. Sect. A Accel. Spectrometers, Detect. Assoc. Equip.*, vol. 605, no. 1–2, pp. 163–166, Jun. 2009.

- [43] L. Hanžič and R. Ilić, “Relationship between liquid sorptivity and capillarity in concrete,” *Cem. Concr. Res.*, vol. 33, no. 9, pp. 1385–1388, Sep. 2003.
- [44] P. Zhang, F. H. Wittmann, T. Zhao, E. H. Lehmann, and P. Vontobel, “Neutron radiography, a powerful method to determine time-dependent moisture distributions in concrete,” *Nucl. Eng. Des.*, vol. 241, no. 12, pp. 4758–4766, Dec. 2011.
- [45] A. Gerdes, F. H. Whittmann, and E. Lehmann, “Characterisation of transport processes in surface near zones of concrete by means of neutron radiography,” *PSI Annu. Rep.*, vol. VI, p. 56.
- [46] P. Zhang, F. H. Wittmann, T. J. Zhao, E. H. Lehmann, L. Tian, and P. Vontobel, “Observation and quantification of water penetration into Strain Hardening Cement-based Composites (SHCC) with multiple cracks by means of neutron radiography,” *Nucl. Instruments Methods Phys. Res. Sect. A Accel. Spectrometers, Detect. Assoc. Equip.*, vol. 620, pp. 414–420, Aug. 2010.
- [47] M. Kanematsu, I. Maruyama, T. Noguchi, H. Iikura, and N. Tsuchiya, “Quantification of water penetration into concrete through cracks by neutron radiography,” *Nucl. Instruments Methods Phys. Res. Sect. A Accel. Spectrometers, Detect. Assoc. Equip.*, vol. 605, no. 1–2, pp. 154–158, Jun. 2009.
- [48] ASTM Standard C192/C192M-13, “Standard Practice for Making and Curing Concrete Test Specimens in the Laboratory.” ASTM International, West Conshohocken, PA, 2013.

- [49] ASTM Standard C213/C231M-13, “Standard Test Method for Air Content of Freshly Mixed Concrete by the Pressure Method.” ASTM International, West Conshohocken, PA, 2014.
- [50] G. Sant and W. J. Weiss, “Using X-Ray Absorption to Assess Moisture Movement in Cement-Based Materials,” *J. ASTM Int.*, vol. 6, no. 9, p. 15, 2009.
- [51] O. M. Jensen and P. F. Hansen, “Water-entrained cement-based materials,” *Cem. Concr. Res.*, vol. 31, no. 4, pp. 647–654, Apr. 2001.
- [52] Y. Bu, R. P. Spragg, and W. J. Weiss, “Comparison of the Pore Volume in Concrete as Determined Using ASTM C642 and Vacuum Saturation,” *Adv. Civ. Eng. Mater.*, vol. 3, no. 1, pp. 308–315, 2014.
- [53] S. Mindess, J. F. Young, and D. Darwin, *Concrete*, 2nd ed. Prentice Hall, 2002, p. 644.
- [54] W. Li, M. Pour-Ghaz, P. Trtik, M. Wyrzykowski, B. Münch, P. Lura, P. Vontobel, E. Lehmann, and W. J. Weiss, “Using Neutron Radiography to Assess Water Absorption in Air Entrained Mortar,” *In Preparation..*
- [55] G. Fagerlund, “Chemically bound water as measure of degree of hydration: method and potential errors,” 2009.
- [56] F. Grünauer, “Image deconvolution and coded masks in neutron radiography,” *Nucl. Instruments Methods Phys. Res. Sect. A Accel. Spectrometers, Detect. Assoc. Equip.*, vol. 542, no. 1–3, pp. 342–352, Apr. 2005.
- [57] A.-J. Dianoux and G. Langer, *Neutron Data Booklet*. Philadelphia, PA: Old City Publishing, 2003.

- [58] B. Hammouda, “Coherent and Incoherent Neutron Scattering,” 2013. [Online]. Available:  
[http://www.ncnr.nist.gov/staff/hammouda/distance\\_learning/chapter\\_9.pdf](http://www.ncnr.nist.gov/staff/hammouda/distance_learning/chapter_9.pdf).  
[Accessed: 04-Oct-2014].
- [59] I. Ioannou, A. Hamilton, and C. Hall, “Capillary absorption of water and n-decane by autoclaved aerated concrete,” *Cem. Concr. Res.*, vol. 38, no. 6, pp. 766–771, Jun. 2008.
- [60] N. S. Martys and C. F. Ferraris, “Capillary transport in mortars and concrete,” *Cement and Concrete Research*, vol. 27. pp. 747–760, 1997.
- [61] W. Jones, Y. Farnam, P. Imbrock, J. Spiro, C. Villani, J. Olek, and W. J. Weiss, “An Overview of Joint Deterioration in Concrete Pavement: Mechanisms, Solution Properties, and Sealers,” West Lafayette, Indiana, 2013.
- [62] L. Sutter, K. Peterson, G. Julio-Betancourt, D. Hooton, T. Van Dam, and K. Smith, “The deleterious chemical effects of concentrated deicing solutions on Portland cement concrete,” Pierre, South Dakota, 2008.
- [63] D. Harris, Y. Farnam, R. P. Spragg, P. Imbrock, and W. J. Weiss, “Early Detection of Joint Distres in Portland Cement Concrete Pavements,” West Lafayette, Indiana, No. SPR 3623, 2015.
- [64] D. Harris, P. Imbrock, and W. J. Weiss, “Using Ground-Penetrating Radar to Detect Indicators of Premature Joint Deterioration in Concrete Pavements,” in *Transportation Research Board 94th Annual Meeting*, 2015.

- [65] K. Raoufi, T. Nantung, and W. J. Weiss, "Numerical analysis of saw cutting: The influence of environmental conditions," *Am. Concr. Institute, ACI Spec. Publ.*, no. 266 SP, pp. 87–99, 2009.
- [66] K. Coates, S. Mohtar, B. Tao, and W. J. Weiss, "Can Soy Methyl Esters Reduce Fluid Transport and Improve the Durability of Concrete?," *Transp. Res. Board*, vol. 2113, pp. 22–30, 2009.
- [67] D. P. Bentz, M. A. Ehlen, C. F. Ferraris, and E. J. Garboczi, "Sorptivity-based service life predictions for concrete pavements," in *7th International Conference on Concrete Pavements—Orlando, Florida, USA, Sept, 2001*, vol. 1, pp. 9–13.
- [68] G. Fagerlund, "Critical Degrees of Saturation at Freezing of Porous and Brittle Materials," 1973.
- [69] C. Villani, R. Spragg, M. Pour-Ghaz, and W. Jason Weiss, "The Influence of Pore Solutions Properties on Drying in Cementitious Materials," *J. Am. Ceram. Soc.*, vol. 97, no. 2, pp. 386–393, Oct. 2013.
- [70] R. P. Spragg, J. Castro, W. Li, M. Pour-Ghaz, P.-T. Huang, and J. Weiss, "Wetting and drying of concrete using aqueous solutions containing deicing salts," *Cem. Concr. Compos.*, vol. 33, no. 5, pp. 535–542, May 2011.
- [71] C. Villani, Y. Farnam, T. Washington, J. Jain, and W. J. Weiss, "Performance of Conventional Portland Cement and Calcium Silicate Based Carbonated Cementitious Systems During Freezing and Thawing in the presence of Calcium Chloride Deicing Salts," *J. Transp. Res. Rec.*, 2015.

- [72] A. K. Suryavanshi, J. D. Scantlebury, and S. B. Lyon, "Mechanism of Friedel's salt formation in cements rich in tri-calcium aluminate," *Cem. Concr. Res.*, vol. 26, pp. 717–727, 1996.
- [73] Y. Farnam, D. P. Bentz, A. Hampton, and W. J. Weiss, "Acoustic Emission and Low Temperature Calorimetry Study of Freeze and Thaw Behavior in Cementitious Materials Exposed to Sodium Chloride Salt," *J. Transp. Res. Rec.*, vol. 2441, pp. 81–90, 2014.
- [74] T. R. Jensen, A. N. Christensen, and J. C. Hanson, "Hydrothermal transformation of the calcium aluminum oxide hydrates  $\text{CaAl}_2\text{O}_4 \cdot 10\text{H}_2\text{O}$  and  $\text{Ca}_2\text{Al}_2\text{O}_5 \cdot 8\text{H}_2\text{O}$  to  $\text{Ca}_3\text{Al}_2(\text{OH})_{12}$  investigated by in situ synchrotron X-ray powder diffraction," *Cement and Concrete Research*, vol. 35, pp. 2300–2309, 2005.
- [75] B. Masschaele, M. Dierick, V. Cnudde, L. V. Hoorebeke, S. Delputte, A. Gildemeister, R. Gaehler, and A. Hillenbach, "High-speed thermal neutron tomography for the visualization of water repellents, consolidants and water uptake in sand and lime stones," *Radiat. Phys. Chem.*, vol. 71, no. 3–4, pp. 807–808, Oct. 2004.
- [76] Y. Bu, D. Luo, and W. J. Weiss, "Using Fick's Second Law and the Nernst-Planck Approach in the Prediction of Chloride Ingress in Concrete Materials," *Adv. Civ. Eng. Mater.*, 2014.

- [77] X. Pang, D. P. Bentz, C. Meyer, G. P. Funkhouser, and R. Darbe, "A comparison study of Portland cement hydration kinetics as measured by chemical shrinkage and isothermal calorimetry," *Cem. Concr. Compos.*, vol. 39, pp. 23–32, 2013.
- [78] M. R. Conde, "Properties of aqueous solutions of lithium and calcium chlorides: formulations for use in air conditioning equipment design," *Int. J. Therm. Sci.*, vol. 43, no. 4, pp. 367–382, Apr. 2004.
- [79] "Calcium chloride: A guide to physical properties." Occidental Chemical Corporation.
- [80] K. Hong and R. D. Hooton, "Effects of cyclic chloride exposure on penetration of concrete cover," *Cem. Concr. Res.*, vol. 29, no. 9, pp. 1379–1386, 1999.
- [81] M. Collepardi and S. Biagini, "Effect of water/cement ratio, pozzolanic addition and curing time on chloride penetration into concrete," in *European Ready Mixed Concrete Organisation Congress*, 1989.
- [82] K. Peterson, G. Julio-Betancourt, L. Sutter, R. D. Hooton, and D. Johnston, "Observations of chloride ingress and calcium oxychloride formation in laboratory concrete and mortar at 5 C," *Cem. Concr. Res.*, vol. 45, pp. 79–90, 2013.
- [83] L. Koester, "Neutron Scattering Lengths: A Survey of Experimental Data and Methods," *At. Data Nuclear Data Tables*, vol. 49, no. 1, pp. 65–120, 1991.
- [84] T. Sato, T. Goto, and K. Sakai, "Mechanism for reducing drying shrinkage of hardened cement by organic additives," *CAJ Rev.*, vol. 5, pp. 52–55, 1983.



- [85] R. Tomita, Y. Simoyama, and K. Inoue, "Properties of hardened concrete impregnated with cement shrinkage reducing agent.," *CAJ Rev.*, pp. 314–317, 1986.
- [86] R. Tomita, K. Takeda, and T. Kidokoro, "Drying shrinkage of concrete using cement shrinkage reducing agent," *CAJ Rev.*, pp. 298–201, 1983.
- [87] S. P. Shah, M. E. Karaguler, and M. Sarigaphuti, "Effects of shrinkage-reducing admixtures on restrained shrinkage cracking of concrete," *ACI Mater. J.*, vol. 89, pp. 291–295, 1992.
- [88] D. P. Bentz, M. R. Geiker, and K. K. Hansen, "Shrinkage-reducing admixtures and early-age desiccation in cement pastes and mortars," *Cem. Concr. Res.*, vol. 31, pp. 1075–1085, 2001.
- [89] W. J. Weiss, "Shrinkage cracking in restrained concrete slabs: Test methods, material compositions, shrinkage reducing admixtures and theoretical modeling," Northwestern University, 1999.
- [90] W. J. Weiss, W. Yang, and S. Shah, "Factors influencing durability and early-age cracking in high strength concrete structures, High Performance Concrete: Research to Practice," *ACI Spec. Publ.*, vol. 186, pp. 387–409, 1999.
- [91] H. Ai and J. F. Young, "Mechanisms of shrinkage reduction using a chemical admixture," in *10th International Congress on the Chemistry of Cement*, 1997, p. 8.
- [92] D. P. Bentz, "Influence of Shrinkage-Reducing Admixtures on Early-Age Properties of Cement Pastes," *J. Adv. Concr. Technol.*, vol. 4, pp. 423–429, 2006.

- [93] W. J. Weiss and N. Berke, “Admixtures for reduction of shrinkage and cracking,” *Report 25: Early Age Cracking in Cementitious Systems-Report*. RILEM Technical committee TC 181-EAS: Early age cracking shrinkage induced stresses and cracking in cementitious systems., 2003.
- [94] N. Berke, M. Dallaire, M. Hicks, and A. Kerkar, “New Developments in Shrinkage-Reducing Admixtures,” *ACI Spec. Publ.*, p. 173, 1997.
- [95] S. Shah, W. J. Weiss, and W. Yang, “Shrinkage cracking-Can it be prevented?,” *Concr. Int.*, vol. 20, 1998.
- [96] ACI Committee 231, “ACI 231 R-10 - Report on Early-Age Cracking: Causes, Measurement, and Mitigation,” 2010.
- [97] B. Pease, H. Shah, and J. Weiss, “Shrinkage, Stress Development, and Early-Age Cracking in Concrete Containing Shrinkage Reducing Admixtures (SRA’s),” *ACI 223*, vol. SP-227, p. 350 pp., 2006.
- [98] F. Rajabipour, G. Sant, and J. Weiss, “Interactions between shrinkage reducing admixtures (SRA) and cement paste’s pore solution,” *Cem. Concr. Res.*, vol. 38, pp. 606–615, 2008.
- [99] A. B. Eberhardt, “On the mechanisms of shrinkage reducing admixtures in self consolidating mortars and concretes,” 2011.
- [100] C. Villani, “Transport Processes in Partially Saturated Concrete: Testing and Liquid Properties,” Purdue University, 2014.
- [101] R. Zana, *Dynamics of Surfactant Self-Assemblies: Micelles, Microemulsions, Vesicles and Lyotropic Phases*. 2005, p. 536.

- [102] A. Schiebl, W. J. Weiss, J. Shane, N. Berke, T. Manson, and S. Shah, “Assessing the moisture profile of drying concrete using impedance spectroscopy,” *Concr. Sci. Eng.*, vol. 2, pp. 106–116, 2000.
- [103] A. Radlinska, F. Rajabipour, B. Bucher, R. Henkensiefken, G. Sant, and J. Weiss, “Shrinkage Mitigation Strategies in Cementitious Systems: A Closer Look at Differences in Sealed and Unsealed Behavior,” *Transp. Res. Rec. J. Transp. Res. Board*, vol. 2070, pp. 59–67, 2008.
- [104] W. J. Weiss, “SPR-3864: Performance of Deicing Salts and Deicing Salt Cocktails,” Joint Transportation Research Board, 2014.
- [105] B. Villmann, V. Slowik, F. H. Wittmann, P. Vontobel, and J. Hovind, “Time-dependent Moisture Distribution in Drying Cement Mortars – Results of Neutron Radiography and Inverse Analysis of Drying Tests,” *Restor. Build. Monum.*, vol. 20, pp. 49–62, 2014.
- [106] P. Lura, M. Wyrzykowski, C. Tang, and E. Lehmann, “Internal curing with lightweight aggregate produced from biomass-derived waste,” *Cem. Concr. Res.*, vol. 59, pp. 24–33, 2014.
- [107] P. Coussot, “Scaling approach of the convective drying of a porous medium,” *Eur. Phys. J. B-Condensed Matter*, vol. 566, pp. 557–566, 2000.
- [108] G. W. Scherer, “Theory of Drying,” *J. Am. Ceram. Soc.*, vol. 73, pp. 3–14, 1990.
- [109] G. W. Scherer, “Crack-tip stress in gels,” *J. Non. Cryst. Solids*, vol. 144, pp. 210–216, 1992.
- [110] T. M. Shaw, “Drying as an immiscible displacement process with fluid counterflow,” *Phys. Rev. Lett.*, vol. 59, pp. 1671–1674, 1987.

- [111] G. W. Scherer, "Aging and drying of gels," *J. Non. Cryst. Solids*, vol. 100, pp. 77–92, 1988.
- [112] A. Anderberg and L. Wadsö, "Method for simultaneous determination of sorption isotherms and diffusivity of cement-based materials," *Cem. Concr. Res.*, vol. 38, pp. 89–94, 2008.
- [113] V. Baroghel-Bouny, "Water vapour sorption experiments on hardened cementitious materials. Part II: Essential tool for assessment of transport properties and for durability prediction," *Cem. Concr. Res.*, vol. 37, pp. 438–454, 2007.
- [114] M. Mainguy, O. Coussy, and V. Baroghel-Bouny, "Role of Air Pressure in Drying of Weakly Permeable Materials," *J. Eng. Mech.*, vol. 127, pp. 582–592, 2001.
- [115] P. Trtik, B. Muench, W. J. Weiss, G. Herth, A. Kaestner, E. Lehmann, and P. Lura, "Neutron tomography investigation of superabsorbent polymers in cement paste," in *International Conference on Material Science and 64th RILEM Annual Week in Aachen - MATSCI*, pp. 1–10.
- [116] H. Todak, C. L. Lucero, and W. J. Weiss, "Why is the Air There? Looking at Freeze-Thaw in Terms of Saturation," *NRMCA Concrete InFocus*, Spring 2015.